The development of surface treatments on galvanised steel products for the automotive industry utilising a chemcoater

Jamie Williams

Thesis Submitted to Swansea University in fulfillment of the requirements for the
Degree of Doctor of Engineering

Spring 2023

Declaration

This work has not previously been accepted in substance for any degree and is not being concurrently submitted in candidature for any degree.

[redacted].............. (candidate)

Date ....26th April 2023..

Statement one: This thesis is the result of my own investigations, except where otherwise stated. Other sources are acknowledged by footnotes giving explicit references. A bibliography is appended.

[redacted]............. (candidate)

Date ....26th April 2023..

Statement two: I hereby give consent for my thesis, if accepted, to be available for photocopying and for inter-library loan, and for the title and summary to be made available to outside organisations.

[redacted]................ (candidate)

Date ....26th April 2023..

Acknowledgements

There are many people I would like to make acknowledgements to, for their help and support throughout this engineering doctorate. Firstly, a special thank you to my academic supervisor Dr Eifion Jewell, a wealth of knowledge, you have always been on hand to share information and steer me in the right direction. Without your guidance, this project would have severely struggled to find a path, especially given the turbulent times of a pandemic and a late move to Asia. I am appreciative of all that you have done, Diolch yn fawr! A massive thank you to my industrial supervisor, Dr. Clive Challinor. You have always been approachable and happy to help wherever needed. You really made the link between academia and industry easy. Thank you for all your encouragement and support, despite our differences in opinion on our national rugby teams! Dr. Christian Griffiths (Chrisy), If I am honest, this entire project would not have been possible without your support. You have always been on hand to assist me wherever needed, sharing your knowledge and being instrumental in keeping the wheels turning on this rickety old bus, hey we even managed to enjoy a few beers on the way. Thanks mate and it's great to be able to call you a friend as well as a mentor now. My mucker (Dr.) Matthew Dodd (Doddsy), it's been a pleasure to graft alongside you mate, at many points we thought it might not happen, but our ~~love of a good pint and continuous moan~~ tenacity to get the job done has surely made it easier! Many others have always been on hand to help when needed. There are too many to list but a big thank you to Dr. Natalie Wint for sharing your expertise and always being there. Dr. Peter Greenwood and Professor Trystan Watson for starting my engineering doctorate journey and helping me establish myself in the early days. Uncle Leighton and the boys at PMRC for always providing a great working environment and helping to get the job done. Finally, a massive thank you to all my friends and family, especially Abbie and my parents who have supported and encouraged me from day one. Without you all, the road certainly would have been much rockier. Spot on.

Abstract

This thesis investigates the development of coatings to be applied via a two-roll roller coating system, a Chemcoater. Novel coatings were investigated to enhance a substrate's performance and add overall value to the hot-dipped galvanised steel product, by adding fuctionalities such as improved corrosion resistance, enhanced surface passivation and increased surface lubricity. Historically, hexavalent chromate was a common component of coatings for hot-dipped galvanised steel to provide corrosion protection during material storage and transportation. However, REACH law within the European Union prohibited its use due to its intrinsic toxicity and detrimental environmental effects. This legislation accelerated industry and researchers' attention toward developing alternative, more environmentally friendly processes. Initial investigations included the analysis of current coatings, PrimeCoat and PLT. Both coatings were shown to have similar rheological characteristics and similar thermal stabilities with PLT performing well as a dry film lubricant. A common laboratory polishing unit was adapted to create a novel Pin-on-Disk tribometer, providing an effective and reliable method for measuring the dynamic coefficient of friction of coated substrates. The adapted unit was designed, built, and commissioned according to ASTM G99-17, and it was able to produce repeatable results for measuring the coefficient of friction. An additional investigation showed that sulphate-based treatments could reduce the coefficient of friction of zinc-coated steel substrates. Tests indicated that a neutral ammonium sulphate solution improved lubricity by 15-10%. Ammonium and sodium sulphate treatments were deemed suitable for coil coating, improving the capacity to reduce oil volume and overall production costs. A systematic study was conducted to improve the processability of a one-step hydrophobic coating. The best-performing coating had a contact angle of 146° with a reduced processing time of ~67%, using IPA as the solvent, 2% wt. 1 M NaOH (aq), 0.2 M stearic acid and micro-SiO2 (0.2–0.3 µm). This method significantly reduced processing time and fewer health and safety risks, avoiding the use of toxic chemicals. On further analysis, the coating was shown to be relatively formable and durable, with no significant reduction in hydrophobic performance after 30% strain was induced. Several corrosion analysis techniques showed increased performance in comparison to uncoated hot-dipped galvanised steel samples. These results suggested that the coating could be a viable option for some industrial applications and showed a potentially positive alternative to banned hexavalent chromate options. The chemical constituents of the newly proposed coatings have significantly less toxicity and pose a reduced negative effect on the wider environment and its users.

Table of Contents

Table of Figures

Table of Tables

Abbreviations

HDG	Hot-Dipped Galvanised
CA	Contact Angle
IPA	Isopropyl Alcohol
SEM	Scanning Electron Microscopy
EDX	Energy Dispersive Spectroscopy
AFM	Atomic Force Microscopy
XRD	X-ray Diffraction
ST	Interfacial Surface Tension
STA	Simultaneous Thermal Analysis
XRF	X-ray Fluorescence
FTIR	Fourier Transform Infrared Spectroscopy
LFT	Linear Friction Testing
DFT	Dynamic Friction Testing
SVET	Scanning Vibrating Electrode Technique
EIS	Electrical Impedance Spectroscopy

1 Introduction

1.1 General introduction

Coiled strip steel products are manufactured in the UK by Tata Steel and sold globally. Strip steels have a wide range of applications but are frequently used in the automotive, construction and packaging industries. A typical product consists of an annealed steel strip with an applied zinc coating via galvanisation. Galvanisation is a manufacturing process whereby a metallic coating is applied to steel, providing anodic corrosion protection to the underlying substrate by acting as an anode and being more preferential for corrosion than the underlying substrate (1). The metallic coatings are applied to the steel strip at speeds of up to 200 m/min with commonly applied coating weights ranging from 70 gm^{-2} to 275 gm^{-2}. Subsequent organic and inorganic coatings can be applied to the steel following annealing or galvanising to further enhance its performance and atmospheric corrosion resistance. Typically, inorganic coatings are characterised by having a non-carbon binder present, whereas organic coatings are often composed of carbon-based substances. Tata Steel implement a continuous coating process using an inline roll-coating system known as the chemcoater.

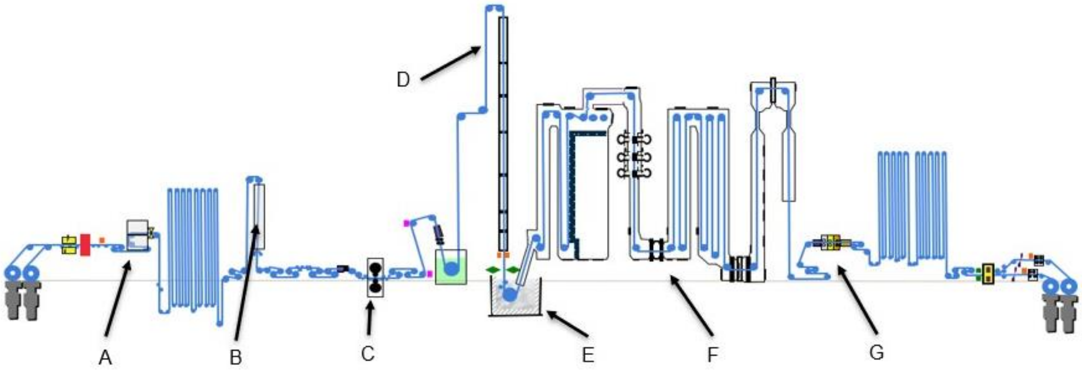

A = Double-sided inspection system
B = Chemcoater system
C = Polishing section
D = Matt mill/cooling tower
E = Weir system and zinc pot
F = Combination furnace
G = Brushing system

Figure 1. Schematic of Tata Steel's ZODIAC galvanising line, Llanwern.

Commonly applied coatings can significantly improve characteristics such as corrosion resistance, lubricity and surface passivation, or add specific functionality, with the ultimate aim of adding value to the steel product (2,3). Figure 2, demonstrates a summary of the work presented in this thesis and what has been discussed.

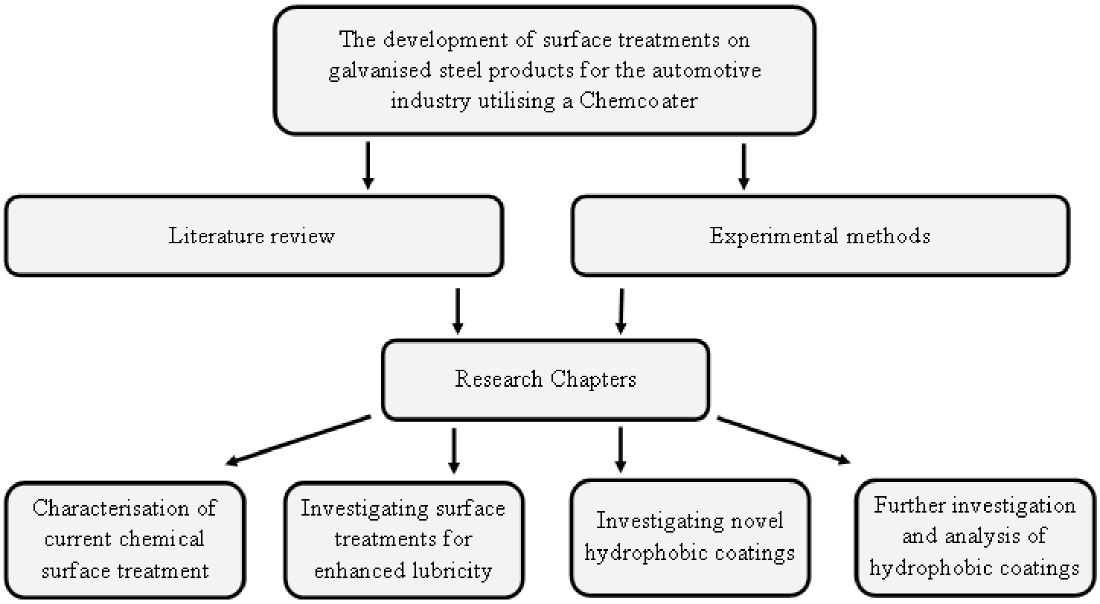

Figure 2. Flow chart summarising the thesis content.

1.2 Project aim

This research project aimed to explore the development of novel coatings to be used via a two-roll roller coating system, a chemcoater, in order to improve a hot-dipped galvanised substrate’s performance and add overall value to the product, via increasing surface passivation, enhancing surface lubricity and increasing hydrophobicity. In addition to the development of novel coating systems, the research project also allowed the characterisation, review and evaluation of current coatings applied by Tata Steel.

1.3 Environmental impact

The steel industry is one of the world’s largest, energy-consuming manufacturing industries and as a result steel companies are very aware of the sustainability challenges they face (4). Within industry, the need for reduced energy consumption when producing steel is paramount. Currently, the biggest environmental impact lies besides increasing energy and carbon dioxide outputs. By applying coatings, the overall performance of steel products can be significantly enhanced, improving their resistance to degradation and corrosion. With improved steel performance, the steel’s lifecycle can be maximised, in turn reducing the amount of wasted steel and the demand for new steel to be produced. Historically, popular coatings utilised in the coil coating industry contained hexavalent-chromate, due to its excellent corrosion resistance properties. However, REACH legislation was enforced across the European Union, banning the use of hexavalent-chromate due to its toxicity and negative consequences for the wider environment. This legislation has accelerated industry and researchers’ attention towards developing alternative, more environmentally friendly processes and solutions (5,6).

This research project allows the characterisation and development of current and novel coil coating surface treatments, providing alternatives to hexavalent-chromate systems. Improving surface functionality and coating productivity can also improve durability and/or reduce the manufacturing time needed for the product. In turn, this gives the opportunity to increase product life expectancy, minimise material waste, reduce overall energy expenditure demands and allow differentiation of coating products to the market. These factors provide potential to positively impact current market sectors that use HDG steel, such as the automotive, construction and industrial/manufacturing industries. In addition, the expansion and improvement of systems could open opportunities for Tata steel to begin supplying products in new markets, such as the renewable energy infrastructure, advanced manufacturing and advancing emerging markets.

2 Literature review

2.1 Introduction

At present, the chemcoater has the potential for applying many organic and inorganic coatings to steel after the galvanising process. The system follows a two-roll, roller-coating process, that provides an effective method of depositing coatings on to the zinc-alloy coated steel strip. Roller coating is a process whereby a liquid film is formed on a continuous web (e.g. a steel substrate) by the use of two or more rotating rolls. The gap between the adjacent rolls and their relative speeds is the primary factor determining the thickness of the coating. The relative direction of the rollers also distinguishes the overall finish on the coated substrate. In direct roll coating, the roll surfaces move in the same direction in comparison to reverse roll coating, where the roll surfaces move in opposing directions (7). Figure 3 demonstrates the chemcoater apparatus at Tata Steel's ZODIAC galvanising line.

Figure 3. Chemcoater apparatus at ZODIAC galvanising line, Llanwern.

The chemcoater provides an effective platform to add additional value to the product for Tata Steel. Currently, the chemcoater system is underutilised and only used for depositing a single passivation layer on to a small proportion of substrate that leaves Tata Steel's ZODIAC site. Throughout the duration of this project, the capabilities of the system have been explored to enhance its effectiveness and investigate new, novel coatings that could provide functionality and value to finished products. Passivation treatments have historically included toxic and harmful hexavalent chromium-based inhibitors (Cr^{6+}). These treatments were applied to steel substrates via the addition of a chromium coating layer on top of the zinc and metallic-alloy coating. Hexavalent chromium-based treatments have been shown to greatly aid galvanised steel's corrosion resistance, whilst improving adhesion properties at the surface (2,8–10). It acts as an anodic inhibitor, forming a passive layer and slowing zinc dissolution. Whilst additionally acting as an efficient cathodic inhibitor, lowering the rate of oxygen reduction at the metal surface (2). However, restrictions have been placed on the inclusion of chromium within conversion coatings by the European Union regulation, REACH (Registration, Evaluation, Authorisation and restriction of Chemicals). These restrictions have been placed due to chromium's apparent toxicity and carcinogenic effects, which pose potential health risks (3,11–13).

2.2 Properties of galvanised steel

Historically, steel has been utilised within building and automotive engineering industries, due to its high strength-weight ratio and relative low cost in comparison to other materials. However, a negative of steel is its tendency to corrode in humid conditions. Hot-dip galvanising provides an effective and robust method of metallic coating to increase steel's durability, corrosion resistance and paintability. The outer coating is primarily made up of Zinc, which acts as a sacrificial anode to protect steel from corrosion (1).

Three different metallic coatings have been implemented through hot dipping at Tata Steel's ZODIAC site. These metallic coatings include galvanised steel (>99% zinc content), MagiZinc (zinc coating with additional magnesium and aluminium content) and the now discontinued, Galvanneal steel (zinc coating with 8-12% iron content) (14). Table 1 displays the common mechanical properties of DX57 grade steel commonly used within the automotive sector.

Table 1. Mechanical properties of DX57 grade steel produced by Tata Steel (14).

	Strength (Nmm^{-2})		**Elongation**
Grade	**Yield**	**Tensile**	**Min. after fracture (%)**
DX57D	120-170	260-350	39
DX57D HyperForm	120-160	260-350	43

2.2.1 Continuous hot dip galvanising process

The technique of hot dip galvanisation involves the immersion of a substrate in molten Zinc and has been a commercially accepted method of metallic coating since 1850. Generally speaking, the specification for hot dip galvanising of iron and steel complies with standard EN ISO 1461. Historically, conventional HDG processes have included cleaning, before being submerged into molten zinc (1). After the cleaning process, the substrate is continuously passed through a pot of molten zinc, upon exit it is cooled for solidification and forms the protective zinc coating on the substrate's surface. The quality of the final metallic coating is dependent upon: the composition of the steel substrate, the quality of molten zinc, the composition/temperature of galvanising bath, immersion duration and the rate of substrate removal (1,15,16).

2.2.2 The corrosion resistance of galvanised steel

A metallurgical bond between the steel substrate and zinc coating is formed to serve as a protective barrier with lower corrosion and dissolution rates. Zinc has the ability to form protective layers of basic carbonates, oxides and hydrated sulphates depending on its environment. When formed into a complete layer, corrosion proceeds at a much slower rate (17–19). Despite this, galvanised steels can still be subjected to corrosion failure. Corrosion can be defined as the physicochemical interaction between a metal and its environment, which results in changes in the properties of the metal. Which may often lead to impairment of the function of the metal, the environment, or the technical system of which these form a part (20). Corrosion can have a negative impact on the performance and aesthetic of substrates, so should be minimised wherever possible to improve product lifetime. Generally, HDG steels corrode as a result of general zinc dissolution away from the coating surface. A summary of the atmospheric corrosion mechanisms of zinc are expressed below (21):

Anodic reactions:

$$Zn + 2H_2O \rightarrow Zn(OH)_2 + 2H^+ + 2e^- \quad (1)$$

$$Zn(OH)_2 \rightarrow ZnO + H_2O \quad (2)$$

Cathodic reaction:

$$O_2 + 2H_2O + 4e^- \rightarrow 4OH^- \quad (3)$$

On the corrosion of zinc, zinc hydroxide forms first across the surface, zinc hydroxide then becomes dehydrated and forms zinc oxide accompanied by water molecules. Additionally, due to zinc hydroxide's low electrical conductivity, it retards oxygen reduction, hence the reaction (3). Zinc oxide is less effective at suppressing this reaction and thus corrosion continues to initiate (21).

Localised crevice corrosion can occur under certain conditions, for example, if zinc is exposed to water at a local, calcareous crack site. Intergranular corrosion of zinc coatings is not usually an issue unless certain impurities are present in the stoichiometry. Exposure of unprotected steel surfaces to other metals can cause bi-metallic corrosion when in the presence of an electrolyte (18). Other examples of corrosion failure for galvanised steel when in atmospheric conditions include:

blistering due to rust and corrosion creep or undercutting of exposed areas or defects (22).

Therefore, the application of additional coatings to a hot-dipped galvanised substrate can further enhance its corrosion resistance characteristics. These coatings have become particularly prevalent in the industry to further enhance the performance and functionality of HDG substrates.

2.3 Rheology and surface chemistry of coatings

The term coating refers to a metallic and/or non-metallic layer/film spread over a surface for added protection or decoration. The application of a coating is intended to protect the substrate from reacting with its environment (23). Within industry, coatings generally serve one or more of the following purposes: to alter physical properties (e.g. colour, conductivity, reflectivity, etc); to protect surfaces from corrosion or to add functionality (like controlling friction and wear through enhanced lubricity)(24).

For a coating to create an effective, functional barrier it must be continuous and free from defects. The material is required to be easily handleable, and generally deposited from a container, on to a surface, at an appropriate film thickness. Critically, an important property of coating is how the material flows. Rheology relates to the science behind how materials flow and deform. It can be summarised as “the rate at which a material resists permanent change of shape” (25). In general, the four categories of rheology can be recognised: viscosity, elasticity, rigidity and plasticity. The viscosity of a fluid is defined as the magnitude of internal friction and is a measure of the force per unit area that resists uniform flow. In simple terms, viscosity is the resistance of the material to flow, the ratio of shear stress to shear rate (26). Shear Stress relates to the force per unit area applied to a material, whilst the shear rate is a measure of how quickly a material deforms and the magnitude of energy applied.

Viscosity (η) of a material can be resolved mathematically as the ratio of the shear stress (τ) per unit area to the shear rate (γ)(25,26):

$$\eta = \tau / \gamma \tag{4}$$

Additional factors affect viscosity such as temperature and the solvent used. Viscosity can be reduced or increased through manipulation of temperature, for example, the preheating of ultraviolet curable coatings after application (26). This is observed in the curing of paints. Viscosity can be separated into categories: dynamic, kinematic, apparent and relative viscosity. In classical fluid mechanics, dynamic viscosity is defined as the stress in phase with the rate of strain, divided by the rate of strain. Kinematic viscosity is defined as the dynamic viscosity divided by the density of a material. Apparent viscosity refers to the relationship between viscosity with shear rate and relative viscosity refers to the relationship between molar mass and viscosity (27). Dynamic viscosity is generally considered an absolute viscosity measurement and shows the material’s internal resistance to flow.

Surface chemistry deals with the interface between two materials, independent of the phase of the material. For the understanding of coatings, only the liquid-solid interface needs to be explored. The rheological properties of a coating, such as viscosity significantly impact its performance. These properties influence application quality, appearance, and functionality. They can have a determining effect on uniformity, drying time, and stability. Proper control of a coating's rheology is essential for achieving desired coating characteristics and ensuring it can effectively function as it is intended.

2.3.1 Newtonian materials

Newtonian materials are identified as having applied stress proportional to the shear rate. Additionally, their viscosity is invariant with either variable and therefore remains constant with increasing shear rate (25). Figure 4 (a) depicts Newtonian behaviour and the relationship between shear stress applied and viscosity with shear rate. Within rheological behaviour, the simplest form a liquid will show is when the applied stress is proportional to the shear rate. Many simple molecules of low molecular weight are Newtonian when liquid.

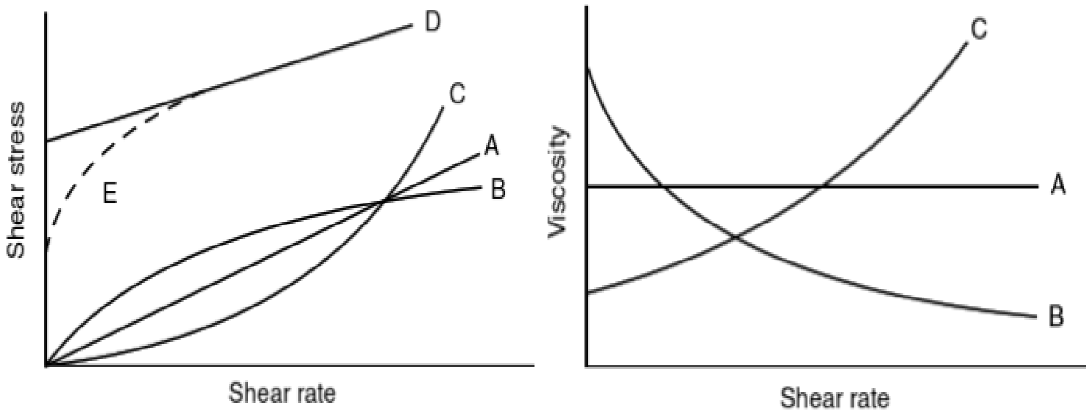

Figure 4. Schematic diagram of shear stress and viscosity against shear rate for (a) Newtonian (b) Shear thinning (c) Shear thickening (d) Bingham plastic (e) Plastic (25).

2.3.2 Non-Newtonian materials

Non-Newtonian materials find that viscosity does not remain constant with increasing shear rate or shear stress. Figure 4 (a) and (b) demonstrate shear thinning and shear thickening behaviour respectively. Shear thinning materials (Pseudoplastics) experience a decrease in viscosity with increasing shear rate and often are used as paints and coatings. However, this is mainly dependent on the exact chemical composition and physical nature of the materials used (25). Similarly to plastic materials, pseudoplastic materials drop in viscosity as force is applied. They differ from plastic materials as they have no fixed yield point. Viscosity increases by the same amount as the shear rate is reduced. Viscosity can be dependent on two factors: the amount of mechanical force applied and the length of time it is applied for. Time-dependent behaviour is displayed by coating materials, there is a delay in viscosity increase or decrease after the force has been removed. Thixotropic behaviour is observed when the viscosity is shown to decrease with time, even when shear remains constant, only returning to its original value after a period of rest (25,26,28).

Conversely, shear thickening (dilatants) materials increase viscosity with increasing shear rate. This is due to the materials generally containing a high concentration of particulates. True shear thickening behaviour occurs independently of solvent loss. Rheopectic materials display the opposite behaviour to thixotropic materials. They are time-dependent materials that cause shear thickening. An increase in viscosity is observed over time, with constant shear, only returning to its original value after a period of rest (25,26,28).

Plastic behaviour is observed in Figure 4 (e), once the yield point has been reached, the material begins to approach Newtonian-like behaviour as the shear rate is increased. This type of flow requires a specific amount of stress to be applied before the material is allowed to flow, this can be observed as the line intersects the Y-axis (25,26). Bingham plastics as observed in Figure 4 (d) demonstrate viscoplastic behaviour, whereby the material exhibits rigidity under low stresses but fluid viscosity under high stresses (29).

2.3.3 Surface energy

2.3.3.1 Surface tension

Liquids are generally made up of molecules that are in close proximity to each other. These molecules display attractive forces due to asymmetrical charge distributions in their electron clouds. Attractive forces are recognised as the universal property surface tension with unit, force per unit length at the surface: dynes per centimetre.

When a droplet of liquid is suspended in air a spherical shape is formed due to surface molecules being attracted to molecules around them. A minimum sphere surface area results. All liquids in suspension attempt to form a sphere, however when a liquid comes into contact with a solid surface, a solid-liquid interface is formed. The surface tension acts in redistributing the liquid layer, but at this interface, intramolecular forces are present between molecules of the liquid and intermolecular forces are now present between the liquid molecules and solid surface molecules they come into contact with (30). Thus, these forces determine every material's specific surface tension value. Liquids with high intramolecular attraction show high surface tension values and so will show a strong tendency to form spheres (i.e. water). Liquids with low intramolecular attraction show less tendency to form spheres and can be overcome by countering forces. The surface tension of liquids can be measured through methods such as a capillary tube, Du Nuoy ring, and the pendant drop method (26).

2.3.3.2 Contact angle

When a liquid comes into contact with a flat surface it either dewets to form a droplet or wets and flows out across the surface. The droplet/edge of the droplet creates an angle with the solid plane, commonly known as the contact angle, θ. If the contact angle is greater than 0°, a nonwetting condition exists, where the material's intramolecular attraction is greater than the intermolecular attraction with the solid surface. Thus, the material's surface tension value is higher than the solid's surface energy. In contrast, if the contact angle is 0° then wetting occurs. Measuring contact angle enables us to understand the relative difference between two surface tensions. Smaller contact angles indicate similar (but not equal) surface tension values, whilst a large angle signifies a large difference in values (26,31,32). Figure 5 shows an illustration of a liquid's ability to wet on to a solid surface, the contact angle is also identified.

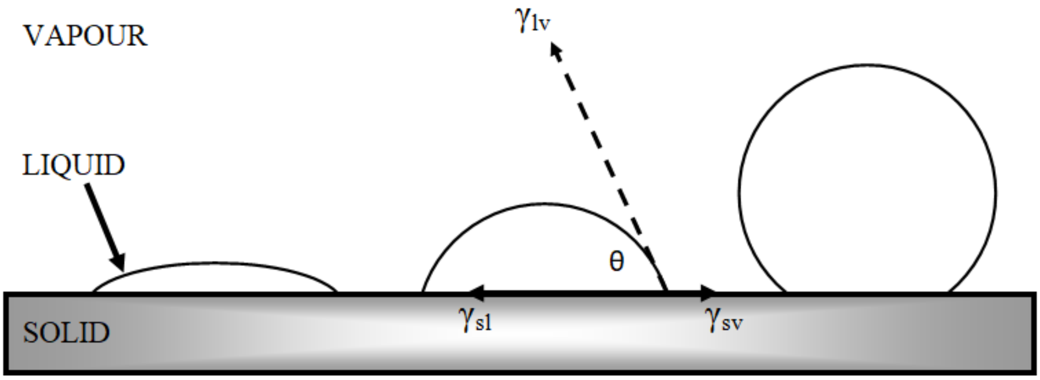

Figure 5. Schematic demonstrating great, good and poor wetting of a surface.

The equilibrium contact angle for a droplet of liquid sitting on a smooth, homogeneous and non-deformed surface is given by Young's equation:

$$\gamma_{lv} \cos(\theta) = \gamma_{sv} - \gamma_{sl} \tag{5}$$

Where γ_{lv} is the surface tension of the liquid within its saturated vapour, γ_{sv} is the surface tension of the solid with the saturated vapour of the liquid and γ_{sl} is the interfacial tension between the solid and the liquid. For wetting to occur the liquid surface tension must be greater than the surface tension of the solid as θ is equal to zero. Surfactants, commonly known as wetting agents, can be utilised to alter the interactions between interfacial molecules. They do so by modifying the surface tension of either the liquid or the solid substrate. Common materials used as surfactants include fluorochemicals, silicones and hydrocarbons (26).

2.3.3.3 Levelling

Levelling refers to the aesthetic appeal of a coating and its ability to level out and become smooth after application. It is reliant on the rheology and surface chemistry of a coating and substrate. Understanding the dynamics of levelling is crucial as with manipulation, it is possible to improve the overall surface finish of a coating. Levelling can be improved through five different variable changes. Including: increasing the duration of the levelling process, increasing the surface tension of the coating, increasing the coating thickness, decreasing the coating viscosity, or reducing the wavelength (minimising the distance between repeating ridges)(26).

2.4 Adhesion of coatings

Adhesion can be described as "the physical resistance of an interface between regions of the material system". It is an interfacial process and in practice, is a function of the basic adhesion properties, a summation of all intermolecular interactions at the interface (33,34). Cohesion can be defined as the mutual attraction and intrinsic sticking property between molecules of a substance. Adhesion and cohesion have a significant impact on the performance of a coating and can relate to the ability of a coating to successfully adhere to a substrate surface over a sustained period (34). There are many different theoretical mechanisms for the adhesion of coatings to a substrate including: physical adsorption, mechanical interlocking, chemical bonding, diffusion, electrostatic force, and weak boundary layer theories. These theories provide an important insight into understanding the adhesive processes at an atomic and molecular level, however, experimental tests provide important information about the coating adhesion at the macroscopic level (26,33–36).

2.4.1 Adhesion failure modes

The durability of a coating can be directly affected by its adhesion properties. Failure modes of coating adhesion can be separated into three general categories: formulation-related, substrate-related and physical defect-related failure modes (37). Formulation-related failures occur as a result of the constituent parts (resins/solvents/pigments) used and their inadequate formulation within the coating. Substrate-related failure can occur due to poor preparation of a surface before coating, some coating's new appropriate cleaning, pre-treatment, or roughening for successful adherence. Physical defect-related failures can lead to localised areas of stress through such things as: blistering, bubbling, peeling or mechanical damage. If cleavage is initiated within these localised stress areas, significant damage and separation between the coating and/or substrate can occur (26,37). Figure 6 demonstrates the cohesive and adhesive failure of a coating on a substrate.

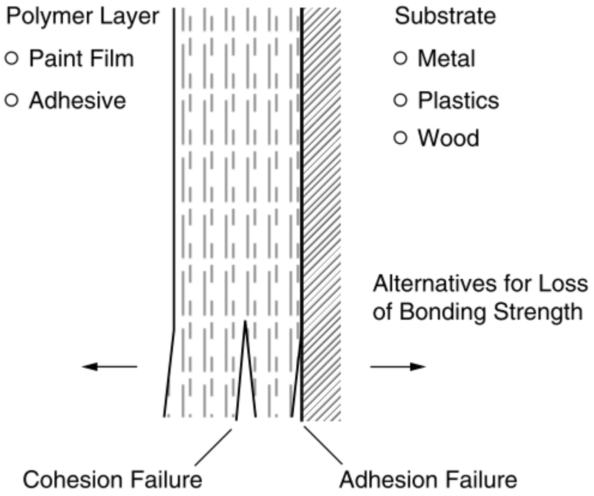

Figure 6. Schematic demonstrating cohesion and adhesion failure between two substrates (26).

Mechanical damage provides a significant threat to coating adhesion and if a substrate is subjected to sufficient external force, coating failure can occur. Whether a coating is to fail cohesively or through adhesion failure is completely dependent upon the type of material being used. Cohesive failure will occur if adhesion at the coating-substrate interface surpasses the cohesion of the coating layer. In contrast, if the cohesive forces surpass adhesion, a definite separation at the interface can occur (26). It must also be noted that, whilst adhesive failure is often a significant factor within coating failure, it is not always the root cause. It is important to note that other factors such as corrosion resistance, mechanical damage, chemical exposure and other elements can also influence the failure of a coating.

2.5 Coil coating process

Coil-coating is a common process used to continuously coat a flat substrate usually via liquid-based treatments. The process usually includes some form of cleaning, chemical pre-treatment and single or multiple applications of a coating. In general, substrates to be coated are cold-rolled steels, aluminium or tinplate products. The process is commonly highly automated and utilises rolls to coat substrates to a consistently high standard (38). An example of Tata Steel’s full coil-coating line is shown in Figure 1. The line provides strict parameters that help to appropriately manage variables such as film thickness, volume, curing/drying time and material surface preparation to produce a consistent and high-quality coating. Generally. coil-coating lines use either direct or reverse roll coating applications. Drying is achieved via conveyorised ovens, whereby the coated strips pass through after deposition. This allows application layers to cure quicker, meaning a faster throughput and production rate (38,39).

2.5.1 Surface preparation for coil coating

Different material interfaces require different methods of surface preparation for good adhesion characteristics. In general steel, surfaces need to be free from foreign bodies such as rust, salts, oil, grease, moisture and any substances that may have a negative effect on the adhesion process. This preparation can be achieved through various manual and chemical methods, including processes in the order of grinding, sanding, polishing, mechanical polishing, cleaning, electropolishing, degreasing, etching and pickling (34,40).

The preparation of hot-dipped galvanised steel strip for coating is crucial to ensure good adhesion between substrate and coating. Historically, degreasing is a method used to effectively clean the substrate surface. Degreasing completely removes disparities away from the surface including the likes of oil, grease, dirt, and swarf, through techniques such as solvent, alkaline or steam cleaning before rinsing and with water and drying thoroughly (41,42).

2.5.2 Roll coating types

When discussing roll coating applications, there are often two common methods, direct and reverse roll coating. In direct roll coating applications, the substrate is passed through two pre-set rolls, the applicator roll rotates in the same direction as the substrate passes, subsequently applying a film to the surface of the substrate. This form of coating is also commonly referred to as ‘forward roll’ coating (43). The wet film thickness on the steel strip is adjusted by altering the clearance between the doctor and applicator rolls. Adjusting the speeds and the loads on the rolls also allows the modification of final film stability and thickness (43,44). This variation of roll coating allows substrates to be coated on a singular face or both sides simultaneously. Film thickness can be determined by the fluid mechanics with the nip region (the area between the two opposing rolls). Within this region pressure increases at the inlet and decreases at the outlet, splitting the film into two. Pressure values are dependent on the parameters of the fluid being utilised and the nip region (7). Direct roll coating allows the wet film thickness to be controlled more accurately than reverse roll coating. Additionally, the applicator roll in direct roll coating (commonly made from polymers, rubbers or urethane-coated metals) has a longer life expectancy when compared to its counterpart, reverse roll. This is due to the roller undergoing smaller frictional stresses (7,43). Figure 7 demonstrates both direct and reverse roll coating.

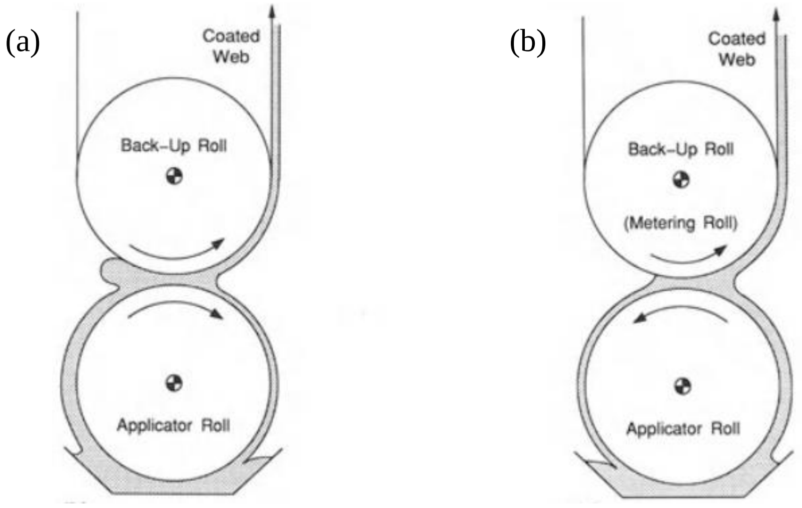

Figure 7. Schematic demonstrating two-roll coater: (a) direct roll (b) reverse roll (7).

Reverse roll coating application is similar to direct roll coating, with a continuous web passing through rollers. However, the applicator roll rotates in the reverse direction to that of the moving web. This has a significant impact on the fluid between the rolls and its subsequent transfer to the substrate. Reverse roll coating forms a significantly better surface finish than direct roll coating. During film formation, smoother and thinner films can be formed due to the liquid being subjected to higher shear stresses and extensional rates over a very short period. Higher shear is apparent due to the fluid within the nip being sheared in opposing directions by the individual rollers. This can assist in reducing pseudoplastic coating's viscosity, enhancing the surface finish (45,46).

2.5.3 Roll coating operability

Table 2 demonstrates the operating parameters and some key characteristics for both direct and reverse roll coating.

Table 2. Approximate operating parameters for direct roll and reverse roll coating (7,47).

Type	Film thickness (μm)	Line speed (m/min)	Viscosity (Pa·s)
Direct	25-60	3-60	0.001 – 0.5
Reverse roll	< 25	30-500	0.001 – 50

Direct roll coating operates with a greater wet film thickness than reverse roll coating, thus meaning reverse roll coating can utilise thinner films. Additionally, in direct roll coating line speeds are limited to 60m/min and the range of fluid viscosity applicable is smaller (7,47). Thus, reverse roll coating tends to be better suited for industrial coil coating purposes, due to the surface finish and higher potential throughput.

Hypothetical operability diagrams for a direct two-roll coater can be seen in Figure 8. The figure demonstrates a comparison between viscous and non-viscous fluids. As can be seen on both (a) and (b), applicator roll speed is shown on the vertical axis against web speed (substrate speed) on the horizontal axis. For the higher viscous coating, ribbing presents the highest threat, when speeds are high. The starvation limit is observed when the applicator roll speed is too low. Additionally, at high applicator roll speed limits, air entrainment could cause issues. For inertial coatings starvation poses the highest threat, this is due to needing a low capillary number (low speed) to stabilise the liquid bead (7). Moreover, at high-speed limits, air entrapment and vortex instability can also become apparent. For both (a) and (b), the dark shaded area shows the favourable limits for efficient direct roll coating.

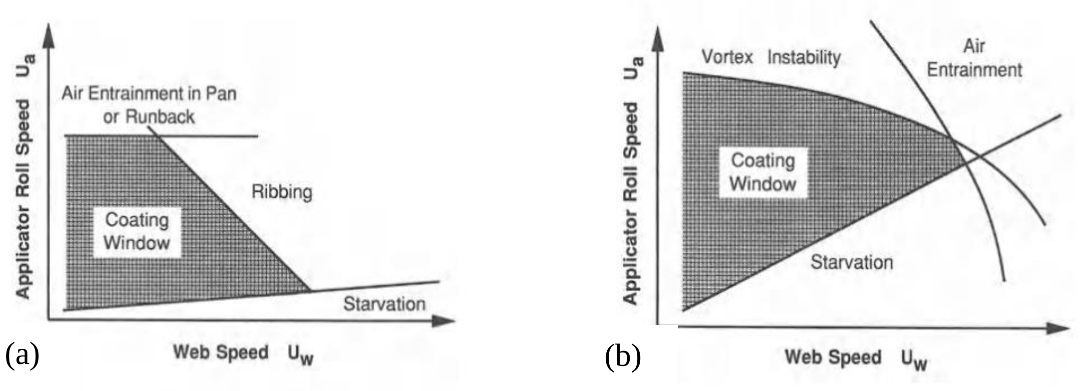

Figure 8. Operability diagrams for direct roll coater for: (a)viscous coating; (b)inertial coating (7).

Hypothetical operability diagrams for a reverse two-roll coater can be seen in Figure 9. The figure demonstrates a comparison between viscous and non-viscous fluids much like the graphs observed in Figure 8. For highly viscous fluids the main failure modes seen are ribbing and cascading which occur when the substrate speed is too low and too high respectively. If the applicator roll speed is higher than an upper limit the coating could suffer from air entrainment. Conversely, if the applicator roll speed is kept to a minimum level, starvation can occur. For inertial coatings that are not very viscous, issues with ribbing and cascading are reduced and starvation becomes the main failure mode. At high applicator roll and substrate speeds, vortex instabilities can also have a negative effect. For both (a) and (b), the dark shaded area shows the favourable limits for efficient reverse roll coating.

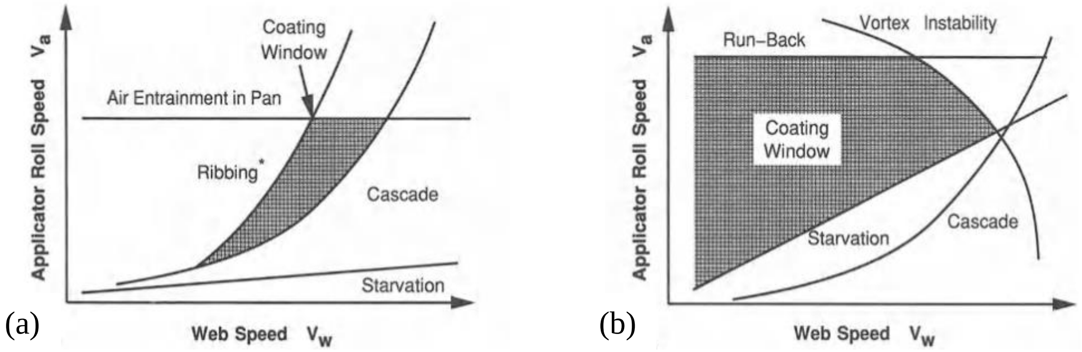

Figure 9. Operability diagrams for reverse coater for: (a)viscous coating; (b)inertial coating (7).

2.5.4 Roll coating defects

In theory, the roll coating process should have significantly reduced defects, due to the high continuous coating speed that can be achieved. In reality, transverse defects can appear, leaving negative effects on the end products such as sagging, bénard cells, fat edges, cascading and ribbing (24,26,45,48–50).

Sagging can occur in coatings applied to inclined or vertical surfaces. It occurs when gravity influences the coating to flow downwards creating a defect. The length of the sagging defect is determined by the velocity of the coating at the liquid-air interface and the time the coating remains in a liquid state. Sagging will occur for Newtonian or shear thinning liquids until the velocity of the coating at the liquid-air interface is considered negligible (26).

Bénard cells have a distinctive hexagonal shape. They appear on the dried surface as a result of unbalanced surface tension, known as the Marangoni effect (48). They are created via circulating air patterns induced through the evaporation of solvent during drying/curing. The defect can cause irregularities on the film such as surface roughness, low gloss and uneven appearance. These unwanted cells can be prevented through lower overall film thickness, increasing viscosity, decreasing surface tension gradients across the surface, or increasing the drying time (26,45).

Fat edges (picture framing) are an accumulation of the coating around the edge of the coil as a strip or bead. Around the edges, surface tension gradients occur due to differences in the drying/curing times of the coating at different substrate locations. Increased surface tension at edge regions causes a flowing stream of paint from lower surface tension areas to travel to the higher surface tension area. Thus, causing areas of paint to accumulate at the edges. By adding silicones or other surfactants it is possible to reduce surface tension gradients and reduce the effects of fat edges (45).

Cascade instability is a defect affecting the surface finish of a film, often called seahorses or herringbone. The irregular, wave-like patterns propagate unevenly with the flow, which can lead to uneven film thickness on the coated substrate. It is caused by the wetting line moving through the nip gap. Thus, the metering is done at the smallest area of the nip gap, which tends to be smaller than the target coating thickness to be applied. This defect cannot be stabilised until the wetting line moves back upstream (49,50).

Ribbing is an uncharacterised coating instability, identified as periodic marks on the steel substrate that lies parallel to its direction of travel and is associated with high speed of application and/or high liquid viscosity. The undesirable effect occurs as the meniscus profile becomes non-uniform in the direction of the roller's axes (51,52). Capillary number, applicator roll speed, coating gap between rollers, the hardness of the roller cover and coating viscosity can all play a part in the onset of ribbing instability.

2.6 Coating applications for hot-dipped galvanised steel

Numerous manufacturing techniques are available to provide enhanced surface properties to galvanised steel. In reviewing these, the focus was on those which are liquid in nature with the scope to fit within the operational window of a chemcoater's operability. Appropriate coatings demand viscosities within the range of 0.5 mPas to 5 mPas, film thickness in the range of 0.06 mm to 0.08 mm and minimal additional downstream processes (53).

2.6.1 Hexavalent chromium-based passivation treatments

Corrosion resistance is of high importance for galvanised steel within the coil coating industry. Corrosion of galvanized steel has long been a proven problem for the industry and thus the development of chromium-based passivation treatments was introduced (2). Passivation can be defined as treating a surface to become more chemically inactive/inert to its environment (41). Historically, chromatation layers were applied to the outer zinc layer to act as an efficient anodic inhibitor, lowering zinc dissolution and as an effective cathodic inhibitor, lowering the rate of oxygen reduction at the metal's surface (2). Due to strict regulations imposed by the European Union regulation, REACH, the use of chromium-based treatments has been curtailed due to chromium's adverse health effects.

Hexavalent chromium-based conversion coatings (Cr^{6+}) are historically the most successful, most widely used and one of the earliest treatments used to passivate zinc-alloy and galvanized surfaces (42,54). These conversion coatings are able to convert the metal surface into a superficial outer layer containing a mixture of chemical compounds (including Cr), which in turn provide excellent corrosion resistance and paint adhesion (54). Corrosion resistance benefits can even be observed for scratched and abraded surfaces due to chromium's leachable self-healing effect when moisture is present (55). The degree of protection is generally proportional to the applied film thickness of the coating, with thicker coatings providing greater resistance than thinner coatings. The adhesion of additional coatings (i.e. paints, lacquers and organic finishes) to chromate conversion coatings is very high, due to good initial adhesion and protective nature that prevents subsequent loss of adhesion due to under-film corrosion (54,55).

Excess heating of chromate films above 66°C can dramatically decrease their protective value through two different mechanisms. Firstly, heating can cause insolubility of hexavalent chromium, rendering its corrosion resistance properties ineffective. Secondly, the shrinking and cracking of the film during heating can damage the physical integrity of the barrier. However, the heat resistance of chromate films has been shown to improve with the addition of some posttreatment "sealers" (55).

The contact resistance of substrates with chromate conversion coatings is lower than substrates that have not been treated and have been corroded or oxidised at the surface. The thinner the applied coating, the lower the contact resistance. Therefore, a compromise must be made around the coating thickness if the substrate is intended to be used for electrical use (55). The utilisation of mechanical fasteners like bolts and rivets on chromium parts can cause localised damage to the chromium film, this will have an adverse effect on the corrosion resistance of these areas and the ability of the film's self-healing properties (55).

2.6.1.1 Formation of chromium-based coatings

The mechanisms that are mostly accepted throughout the academic field are expressed below. From Cr^{6+}, predominantly CrO_4^{2-} ions are formed in the acidic solution. The process involves the oxidation of the zinc matrix, whilst simultaneously transitioning zinc ions to the solution and causing the evolution of hydrogen (56).

$$2CrO_4^{2-} + 16H^+ + 3Zn \rightarrow 2Cr^{3+} + 3Zn^{2+} + 8H_2O \tag{7}$$

$$Cr^{3+} + 3OH^- \rightarrow Cr\,(OH)_3\downarrow \tag{8}$$

2.6.1.2 Detrimental health effects

Historically, hexavalent chromium (Cr^{6+}), was the species utilised in conversion coatings for several decades. Chromium is a pervasive environmental contaminant that is highly toxic and Cr^{6+} is classified as a group one carcinogen with multiple complex mechanisms that can trigger the development of cancer. Workers within industrial processes such as metal refinement and chrome-plating/coating are subjected to two times the usual chromium exposure that the general population is subjected to, obviously posing severe health risks. Exposure to Cr^{6+} includes toxic and carcinogenic effects via a multitude of complex mechanisms including promoting oxidative stress, epigenetic changes, chromosome/DNA damage and potentially mutagenesis (57).

2.6.2 Chromium-free passivation treatments

Unfortunately, chromium-based passivation treatments are still one of the best options for surface passivation due to their high-performance characteristics. However, the scope for developing efficient Cr-free passivation treatments is vast and in recent years there has been lots of research conducted. Alternatives to Cr-based treatments include phosphate-based, molybdate-based, vanadate-based replacements and more. Some of the possible alternatives demonstrate considerable potential almost matching the performance of chromium-based treatments if only some small improvement is made (42,56,58).

2.6.2.1 Phosphate-based

Phosphate conversion coatings on zinc-based materials can be separated into two different types of processes. The first process can be identified as primary alkali (heavy metal) phosphating, where a conversion coating is formed on the base substrate. These conversion coatings generally have excellent microstructure for surface painting applications. However, zinc-aluminium alloys prove particularly difficult to phosphate, this is due to Al acting as a negative catalyst in the phosphating process, therefore, the inclusion of fluoride is necessary to produce aluminium fluoride precipitate (42,56).

The chemical reaction for when metal dissolution is initiated by phosphoric acid is observed in equations (9) – (12). Contact with phosphoric acid in solution causes initial hydrogen evolution. Thereafter, soluble phosphate present within the solution causes a localised rise in pH. This rise subsequently causes primary, secondary and tertiary precipitates to be formed. Soluble phosphates and insoluble tertiary phosphates are precipitated as blocking layers on to the cathode surface as a protective coating. This coating offers passivation to the substrate and also can be utilised to enhance lubricity, promote adhesion and increase wear resistance (59,60).

$$Zn + 2H_3PO_4 \rightleftarrows Zn(H_2PO_4)_2 + H_2 \qquad (9)$$

$$Zn(H_2PO_4)_2 \rightleftarrows ZnHPO_4 + H_3PO_4 \qquad \text{(Primary)} \qquad (10)$$

$$3ZnHPO_4 \rightleftarrows Zn_3(PO_4)_2 + H_3PO_4 \qquad \text{(Secondary)} \qquad (11)$$

$$3Me(H_2PO_4)_2^- \rightleftarrows Me_3(PO_4)_3 + 4H_3PO_4 \qquad \text{(Tertiary)} \qquad (12)$$

The second process is known as pseudo-phosphating and has attracted considerable attention within industry, due to the excellent protection obtained through optimisation of the crystalline structure formed at room temperature. The mechanism for this process can be seen below when iron phosphating is utilised (56):

$$4Fe^{2+} + 3H_2PO_4^- \rightleftarrows FeHPO_4 + Fe_3(PO_4)_2 + 5H^+ \quad (13)$$

$$Zn + Fe(H_2PO_4)_2 \rightarrow ZnFe(HPO_4)_2 + H_2 \quad (14)$$

Formation of the phosphate coating relies on the oxidation of zinc surfaces and the simultaneous transition of zinc ions to the solution, followed by hydrogen evolution. This causes a change in pH levels, altering the dissociation equilibrium and causing the formation of HPO_4^{2-} and PO_4^{3-}. Phosphating is dependent on concentrations of Zn^{2+}, Fe^{2+}, HPO_4^{2-} and PO_4^{3-} built up at the surface interface (56,61). This process is demonstrated by the schematic in Figure 10.

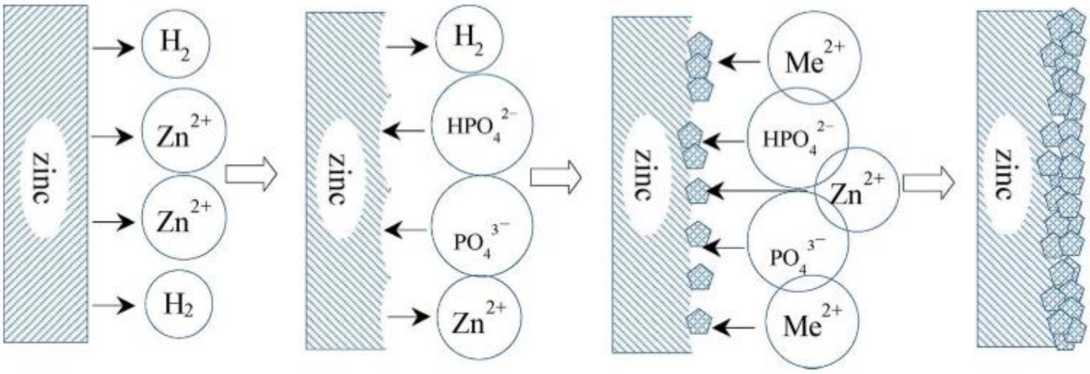

Figure 10. Visual representation of pseudo-phosphating process on zinc surface (56).

2.6.2.2 Molybdate-based

The addition of molybdates (Mo) to solutions is an environmentally viable option for inhibiting corrosion, making it a possible chromium-free alternative for passivation treatments (62,63). There is widespread speculation over the exact species present on molybdate surfaces and their mechanisms. However, it is generally accepted that the majority of molybdate coatings inhibit corrosion of zinc surfaces involving an electrochemical reduction mechanism, with almost all coatings containing Mo(IV), Mo(V), or Mo(VI) species (56). Although corrosion is inhibited by Mo, its performance is currently still lower than that of chromium-based treatments.

Studies have been conducted to develop hybrid coatings that utilise molybdate-based conversion coatings whilst supplementing with other chemicals. One study identified a Cr-free treatment that utilised a two-roll process depositing a zinc phosphate and molybdate hybrid coating. Results demonstrated good corrosion resistance when both coatings were used. Although the phosphate provided the bulk of the corrosive resistance layer, both coatings were necessary due to weak areas left from the crystallization of the zinc phosphate. Thus, the molybdate coating acted as a sealant and was able to identify and repair the voids during the secondary coating process (64).

Another study identified the performance of molybdate/phosphate/silicate-coated electroplated galvanised steel using a POLFIT programme. The programme was created in line with ASTM STP 1188, for analysis and interpretation of electrochemical impedance data (65). By measuring current corrosion densities and interpreting Tafel slopes, a reduction in corrosion current density was found, resulting in an increase in the protection efficiency of the substrate This reinforces that molybdates may be used as a good passivator of HDG steel, especially when paired with synergistic additions (56,65).

2.6.2.3 Additional passivation treatments

Vanadates have been shown to exhibit very similar chemical properties to chromium in terms of corrosion resistance. They show promising inhibition of corrosion, especially for zinc within an aqueous solution (66). Vanadate conversion coatings (VCC’s) are applied to substrates by utilising the chemical treatment of a vanadium salt, such as ammonium/sodium/potassium metavanadate, dissolved in a water solution. It is thought that VVC’s contain mostly V(V), V(IV) species and their hydrates. The excellent corrosion protection of VCC’s may be related to the barrier coating quality and leaching of V(V) species from base coatings (67). Despite vanadate-based coatings' feasibility for corrosion inhibition, the V(V) species exhibit extremely complex aqueous chemistry, which in turn makes its application very challenging in industrial applications (56).

Application of group IV(B) metal hydrofluoric acids and their salts are also promising alternatives for the corrosion resistance of zinc. These coatings appear iridescent due to their interference effect, with thick coatings being darker colours like matt black or dark brown and thinner coatings appearing grey. IV(B) metal ions undergo hydrolysis in an alkaline medium spontaneously. To acidify the solution, in industrial applications, phosphoric acid is used as an additive (56). They are commercially available and cost-effective, however, pose some limitations as they are deemed environmentally detrimental.

Silane-based coatings demonstrate exceptional adhesion to metal substrates, by forming strong cross-polymeric bonds on the surface. This provides good corrosion resistance for the base substrate. Silanes effectively protect substrates as a result of their good chemical reactivity, hydrophobic behaviour, siloxane cross-link network and film thickness. In addition to this silanes are also considered environmentally friendly, making them a favourable alternative to chromium-based treatments. Silanes with self-assembled monolayers are particularly attractive for corrosion protection applications. This is due to the many advantages of organic polymers, such as ease of processing, good mechanical properties, increased functionality by the incorporation of organic or inorganic mixtures, good hardness, thermal/chemical stability and transparency (56,68).

2.6.3 Functional coatings

Historically, conventional coatings applied to substrate surfaces have had the main purpose of passivation and/or decoration. However, in recent times the application of functional coatings has surged and research and industry have turned to the development of innovative, smart coatings with synergistic properties and functional capabilities. (69). Functional coatings have the ability to be utilised within many different industrial environments due to their potential for enhanced durability, improved chemical/thermal stability and greater environmental sustainability (70–72).

Within the galvanised steel industry there are many customer requirements, good surface qualities and resistance to corrosion are apparent, but other characteristics, like optimal enhanced lubricity and formability for post-processing, are also highly desired and can be achieved via a range of different functionalities. The use of thin polymeric coatings can be used on substrates, the coatings exhibit functional properties, including self-lubricating, self-cleaning, anti-fingerprint, and static-free properties improving the substrate's performance. This demonstrates how the use of organic and inorganic compounds with significant constituent additions can provide important functionalities for zinc substrates (73,74).

2.6.3.1 Hybrid Sol-Gel

Hybrid sol-gel coatings have seen particular interest as they can provide many benefits to the substrate surface. They can demonstrate significant corrosion resistance, adhesion promotion, coating flexibility, abrasion resistance, low hazard tom health and great thermal stability (10,75,76). They can be prepared in aqueous or organic media via a hydrolytic or nonhydrolytic method respectively, with both methods providing different characteristics and properties. These characteristics are determined by adjusting parameters within the coating, including: the composition of reactive species, organic functionalisation of species, the temperature of combinations, time taken to manufacture and pH level of constituents (10). The sol-gel process is based on the hydrolysis and condensation reactions of metal alkoxides, where M = Si, Ti, Zr, or Al; and R = alkyl group (methyl, ethyl, butyl, etc.) this is demonstrated below (75,76):

Hydrolysis reaction:

$$R\text{-}Si(OR)_3 \leftrightarrow R\text{-}Si(OH)_3 \tag{15}$$

Condensation reaction:

$$\text{-}Si\text{-}OH + HO\text{-}Si\text{-} \leftrightarrow \text{-}Si\text{-}O\text{-}Si\text{-} + H2O \tag{16}$$

The formation of sol-gel coatings typically follows four stages: hydrolysis, condensation/polymerisation (monomers forming chains), growth of chains and particles and agglomeration of networks where the gel thickens and forms. Sol-gel films display great characteristics for paint adhesion, however, are susceptible to cracking at higher coating weights. Thus, hybrid sol-gel coatings have been developed to combine inorganics/ceramics with organic polymeric materials. Corrosion resistance is dependent on obtaining crack-free films and although the hybrid sol-gel films offer several advantages, there are still limitations associated with reduced wear resistance and lower mechanical properties (10).

2.6.3.2 Enhanced lubricity coatings

Lubricating coatings when applied to sheet metal can aid in the attainment of low adhesion, low friction and subsequently low surface damage. This can be particularly desirable for substrates before post-manufacturing forming processes. They work to reduce the material's coefficient of friction and as a result, wear effects during the drawing process are reduced, tool loads are reduced, and material pick up on surfaces can be avoided (77,78).

Dry film lubricants that have been developed have demonstrated higher deep drawing performances and cleaner press shop environments and have been shown to have some significant advantages over other conventional oil lubricants even when used in challenging circumstances like high temperature and vacuum (78,79). In the case of dry film lubrication, the mechanism employed is ‘boundary lubrication’. Boundary lubrication is often referred to as the 'classical' approach to lubrication and utilises freely supported multimolecular layers of liquid lubricants at the surface boundary (77). Pure boundary lubrication is shown in Figure 11. A lubricant film, even if only a few molecular layers thick, prevents interference between the two surfaces (77–83).

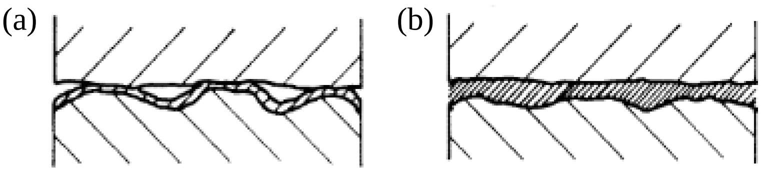

Figure 11. Comparison between lubrication mechanisms in metal forming: (a) Boundary lubrication (film thickness not to scale) and (b) Solid-film lubrication (80).

There has been gathering attention around the use of sulphate and sulphonate ions as lubricants and they have been shown to induce a strong reduction in friction and wear. An environmentally friendly lubricant was investigated by Lovell et al. to aid the sheet metal forming process. The lubricant was composed of solid boric acid particles within a matrix of canola oil as an additional lubricant due to their eco-friendly nature as well as independently demonstrating good lubrication potential (84). This study identified that significant friction reduction was observed when a solid lubricant within an oil matrix was used, due to reduced metal-to-metal contact, something particularly poignant for the metal sheet-forming process. More recently, a study investigated the use of ammonium sulphate treatment to improve the tribological performance of hot-dipped galvanised (HDG) steel by creating a Zn/ZnS solid lubricant matrix (85). Timma et al. found that when an ammonium zinc sulphate complex was produced on the surface in addition to a thin lubrication film, superior frictional properties were observed. Figure 12 shows a schematic displaying the sulphate and lubricant mixture seen by Timma et al. This illustrates how the ZnS matrix may assist the reduction of friction by acting as a lubricating barrier between the metal to metal surface, assisting movement.

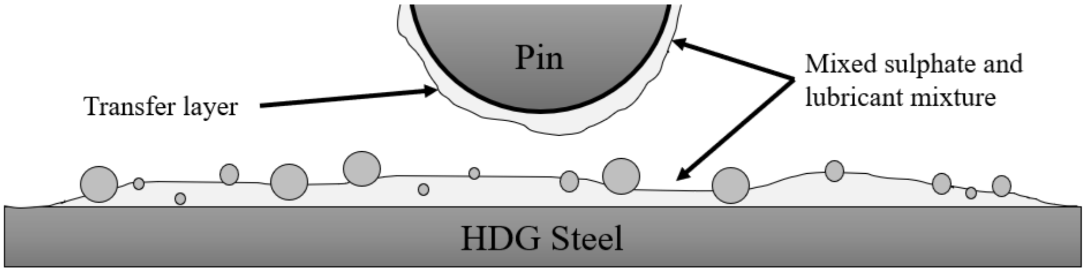

Figure 12. Schematic displaying lubrication and sulphate mechanism observed from Timma et al (85).

This coating poses many significant benefits due to improving the frictional performance of the metallic surface, via a simple and effective procedure. Furthermore, there is minimal negative impact on users and the environment, due to the coating's low toxicity and simple chemistry. Thus, there is particular interest in exploring the use of a ZnS matrix.

2.6.3.3 Hydrophobic coatings

Hydrophobic surfaces are assessed by having a large CA and by definition superhydrophobic surfaces (SHS) must have a CA greater than 150° (86–88). SHSs have been shown to provide effective corrosion protection on a range of metallic substrates, such as steel (89,90), copper (91), magnesium (92) and zinc (93–97). Water repellency/adhesion is directly related to the contact angle hysteresis (CAH) and the force required to start a droplet moving over a solid surface:

$$F = \gamma_{lv} (\cos(RCA) - \cos(ACA)) \tag{17}$$

Where F is the critical force per unit length, γ_{lv} is the liquid-vapour interfacial surface tension, RCA is the receding contact angle and ACA is the advancing contact angle. CAH is the difference between ACA and RCA and thus shows how surface wettability and CAH are related (74). There has been growing interest in the use of hydrophobic coatings (HCs) to improve the corrosion resistance of metallic substrates and to provide functionality, such as self-cleaning (86,97–101). These coatings are inspired by the natural surface of lotus leaves, which have nano-structured surfaces coated with low-surface-energy materials that provide an interface between the coating and liquid (102). The interface is created by retaining the air within the nano-scale topography of the surface, which reduces the contact area of water droplets, producing a highly non-wetting, low-adherence surface where dirt particles are only able to lie at the very tip of the structures. Thus, dirt particles that may contaminate the surface develop low adhesion forces and are removed easily and effectively (100,101,103,104).

The preparation of superhydrophobic coatings on metallic substrates can be achieved using a variety of methods, such as electrodeposition, chemical etching and hydrothermal growth (101,105–108). However, many of these methodologies require complex two-step processes that would be difficult to implement in an industrial application. Due to these issues, there have been recent advances to develop simple one-step methods to produce a superhydrophobic surface. Li et al. implemented a one-step immersion method to produce a superhydrophobic coating on zinc using a solution of stearic acid containing silver nitrate (109).

The coating was applied at room temperature within 1 min, and the reported results indicated excellent corrosion protection; however, the use of silver nitrate would be prohibitive for industrial applications due to cost. Chen et al. used a rapid one-step electrodeposition process to produce a superhydrophobic coating on copper using a nickel chloride-based electrolyte solution. The resulting surface was reported to achieve up to a 164° contact angle and less than a 2° rolling angle; however, the corrosion resistance was not reported (110).

Liang et al. produced a superhydrophobic coating on a zinc surface implementing a simple one-step hydrothermal growth technique using stearic acid and silicon dioxide (SiO_2) particles (88). The authors reported excellent corrosion performance when the coating was immersed in an aqueous sodium chloride solution and contact angle measurements were recorded of up to 160°. The zinc layer on the surface of hot-dipped galvanized (HDG) steel reacted with stearic acid to form low surface energy zinc stearate. The chemical reaction for this is observed below (88):

$$Zn - 2e^- = Zn^{2+} \tag{18}$$

$$Zn^{2+} + 2CH_3(CH_2)_{16}COOH = Zn[CH_3(CH_2)_{16}COO]_2 + 2H^+ \tag{19}$$

The corrosion resistance of the hydrophobic coating was previously studied by Liang et al. using EIS and potentiodynamic polarisation demonstrating the coating's excellent resistance to corrosion. However, the coating required up to 6 h to form, which would be impractical for industrial applications. There would be significant interest within industry, if this coating technique, employing a simple one-step hydrothermal growth method using stearic acid and silicon dioxide particles, processing time could be reduced. The methodology described by Liang et al. provides a foundation for further improvements to reduce the time required to produce a suitable coating, thereby, making the coating more appropriate for industrial applications (88).

The hydrophobic coating produced via the method proposed by Liang et al. utilised nano-SiO_2. This additive is deemed expensive and potentially hazardous for industrial applications. There lies a significant interest in the use of larger particle size SiO_2, which is more readily available and commonly used in organic coatings, which could provide a viable alternative (111).

2.6.3.4 Self-healing coatings

Self-healing coatings actively repair themselves through the release of a specific repairing agent after changes to the integrity of the coating, as a result of mechanical/chemical damage or from changes in the environment surrounding it (changes in temperature, UV, pH, etc.). For a coating to be deemed self-healing, the repairing process must occur automatically, without extra human interaction.

Therefore, coatings must have an intrinsic capacity to recover automatically after damage occurs. Self-healing coatings can provide two methods of protection after damage. Passive protection, whereby layers of the corrosion product act as a barrier against corrosion and active protection, where protective species are generated from inhibitors (74).

2.6.3.5 Functional properties of coating additives

The use of specific additives within coatings can be highly beneficial in influencing a coating's properties. Table 3 demonstrates potential chemical additions that could provide valuable properties to coatings, such as the ability to aid in corrosion resistance, increase hydrophobicity and provide anti-bacterial properties.

Table 3. Potential chemical additives and their properties that can be utilised in coatings.

Chemical addition	**Size (nm)**	**Supplier cost (INSCX £/g)**	**Anti-corrosion**	**Hydrophobic**	**Lubricating**	**Anti-bacterial**	**Abrasion resistant**	**Self-healing**	**Fire retardant**
SiO_2	10 - 30	0.35 – 0.45	✓	✓	✓	✓	✓	✗	✓
CeO_2	80	2.85	✓	✓	✗	✗	✗	✓	✗
MoS_2	35 - 45	1.65	✓	✗	✓	✓	✓	✗	✗
Bentonite	< 80	0.5 – 2.75	✓	✗	✗	✓	✗	✗	✗

As previously discussed, Liang et al. have shown that HDG steel coated with a combination of Stearic acid and SiO_2 can effectively improve its corrosion protection and greatly increase the hydrophobicity of a substrate's surface (88). The addition of SiO_2 fabricated coating showed excellent water repellency due to its hydrophobicity and greatly improved corrosion resistance.

The inclusion of MoS_2 within coatings has proved to be particularly interesting due to its high anticorrosion performance and potential anti-fouling properties. Protection of a mild steel matrix was shown to be highly effective by combing MoS_2 with a hybrid pigment, before adding it to a waterborne epoxy (112,113). Additionally, MoS_2 nanotube coatings have a superb low frictional performance which is why they are ideal for anti-wear and extreme pressure components and are regularly used in machining and forming applications. Interfacial interaction between MoS_2 and Zn-coated components was studied to understand the important synergy between the two elements. This interaction was important to understand to benefit the future development of nanofluid minimum quantity lubrication formulations. Results from the studies showed MoS_2 interacted favourably with the Zn coating to form a tribological surface with superb frictional performance (114).

Recent developments have seen innovation around synthesis pathways which include novel polymer–nanoclay composites. The improved properties, provide a potentially lucrative coating for diverse fields such as aerospace, automotive and construction (115). Enhanced properties include improved density, increased strength, relatively large surface areas, high elastic modulus, fire resistance and magnetic/thermomechanical/optoelectronic properties. Thus, meaning the potential for nanoclay composite coatings is vast. In addition to this, their relatively low cost, low environmental impact and wide availability provide even greater incentive to adapt these potential coatings for many applications (115,116).

Three synthesis methods: solution-blending, melt-blending and in-situ polymerization are known for configuring nanoclays within coatings. The low viscosity and high agitation power of solution-blending can often lend itself to more favourable dispersion of clay layers within the polymer matrix when compared to melt blending. However, melt blending is an eco-friendly and industrially viable technique that has the potential for high economic growth. In-situ polymerization is the final method, which allows an ability to modify polymerization conditions (115).

2.7 Summary

In summary, this literature review provides an overall insight into the coating of hot-dipped galvanised steel. Some key findings have been discussed throughout this chapter, including:

- The hot-dipped galvanising process, its corrosion resistance and why there is a need for additional coating.
- The rheology of materials, paying special attention to the key characteristics of coatings such as viscosity, elasticity, rigidity and plasticity, that determine how a material deforms or flows.
- The surface chemistry and adhesion properties of coatings, to understand the interfacial behaviour between two materials and give an insight into the mechanisms between a solid-liquid coating interface.
- The coil coating process paying special attention to the role of the direct and reverse roll coating process, operability and common defects.
- Specific coatings applications for HDG steel, highlighting areas of key interest for future HDG steel treatment.

The literature has influenced the direction of this research project. Firstly, it has highlighted the need to gain a greater understanding of current treatments utilised by the chemcoater system at Tata Steel. Gaining an overall assessment of current treatments will enable an in-depth understanding to be had on their performance, as well as provide valuable benchmark criteria for future potential treatments. The literature research has demonstrated the current underutilisation of coating applications utilised by Tata Steel. The highlighted underutilisation of these treatments can be attributed to several factors, high research and development costs, and regulatory compliance challenges can hinder industry to implement technologies easily. Additionally, resistance to change by manufacturers and a lack of awareness around the potential benefits/implications of novel coating technologies can hamper their adoption. Therefore, this research highlights the opportunity for novel coating applications of hot-dipped galvanised steel to provide further functionality and add value to the overall product for Tata Steel.

3 Experimental procedures

3.1 Strategy

Understanding surface behaviour is crucial within coating technology. The surface of a coating is the first thing to interface with the environment and its reactivity determines how well the material behaves for its intended function. Therefore, it was important to have techniques that enabled users to analyse a surface's properties. To understand these properties and the surface's reactivity, information such as: topography, chemical structure, chemical composition, electronic state, atomic structure and molecular bonding may be required. No one technique can be used to find all of this information and thus a collection of techniques can be used (117).

Throughout this project, several parameters were needed to be studied. It was identified through literature that many methods would be appropriate for evaluating materials and specifically coating characterisation. Each method explained, was utilised to provide valuable metrics in determining results throughout this research. The key experimental procedures and methods utilised throughout this research including physical, chemical, tribological and electrochemical techniques are showcased.

3.2 Sample manufacturing

3.2.1 Cleaning procedure

All substrate samples were cleaned thoroughly to mimic industrial conditions (118). Initially, all prepared samples were rinsed with de-ionised water and ethanol respectively to remove excess dirt and debris. Afterward, samples were immersed in 1M NaOH solution at 50°C for 15s, rinsed again with de-ionised water and allowed to air dry before coating.

3.2.2 Coating procedure

It was imperative to ensure the material viscosity of the coating was in the 0.5 mPas to 5 mPas range for it to be considered a suitable option for the roll coating process. Material viscosity that exceeded these parameters could result in detrimental phenomena as shown in section 2.5.

All sulphate-coated samples were manufactured via spin coating. After cleaning, 1ml of coating formulation was deposited into the centre of a 50 × 50 mm coupon and spin-coated at 5000 RPM for 30 s to produce a uniform coating. Coupons were then placed in a convection oven at 180 °C for up to 30s, to achieve a peak metal temperature of 80°C. After which, coupons were removed and cooled in ambient conditions at room temperature.

To fabricate the hydrophobic coatings a one-step immersion method was used. The coating formulation used either ethanol, isopropyl alcohol (IPA) or L-butanol as the solvent. The formulation was prepared by adding 0.05 M stearic acid to 100 mL of the relevant solvent. Hydrogen peroxide (2 mL) was added dropwise to the formulation whilst magnetically stirred for 1 min. Silicon dioxide (1% wt.) was added to the formulation and magnetically stirred for 30 min to ensure the stearic acid was fully dissolved and the silicon dioxide was evenly dispersed. Macro and nano-scale silicon dioxide particles were utilised. The formulation was heated and held at 70 °C using a hotplate before HDG samples were immersed for up to 360 min. The samples were then removed, rinsed with ethanol and blown dry.

3.3 Physical characterisation

3.3.1 Scanning electron microscopy

Scanning electron microscopy (SEM) is widely used for examining the microscopic structure of a material’s surface and provides an analytical approach that is not highly time intensive. SEM utilises an electron gun, which accelerates a condensed electron beam in the voltage range of 1-40kV for intricate probe scanning of surfaces. The beam is directed through a series of electromagnetic lenses and a deflection system allows the electron beam to raster over the specimen's surface. Detectors collect backscattered and secondary signal electrons emitted from elastic and inelastic scattering respectively. These signal electrons are amplified and used to reproduce an image that has a similar appearance to a traditional microscopic image but a much greater depth of field (119,120).

Throughout this research, SEM images were taken using a Hitachi TM3000 and Hitachi TM4000 microscope. All images were taken using 15 kV acceleration voltage at a working distance of approximately 10 mm unless otherwise stated.

3.3.2 Energy dispersive spectroscopy

Energy dispersive spectroscopy (EDX) uses x-rays emitted from specimens after radiation from primary high-energy x-rays. A photon detector characterises the x-ray photons according to their energies. The detector collects signals of characteristic x-ray energies from a whole range of elements in a specimen rather than analysing individual x-ray wavelengths. The x-ray spectrum data collected consists of several peaks which represent the type and relative amount of each element in the sample. Furthermore, the number of counts in each peak can be further processed into elemental weight concentrations and compared with industry standards (119,120). These peaks can be used to identify specific areas of elements present in the accompanying microscopic images, which makes it a useful tool for identifying certain areas of an image.

Throughout this research, EDX analysis was done using Quantax70 software (Oxford Instruments) paired with Hitachi TM3000 and Hitachi TM4000 microscope. Each scan was run for 12 minutes.

3.3.3 Atomic force microscopy

Atomic force microscopy (AFM) provides a profilometry technique in all three dimensions. It translates signals for surface topography by utilising near-field forces between atoms of the probe tip apex and the surface of a sample. Operational modes of AFM are generally divided into static and dynamic modes. In static modes the cantilever physically comes into contact with the surface, statically deflecting to a certain degree. The feedback loop maintains this set value of deflection throughout the scanning period. Dynamic modes include contact and non-contact methods, the cantilever oscillates at a certain frequency and the feedback loop maintains this set value of the amplitude of oscillation during scanning. Tapping mode (dynamic) is the most common method used as possible damage to the sample during scanning is significantly reduced whilst providing information on physical and chemical properties of the surface as well as topography (119,120).

The AFM configuration used to measure surface topography throughout this research was a JPK Nanowizard 3. Samples analysed were cut to an appropriate size and mounted on a glass slide. The AFM was set to alternating contact (AC) mode, with the tip vibrating at 75 Hz and a scan rate of 0.7 line/s. The benefit of using AC mode is that it eliminates lateral forces, resulting in less damage to the sample surface.

3.3.4 Digital Microscopy

During this investigation, digital microscopy was often utilised to acquire quick and accurate images and 3-D depth profiling of the surface morphology via a Keyence VHX-7000 microscope (Osaka, Japan).

3.3.5 X-ray diffraction

X-Ray Diffraction (XRD) allows the determination of crystal structure, particle size and phase composition of materials and thin films dependent on their diffraction pattern (121–123). Generally, XRD instruments include a source, primary optics, sample part, secondary optics and a detector. The technique works by scattering x-rays from a source, which are then reflected through a sample and onto the detector. The scattered x-rays interfere with each other and the atomic planes of the material resulting in partial beam transmission as well as absorbed, refracted, scattered, and diffracted x-rays. Each element diffracts the incident rays uniquely, depending on its atomic structure. By measuring this angle of diffraction and using Bragg–Brentano (parafocusing) Law various characteristics of the crystalline structure can be determined (121,122).

Throughout this research, x-ray diffraction (XRD) (Bruker D8 Discover with copper source 40 kV and 40 mA) (Billerica, MA, USA) was used to characterise surface chemical constituents. Samples were fixed in place and XRD was conducted with a glancing angle setup consisting of a 2° incidence angle in true parallel beam configuration and increments of 0.02°.

3.4 Chemical characterisation

3.4.1 Viscometry

Dynamic viscosity is generally considered an absolute viscosity measurement and shows the material's internal resistance to flow. This measurement is important for assessing a material's resistance to deformation and whether it can be appropriately used for coating application. A RheoSense MicroVISC was utilised for determining liquid viscosity. The portable rheometer utilised VROC$^{©}$ technology to accurately and repeatably measure viscosity, using a sample size of as little as 100µL. During the tests, a flow rate of 450µL/m was maintained. Varying volumes of liquid were measured. One benefit of utilising small sample volumes was that high shear rates could be achieved without flow instabilities due to turbulent behaviour.

3.4.2 Interfacial surface tension

The pendant drop method is used to measure the interfacial surface tension (ST) of a liquid, as well as the tension between two materials. Figure 13 demonstrates a typical pendant-drop profile that is analysed to find surface tension. Surface tension is given by (26):

$$\gamma = \Delta\rho g \cdot d_e/H \tag{19}$$

$$S = d_s / d_e \tag{20}$$

Where γ is the surface tension, d_e is the diameter of the pendant drop and H is related to a measurable shape-dependent factor, S. d_s is the diameter of the pendant drop in a selected plant at a distance, d_e from the droplet apex. Direct digitalisation of video images has improved the accuracy of the pendant drop technique measurements via the use of new algorithms (26).

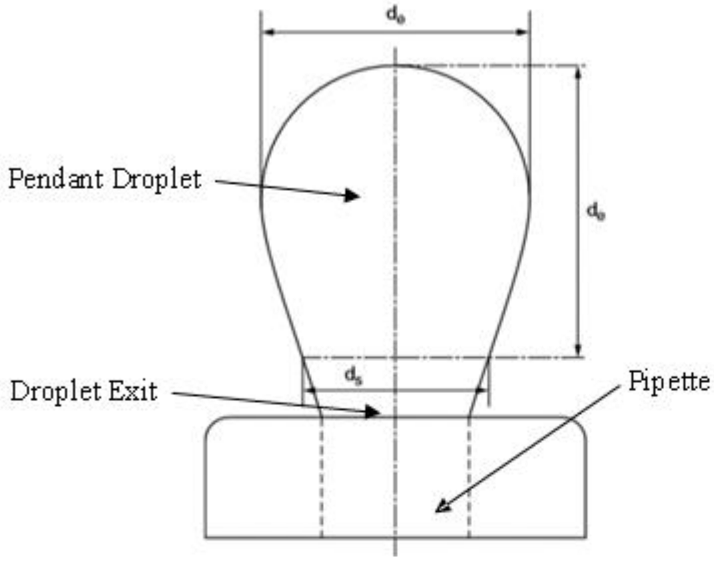

Figure 13. Typical pendant-drop profile (26).

The total attractive force acting on a molecule in the bulk of a liquid is zero, while the cohesion force exerted by a surface molecule is a nonzero quantity acting in the bulk's direction. To enlarge the surface area, this force must be overcome; the energy consumed in this process is referred to as surface energy. ST forces act to redistribute the coating layer after a coating is applied to a surface. If the coating's ST is larger than the substrate's, flaws and insufficient surface wetting may occur (30,124).

Throughout this research, a 20 µL droplet was deposited from a pipette, 20 µL was chosen as this was an easily standardised, repeatable volume to be used from a pipette during testing. The corresponding pendant drop was analysed via a goniometer system comprised of a CCD camera, and contact angle software (Software version 4.0.3.1, Osilla) (Sheffield, UK) with an error measure of ±1° under optimized illumination and optical conditions.

3.4.3 Contact angle analysis

When a liquid comes into contact with a flat surface it either dewets to form a droplet or wets and flows out. The droplet/edge of the droplet creates an angle with the solid plane, commonly known as the contact angle, θ. If the contact angle is greater than 0°, a nonwetting condition exists and the material’s intramolecular attraction is greater than the intermolecular attraction with the solid surface. Thus, the material’s surface tension value is higher than the solid’s surface energy. In contrast, if the contact angle is 0° then wetting occurs. Therefore, measuring contact angle enables us to understand the relative difference between two surface tensions and allows a quantitative method of measuring wetting between a solid and liquid medium. Smaller contact angles indicate similar (but not equal) surface tension values, whilst a large angle signifies a large departure (26).

Figure 5 shows an illustration of a liquid's ability to wet onto a solid surface, contact angle is also identified. During CA analysis, a 20 µL droplet of each liquid was deposited onto a substrate to create a droplet. Once the droplet settled at equilibrium, a goniometer system was used to analyse the CA. Two goniometer systems were utilised throughout this research to investigate CA. Both comprised a CCD camera but used two different types of analysis software (Software version 4.0.3.1, Osilla/FTA1000 manual system, First Ten Angstroms) (Sheffield, UK/Portsmouth, VA, USA). Both systems had an error measure of ±1° under optimized illumination and optical conditions.

3.4.4 Simultaneous thermal analysis

Simultaneous thermal analysis (STA) combines thermogravimetric analysis (TGA) with differential scanning calorimetry (DSC) to understand the thermal profile of a formulation. TGA is completed by monitoring the sample mass under controlled isothermal or linearly varying temperature by a thermo-balance. Application of this method is important in understanding a material's decomposition and thermal stability and results are depicted as mass change expressed against temperature or time (119). DSC is a method primarily used to measure the heat flow difference between a material and a reference sample. When thermal events occur in the sample, the power to the heating element has to alter to ensure the material temperature remains consistent with that of the reference sample. Endothermic events cause a required increase in power, in contrast, exothermic events require a reduction in power. The amount of power change equates to the energy of heat flow needed to compensate for heat release or gain of a sample. DSC curves are commonly recorded over a range of temperatures by heating or cooling a sample at a constant rate. DSC allows a quantitative technique in analysing enthalpy changes of a sample during a thermal event, for example, common material transitions such as: melting, crystallization and glass transition can be understood (119).

STA allows the combination of both these techniques to gain a full understanding of the thermal stability and enthalpy changes of a material. During this research, STA was completed using the PerkinElmer STA6000 (Waltham, MA, USA).

3.4.5 X-ray fluorescence analysis

XRF is a non-destructive technique used for quantitively determining the amount of an element present on a surface. XRF measurements provide a rapid and precise technique for effective quality control of elemental determinations for a variety of materials. A low-level radioisotope is placed in close proximity to the sample and primary x-rays are emitted, in turn striking the sample and causing secondary x-ray emission and fluorescence. Independent of chemical or physical state, these secondary x-rays emitted have specific wavelengths and energies that are characteristic of the elements in the sample, therefore each element demonstrates an individual, characteristic fluorescent profile. These x-rays are detected and a series of pulses are output, the amplitudes of which are proportional to the energy of the incident radiation, enabling analysis of the present chemicals to be obtained (26,119). Figure 14 demonstrates the schematic illustration of the interaction between incident x-rays and electrons during the XRF process.

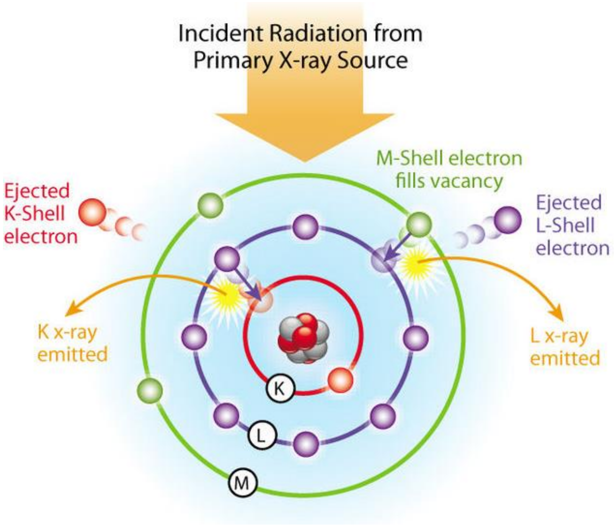

Figure 14. Schematic illustration of the interaction of incident x-rays and electrons as is observed in x-ray fluorescence analysis (125).

Understanding how much material is deposited onto the substrate after the coating process is crucial to ensuring accuracy and concurrency in results. Due to the high throughput of material and the continuous nature of coil production a quick and accurate method is needed on the line to measure sufficient material has been deposited. Thus, Tata Steel utilise XRF to monitor the coating weight of material deposited onto the substrate for quality control. It provides precise and rapid analytical data on the amount and uniformity of the applied coating.

During this project, XRF analysis was completed using a handheld Bruker S1 TITAN 600 series (Bruker) (Billerica, MA, USA). Multiple data readings were taken at equidistant points on the samples and mean values were calculated to ensure concurrent coating results were within an acceptable error margin of 1-2 mg/m^2.

3.4.6 Fourier transform infrared spectroscopy

Fourier transform infrared spectroscopy (FTIR) is a spectroscopy technique used for the identification of organic/inorganic polymeric material's molecular fingerprint. FTIR gives characteristic information on chemical environments, molecular structures, orientations and configurations of polymeric chains (121,126,127).

The technique works by passing approximately 10,000–100 cm^{-1} of infrared (IR) radiation through a sample to excite molecules. An IR spectrum of the sample is obtained as some of the radiation is absorbed and some is transmitted through. The absorbed radiation is converted to vibrational/rotational energy and the resultant signal obtained at the detector represents the samples' molecular fingerprint, which is generally a spectrum in the region of 4000 to 400 cm^{-1} (121,126). Throughout this research, FTIR spectroscopy (PerkinElmer spectrum-100) (Waltham, MA, USA) was used to characterise the surface chemical constituents.

3.5 Tribological characterisation

Tribological data is vital to quantitatively assess the frictional performance of a material and help to explain how it may behave when in physical contact with other materials. Static friction is described as a threshold value of frictional force that must be exceeded to initiate sliding. Whereas, dynamic friction is defined as the frictional force that persists during a sliding motion, under set conditions at a given speed (81). The coefficient of friction (μ) is determined by the ratio of frictional force to the normal force, acting perpendicular to the two surfaces in contact with each other. The equations for static (μ_s) and dynamic (μ_d) coefficient of friction are shown below, where, static force, normal force and dynamic force are given as F_s, F_p, F_d respectively.

$$\mu_s = F_s / F_p \tag{22}$$

$$\mu_d = F_d / F_p \tag{23}$$

3.5.1 Linear friction testing

Linear friction testing (LFT) was carried out in reference to BS EN ISO 8295:2004 to determine the static and dynamic coefficient of friction of a material film when sliding over itself (128). The principle for this analysis technique used two coupons in plane contact with each other. One coupon was immobilised into position and the other was attached to a sled and pulley system. Care was taken when handling the specimen and its surface was wiped clean of debris and dust before contact was established with the load and applied normal to the surface. The force needed to displace the surfaces relative to each other was recorded via a Hounsfield tensile tester. For all measurements, the steel samples were cut into 80 mm × 200 mm coupons and a load of 200g was utilised. All tests were carried out for a distance of 100mm over 300s, at room temperature (~ 20°C). The experimental setup can be observed in Figure 15.

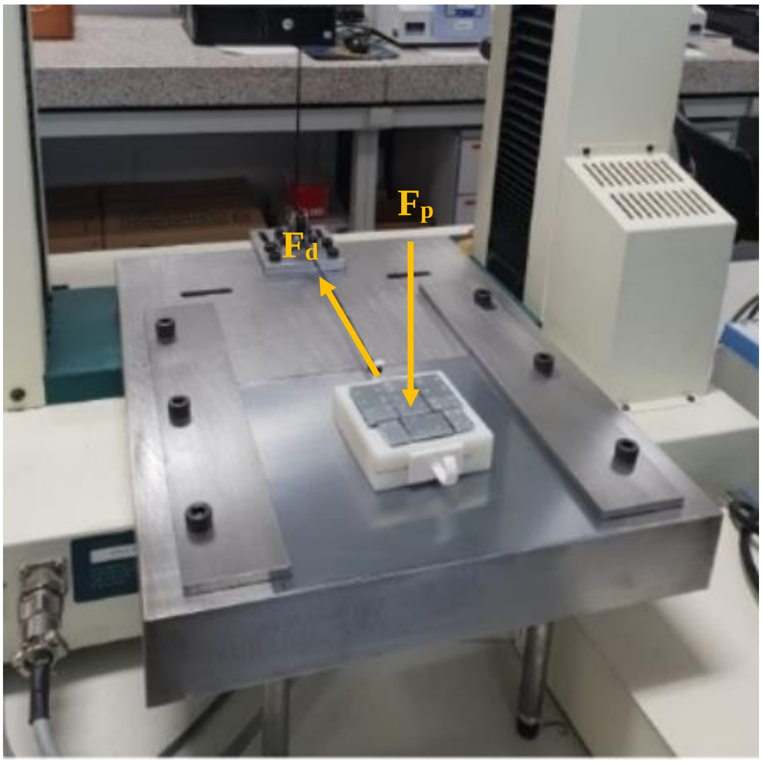

Figure 15. Linear friction testing apparatus set up compliant with BS EN ISO 8295:2004.

3.5.2 Dynamic friction testing

A method of measuring a coated substrate's coefficient of friction dynamically over a sustained period was investigated using a novel Pin-on-Disk (POD) tribometer. Conventional POD tribometers generally have two methods of measuring μ. The first method applies a loaded pin normal to a rotating surface, the second method utilises a loaded rotating surface, which is applied normal to a fixed pin. For both methods, the resulting frictional force is measured to determine the coefficient of friction. No conventional dynamic tribometer was available within the university or Tata Steel R&D laboratories. Therefore, it was decided to create an appropriate POD system, in-house. By liaising with technical staff, a novel POD system was able to be designed, commissioned, and built in reference to ASTM G99-17, to conduct dynamic tribological investigations. A schematic of the novel POD tribometer used throughout this research is seen in Figure 16.

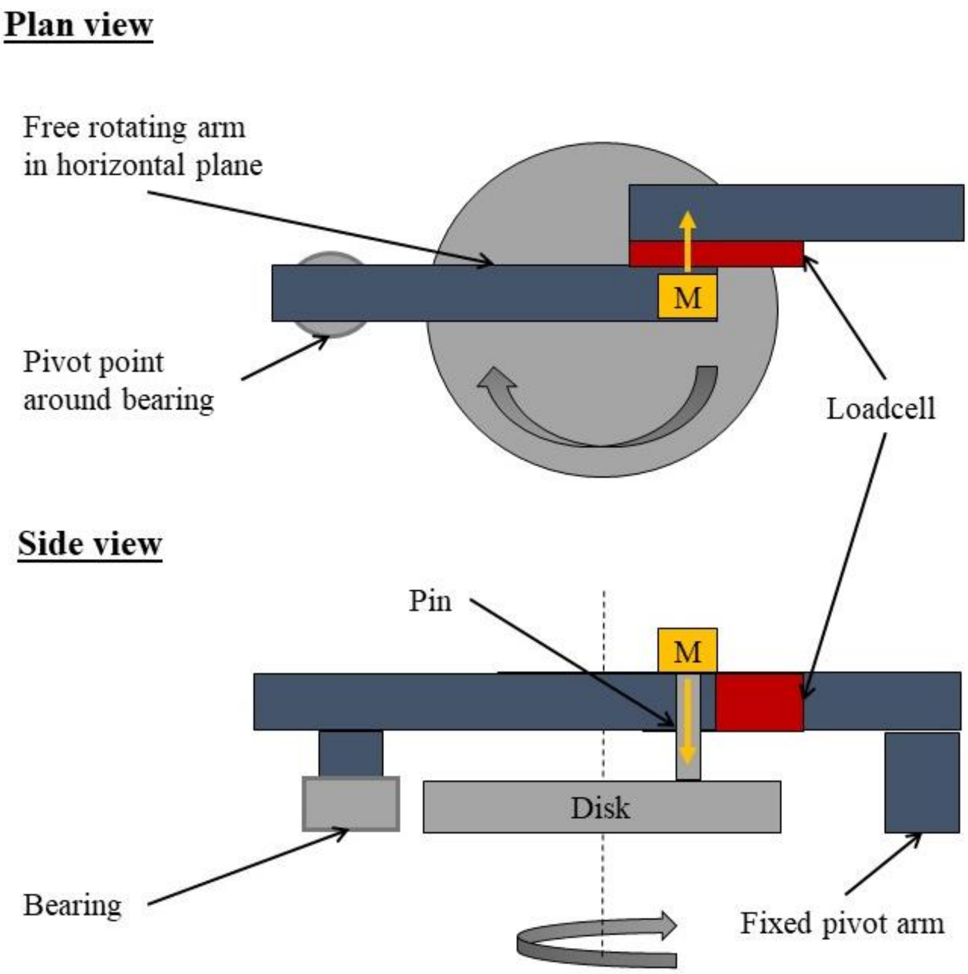

Figure 16. Schematic of novel Pin-on-Disk tribometer.

The system utilised a rotating sample stage and loaded pin. When the sample was rotated in contact with the loaded pin, horizontal displacement occurred. This displacement force (F_d) was proportional to the magnitude of the frictional force between the pin and the sample. Therefore, samples with a higher coefficient of friction elicit a higher displacement force. This method provided a repeatable technique for determining a material's dynamic coefficient of friction over a sustained period (85,129,130). Figure 17 demonstrates the novel POD tribometer built in-house and used throughout dynamic testing.

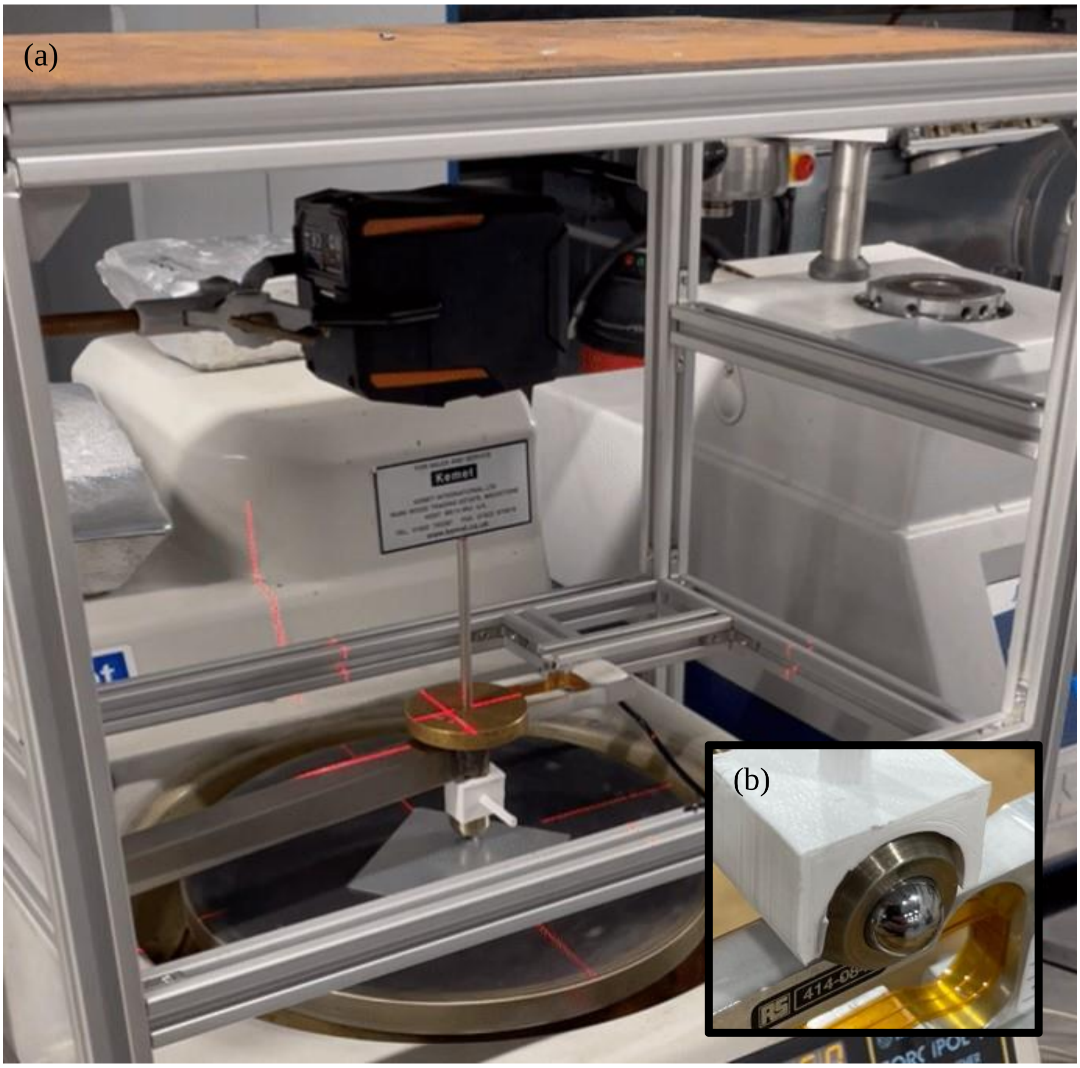

Figure 17. (a) Novel POD tribometer during testing, (b) Close up demonstrating the removable ball inserted into the pin cantilever arm.

A loaded cantilever arm with a removable 10mm diameter steel ball was utilised as the pin. The cantilever arm was attached to the system via a rigid framework with incorporated twin pillow block bearing units. The framework was freestanding and isolated above the rotating sample stage via rigid stands with incorporated noise reduction spikes to minimise external noise and vibrations from affecting results. A polishing machine was repurposed and utilised as the rotating sample stage. This machine gave an easily repeatable and achievable method of rotation, that could utilise a various range of angular speeds over a wide load range. For all measurements, samples were cut into 50 mm × 50 mm coupons and clamped into place on the rotating sample stage. Care was taken when handling the specimen and its surface was wiped clean of debris and dust before contact was established with the pin. A laser was utilised before each test to ensure repeatability when loading the pin into position at approximately 10 mm from the centre of rotation. Horizontal displacement was measured via the compression of a load cell on a fixed arm adjacent to the pin. The loadcell output millivoltages, and so was connected to a wheatstone bridge interface (PhidgetBridge 4-Input) to enable accurate and precise measurements. A compatible user interface (Visual Studio 2022, C# programming language) was designed to output the data efficiently and plot the coefficient of friction data. An additional load of 2N was placed normal to the substrate surface, which was rotated at 50 rpm, equating to a linear speed of 0.05 ms^{-1}. All tests were run for at least 150 cycles, totalling 3 min or until otherwise stated.

3.6 Electrochemical characterisation

3.6.1 Scanning Vibrating Electrode Technique (SVET)

SVET is a technique used to spatially resolve areas of dissimilar electrochemical activity, giving an insight into the corrosion activity at a specimen's surface when placed into an electrolyte. This is achieved by delivering a vibration frequency through a scanning microtip probe at a fixed height normal to a corroding surface. The probe movement is controlled stepwise by a micro-manipulator stage where a computer is responsible for three-dimensional control. A vibration frequency is delivered by a lock-in amplifier (EG&G Instruments 7265) which also serves to detect the incoming vibrating signal from the probe. As a result, the vibrating probe can detect an alternating potential at a frequency that is proportional to the potential gradient/electric field strength in the direction of vibration (131–133).

For SVET analysis conducted throughout this research, extruded PTFE tape (type 5490 HD, 3 M) was used to expose a 100 mm^2 area in the centre of each sample, allowing for a scan area of 8 × 8 mm. Driving frequency was delivered by the lock-in amplifier at a frequency of 140Hz to produce a probe vibration of 25 µm at a scan height of 100 µm. The SVET probe was scanned perpendicular to the surface of the sample, which was immersed in 1% w.t. NaCl solution at a temperature of 20°C for 24 hours.

The output of SVET experiments was exhibited via isocurrent contour maps of ionic current density distribution over the sample surface. Potential fields are created in solution when ionic current flux from any anode on the corroding surface passes through the electrolyte. Areas of positive current, associated with anodic activity, are shown as red and areas of negative current, associated with cathodic activity, are shown as blue.

SVET does have resolution limitations, which have been previously considered in literature (134–136). The vibrating frequency in SVET determines the proximity to the sample's surface, affecting sensitivity and spatial resolution. Changes in frequencies can provide fluctuations in data, ultimately altering the proximity of the vibrating electrode to the sample's surface. Abrupt or extreme frequency changes can introduce mechanical disturbances, potentially compromising measurement stability and accuracy. The SVET's spatial resolution refers to the probe's capacity to gauge the distance between two localised corrosion areas. SVET’s theoretical spatial resolution can be determined by the full-width half-maximum (whm) of the signal peak. A scan height of 100 µm is utilised used throughout this research and thus a theoretical resolution of 153 µm would result. However, whm for the SVET used throughout this research is observed at ~260 µm in practice, when the scan height is 100 µm (134). This discrepancy is in part attributed to the dimensions of the probe itself (~125 µm) and somewhat explains how localised corrosion features within this distance may not be spatially resolved.

3.6.2 Electrical Impedance Spectroscopy (EIS)

Electrical Impedance Spectroscopy (EIS) is a leading technique in evaluating a substrate's impedance to corrosion degradation and delivers the ability to quantitatively gain electrochemical analysis data. To understand the fundamentals of EIS, it is important to start with electrical resistance, R. The concept of electrical resistance is the ability of a resistor to resist the flow of electrical current, I, when a voltage is applied, V. The relationship between these components is described by Ohm's law:

$$R = V / I \tag{24}$$

When applying Ohm's law, the limitation is that the resistor is considered 'ideal' which has several simplifying properties: its resistance value is not dependant on frequency, AC and voltage signals must be in phase with each other, and it must follow Ohm's law at all current and voltage levels. However, in real-world scenarios, circuit elements do not behave ideally and exhibit much more complex behaviour. Impedance, Z, measures the ability of a circuit to impede the flow of an alternating current, therefore:

$$Z = V_{ac} / I_{ac} \tag{25}$$

The magnitude of Impedance, alongside frequency, f, and phase angle, °, can be plotted against each other to demonstrate a Bode Plot. In contrast, when the impedance is measured at several frequencies and plotted on Cartesian axes, a Nyquist plot is represented (137). These plots can give a quantitative assessment of a material and highlight key characteristics such as polarisation resistance, R_p and coating capacitance, $C_{Coating}$ (137–139).

Throughout this research, EIS experiments were conducted with a Gamry Instruments Interface 1010E^{TM} (Warminster, PA, USA). A standard three-electrode cell was employed and incorporated coated steel samples as a working electrode, a platinum gauze counter electrode and a saturated calomel reference electrode. An area of 10 cm^2 was targeted whilst, the input AC amplitude was 10 mV and the frequency range was from 0.05 Hz to 100 kHz. Impedance spectra were obtained at 1 h intervals and plotted via Nyquist plots to illustrate the results.

3.6.3 Humidity testing

Humidity testing provides additional corrosion resistance analysis and enables a “real-life” high-humidity environment to be mimicked within a laboratory setting. High-humidity environments and cyclic temperatures can accelerate the corrosion process rapidly by causing condensation at the substrate surface and initiating corrosion sites.

Throughout this research, humidity testing was completed in line with Standard ASTM D2247-15, where samples were placed at 45° and held at 35 °C and 100% humidity. The investigation was conducted for up to 1000 h. At intervals of 0, 250, 500 and 1000 h a Canon EOS 5D camera within a lightbox was used to photograph the corroded samples, mass measurements were also taken of each sample. Cut edges of the samples were sealed with marine-grade epoxy resin, and the water uptake of the resin was negated for and deducted from the final mass values of the samples. Water uptake was measured by conducting a control experiment. The mass of the control sample was recorded over a period of time, measuring the mass increase of marine-grade epoxy after intervals. The data was utilised to calculate the mean value of mass increase due to water uptake within the epoxy sample after being placed into the humidity cabinet.

3.7 Error estimations

Due to the variability in the coating, errors can occur within the distribution of results across all experimental procedures. Coating variability can occur due to many reasons such as processing errors, substrate chemistries/conditions and formation chemistries/conditions. All of which can play a decisive role in coating stability and effectiveness. To combat these discrepancies in results, repeated sample manufacturing was imperative to ensure additional measurements could be made.

Additionally, repeat testing was vital to ensure accurate, repeatable and concurrent results were obtained throughout all analysis techniques. Repeat readings were executed to obtain the mean, standard deviation and standard error values. The standard error is an important metric to understand the variability in a set of results. This allowed the standard deviation of the sample distribution to be calculated and gave a clear understanding of how consistent that specific data set was. Standard error, SE, was calculated via the equation:

$$SE = S / \sqrt{n} \tag{26}$$

Where S is the standard deviation of the data set and n, is equal to the sample number. Graphically, the standard error was plotted on figures as error bars. This displayed an easily identifiable visual cue of the variability from the mean results recorded.

In general a meticulous effort was undertaken to reduce potential errors throughout testing, all equipment was regularly calibrated and repeated protocols were followed in order to ensure accuracy and concurrency within results. When outliers were recorded, they were either excluded or transformed depending on further statistical analysis. This was in order to maintain transparency throughout results and maintain accuracy in data acquisition.

3.8 Summary

The techniques introduced throughout this chapter provided the ability to obtain valuable metrics when analysing the performance of a material. The key experimental procedures and methods showcased have been used to gain physical, chemical, tribological and electrochemical characteristics. The first use of these techniques is given in the next accompanying research chapter.

4 Characterisation of current chemical surface treatments for hot-dipped galvanised steel employed by a chemcoater

4.1 Introduction

Corrosion of hot-dipped galvanised (HDG) zinc coated steel is a recognised issue within the construction and automotive industries whereby they are exposed to a wide variety of atmospheric conditions. Historically chromium-based passivation treatments were employed to improve substrates' corrosion resistance. The term passivation refers to a chemically inactive surface film on steel that limits the dissolution of the metal surface via the anodic reaction. In the case of HDG steel, the passivation layer is typically formed via Zn cations interacting with limited solubility anionic species, like oxides, phosphates or chromates. However, due to hexavalent chromate's toxicity and in accordance with significant REACH legislation changes, Tata Steel has changed to the use of non-hexavalent chromate coatings on their products (2,41,140).

Lubricants can be applied to metallic substrates to reduce the material's coefficient of friction. As a result, wear effects during the drawing process are reduced, tool loads are reduced, and material pick-up on surfaces is avoided. When working with complex automotive panel geometries, dry film lubricants have been developed and implemented and research has shown notable advantages over other conventional oil lubricants like higher deep drawing performance and cleaner press shop environments (78). In addition to this, their exceptional performance even in challenging circumstances like high temperature and vacuum, means they have drawn a lot of interest from the tribological community (79). A lubricant film, even if only a few molecular layers thick, prevents interference between the two surfaces. In the case of phosphating, the thin crystalline coating acts as a boundary layer, lowering the coefficient of friction between the two surfaces' asperities (78–83).

Tata Steel have the opportunity to utilise two industrial coatings via a chemcoater: PrimeCoat and PLT (Prime Lubrication Technology). PrimeCoat is a proprietary treatment developed and produced by the Quaker Chemical Corporation. It was developed as a passivation treatment for HDG steel to aid corrosion resistance before transportation and storage. Currently, this is the only coating regularly used by the chemcoater at Tata Steel’s ZODIAC galvanisation line. PLT was developed as a dry film lubricant and implemented by Tata Steel post galvanising at sites in Ijmuiden, Netherlands. The principal aims of this research chapter are:

- To study the coating chemistries of PrimeCoat and PLT to assess their similarities and differences.
- To investigate whether PLT could be utilised by Tata Steel on their ZODIAC site and easily interchanged with PrimeCoat without sacrificing productivity.
- To gain a comprehensive understanding of the characteristics and performance of both PrimeCoat and PLT.

4.2 Materials and methods

4.2.1 Materials

4.2.1.1 PrimeCoat

PrimeCoat Z801-017/75 is a water-based Cr-free passivation product specifically used for corrosion protection of hot-dipped galvanised sheet steel. PrimeCoat’s chemical composition includes: Polyphosphoric acid (5-7%), nitric acid (1-2.5%), phosphoric acid (1-2.5%) and pyrophosphoric acid (1-2.5%). PrimeCoat serves as a functional coating in which the constituent elements chemically react with the galvanised substrate’s zinc surface, forming a non-metallic, crystalline coating (59). Table 4 compares both PrimeCoat's and PLT’s key characteristics.

Table 4. Key characteristic data for PrimeCoat and PLT.

Name	**Appearance**	**pH**	**Target coating weight (P, mg/m^2)**
PrimeCoat	Off-white	1.4	50-80
PLT	Off-white (translucent)	1.8	5-8

4.2.1.2 PLT

PLT was developed for deposition on automotive sheet steels as a dry film lubricant to reduce the material’s coefficient of friction and in turn, reduce susceptibility to tribological defects. The coating was manufactured by AD Chemicals and Quaker Chemicals and the composition mainly includes phosphoric acid and aluminium orthophosphate. PLT is intended to be washable (with alkaline reagent) so that, if necessary, it can be removed before further phosphating or painting processes. PLT has no chemical bonding mechanism and upon deposition, dries on the steel substrate's surface in crevices to create a boundary layer.

4.2.2 Methods

4.2.2.1 Sample Manufacturing

PrimeCoat samples were manufactured utilising as-coated HDG samples provided by Tata Steel (ZODIAC, Llanwern, Wales) where they were appropriately cut into 50 × 50 mm coupons. PLT samples were manufactured via spin coating. 20 ml of PLT was diluted and magnetically stirred in 80 ml of de-ionized water in a 1:4 ratio. 1ml was deposited on 50 × 50 mm HDG coupons and spin-coated at 5000 RPM for 30 s which produced a uniform coating. Coupons were then placed in a convection oven at 180 °C to achieve a peak metal temperature (PMT) of 80°C for 30 s.

4.2.2.2 XRF analysis for sample manufacturing

In-house manufactured samples’ coating weight was monitored to ensure consistent and homogeneous coating layers. XRF analysis (Bruker S1 TITAN 600 series) (Billerica, MA, USA) was conducted by identifying the weight of the tracer element, Phosphorus, per metre square of the substrate. Target coating weights for PrimeCoat and PLT coated samples were 50-80 mg/m^2 and 5-8 mg P/m^2 respectively. Data readings were taken at three equidistant points on the samples and mean values were calculated to ensure concurrent coating results were within an acceptable error margin of 1-2 mg/m^2.

4.2.2.3 Characterisation techniques

Surface morphology and analysis of the surface was visualised using scanning electron microscopy (SEM) (Hitachi TM3000) (Tokyo, Japan) equipped with electron dispersive spectroscopy (EDX) as well as using digital microscopy (Keyence VHX-7000) (Osaka, Japan). Simultaneous thermal analysis (STA) (PerkinElmer STA6000) (Waltham, MA, USA) was carried out to evaluate the thermal stability and enthalpy changes of the coatings. The dynamic viscosity (RheoSense MicroVISC) (San Ramon, CA, USA) was assessed to understand the rheological properties. The surface energy of the coatings were determined by analysing coatings in contact with HDG steel substrates. The goniometer system comprised of a CCD camera, and contact angle software (Software version 4.0.3.1, Osilla) (Sheffield, UK) with an error measure of ±1° under optimized illumination and optical conditions. Throughout all characterisation both PrimeCoat and PLT samples were analysed at room temperature (~20°C) unless otherwise stated.

4.2.2.4 Tribology investigation

Static friction is described as a threshold value of frictional force that must be exceeded to initiate sliding. Whereas, dynamic friction is defined as the frictional force that persists during a sliding motion, under set conditions at a given speed (81). The coefficient of friction (μ) is determined by the ratio of frictional force to the normal force, acting perpendicular to the two surfaces in contact with each other. The equations for static (μ_s) and dynamic (μ_d) coefficient of friction are given:

$$\mu_s = F_s / F_p \tag{27}$$

$$\mu_d = F_d / F_p \tag{28}$$

Where,

F_s = static force, N

F_p = normal force, N

F_d = dynamic force, N

4.2.2.4.1 Linear friction testing

Linear friction testing (LFT) was carried out in reference to BS EN ISO 8295:2004 to determine the starting and sliding coefficient of friction of a material when sliding over itself. The principle of using this LFT setup is to place two pieces of known material in plane contact with each other and apply uniform pressure, the force needed to then displace the surfaces relative to each other was recorded, to calculate the material's coefficient of friction (128).

4.2.2.4.2 Dynamic friction testing

A method of measuring the coated substrate's coefficient of friction dynamically over a sustained period was investigated using a novel Pin-on-Disk (POD) tribometer. No conventional dynamic tribometer was available within the university or Tata Steel R&D laboratories. Therefore, it was decided to create an appropriate POD system, in-house. By liaising with technical staff, a novel POD system was able to be designed, commissioned, and built in reference to ASTM G99-17, to conduct dynamic tribological investigations. A schematic of the novel POD tribometer used throughout this study is seen in Figure 16. As has been previously discussed, samples with a higher coefficient of friction elicit a higher displacement force. This method provided a repeatable technique for determining a material's dynamic coefficient of friction over a sustained period (85,129,130). Figure 17 demonstrates the novel POD tribometer built in-house and used throughout dynamic testing.

For all measurements, steel samples were cut into 50 mm × 50 mm coupons and clamped into place on a rotating sample stage. Care was taken when handling the specimen and its surface was wiped clean of debris and dust before contact was established with the pin. A laser was utilised before each test to ensure repeatability when loading the pin into position. Horizontal displacement was measured via the compression of a load cell on a fixed arm adjacent to the pin. An additional load of 2N was placed normal to the substrate surface, which was rotated at 50 rpm. All tests were run for at least 150 cycles, totalling 3 min or until otherwise stated.

4.3 Results and Discussion

4.3.1 Surface morphology

The surface morphology of samples was initially analysed using digital microscopy. Given the off-white appearance of both PLT and PrimeCoat, they are both difficult to be seen via the human eye. Due to PLT’s translucent appearance and much lower coating weight, it is much harder to see when deposited onto the substrate surface. PrimeCoat’s heavier coating weight enables an off-white coating to be observed, as is shown in Figure 18.

Figure 18. Digital microscopy of PrimeCoat coated HDG surface at ×20 magnification (2mm scale).

As described in Table 4, both PLT and PrimeCoat have an off-whitish appearance, with PrimeCoat being more obvious to the eye in comparison to PLT’s translucent appearance. Due to the off-white appearance of both PLT and PrimeCoat, higher magnification images do not display the coating homogeneity well and thus a high scale of 2mm was utilised for initial digital microscopy.

Figure 19 and Figure 20 display SEM and EDS images of PLT and PrimeCoat on coated HDG steel. It can be observed from the EDS layered maps that the primary element found is Zinc, Zn. The presence of this Zn is expected due to the hot dipped zinc coating layer of the steel. The other notable element observed for both coatings is Phosphorus, P. P is well distributed over both samples and especially apparent with the crevices and disparities of the Zn coating layer. This is attributed to both PLT and PrimeCoat layers and thus gives a familiar method of analsying the coatings alongside XRF to investigate coating layers and homogeneity.

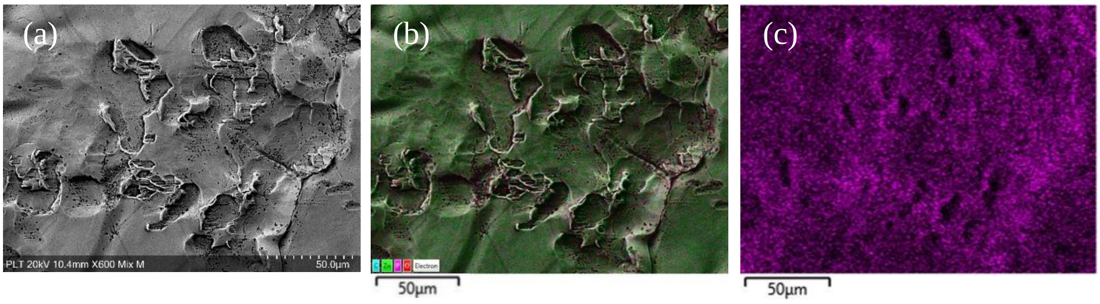

Figure 19. (a) SEM image of HDG coated with PLT layer, (b) EDS layered map of notable elements present on sample, (c) EDS map of Phosphorus element, showing where it is present.

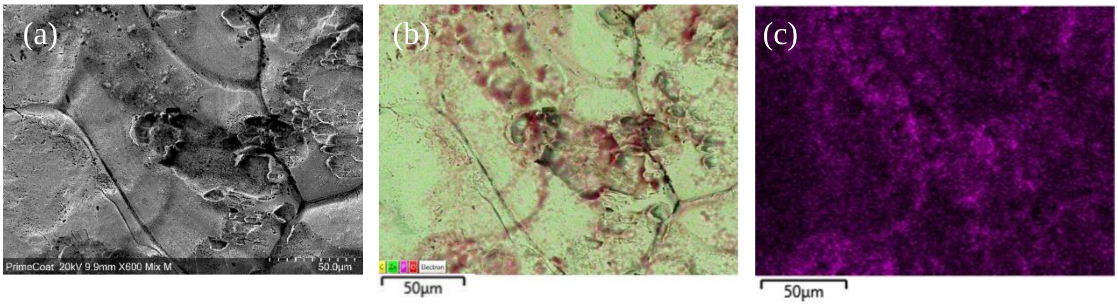

Figure 20. (a) SEM image of HDG coated with PrimeCoat layer, (b) EDS layered map of notable elements present on sample, (c) EDS map of Phosphorus element, showing where it is present.

4.3.2 Rheology

The dynamic viscosity of both PrimeCoat and PLT was measured using a RheoSense MicroVISC. Results from the rheometer tests are presented in Figure 21. During the tests, an average room temperature of 20°C was recorded and a flow rate of 450 μLm^{-1} was maintained. Varying volumes of liquid were measured from approximately 55-130 µL. One benefit of utilising small sample volumes is that high shear rates can be achieved without flow instabilities due to turbulent behaviour, leading to greater accuracy when measuring.

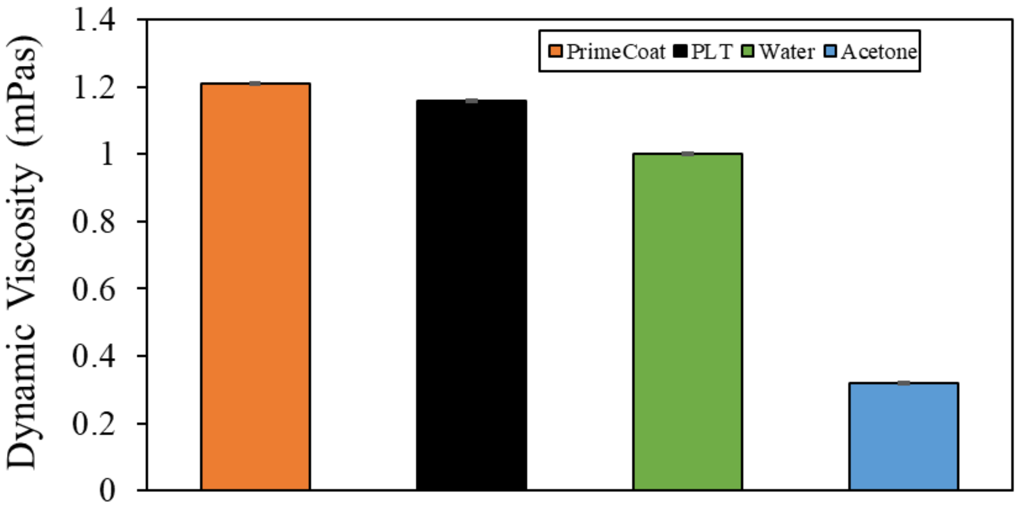

Figure 21. Dynamic viscosity data of applied coatings in comparison to common fluids (27).

The average dynamic viscosity of PLT and PrimeCoat was measured at 1.16 mPas and 1.21 mPas respectively. It was observed that the viscosity of PLT and PrimeCoat demonstrate viscoelastic behaviour similar to that of water and thus it can be assumed in practice that both coatings will behave with almost Newtonian-like behaviour. This information contributes to understanding how the coatings may behave in practice and help to predict certain behaviours particularly when coating on an industrial line.

4.3.3 Surface energy

4.3.3.1 Interfacial surface tension

The sum of all attractive forces acting on a molecule in a liquid's bulk is zero. The cohesion force of a surface molecule is a nonzero number acting in the direction of the bulk. To enlarge the surface area, this force must be overcome; the energy consumed in this process is referred to as surface energy. Surface tension (ST) is expressed as surface energy per unit area. ST forces act to redistribute the coating layer after a coating is applied to a surface. If the ST of the coating is greater than that of the substrate, the coating can be susceptible to incomplete surface wetting and defects (30,124).

Interfacial surface tension measurements were conducted utilising the pendant drop method, by analysing the liquid droplet as it formed into a spherical shape from a pipette. Images of the droplet were captured via a CCD camera, allowing for computational analysis. For analysis, the last frame before the droplet fell was analysed. This can be observed in Figure 22 (a). Initially, de-ionised water was used to obtain a baseline value. An average ST value was recorded at 70.1 mNm^{-1}. The same process was carried out for calculating the ST of PLT and PrimeCoat, whereby a droplet of material was analysed before falling from the pipette. The average ST of PLT and PrimeCoat was recorded at 53.9 mNm^{-1} and 30.6 mNm^{-1} respectively, as observed in Figure 23. These values allude to both PLT and PrimeCoat demonstrating a greater ability to wet to HDG steel's surface, with the former showing the greatest ability to wet efficiently.

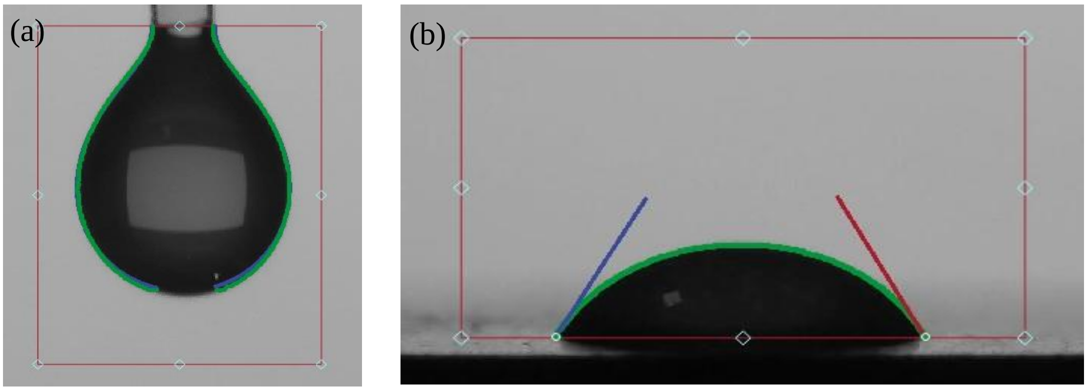

Figure 22. Example of: (a) Pendant drop method and (b) Contact angle method of analysis of PLT using Osilla goniometer software.

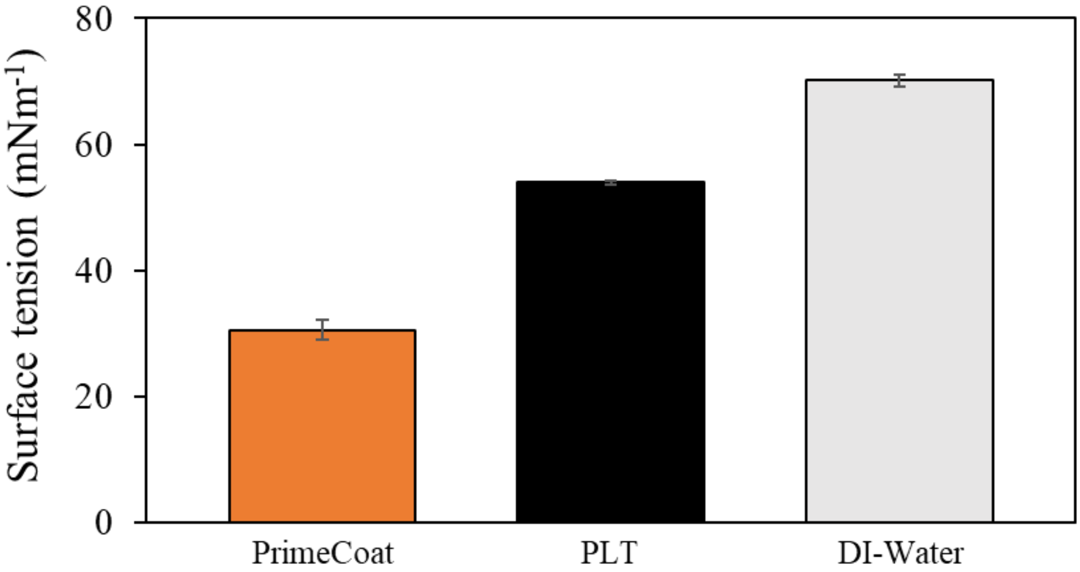

Figure 23. Mean interfacial surface tension values of PrimeCoat, PLT and DI-Water.

4.3.3.2 Contact angle

Contact angle (CA) analysis gives a quantitative measurement of wetting by analysing the interface between solid and liquid mediums. HDG steel samples were appropriately degreased and cleaned before CA analysis was conducted by depositing 20 µL of each formulation onto each coupon of HDG steel. Images of the droplet were captured via a CCD camera, allowing for computational analysis. Data was recorded after the liquid droplet had settled towards an equilibrium point at approximately 10s and 60s. An image of the contact angle analysis software can be observed in Figure 22 (b). The CA data is depicted graphically in Figure 24.

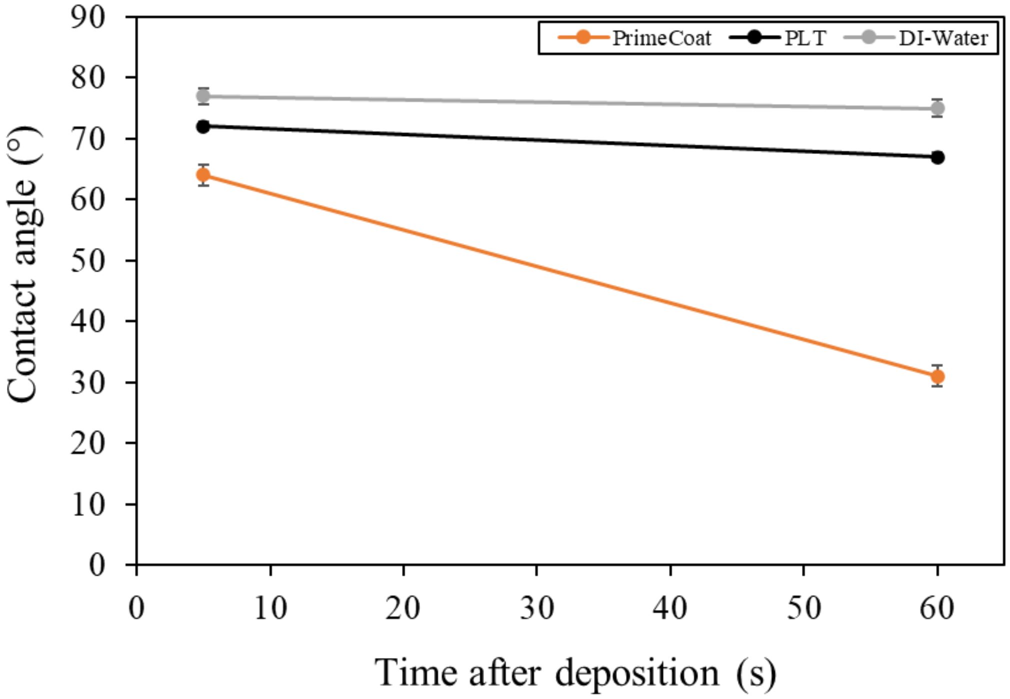

Figure 24. Contact angle against time for PrimeCoat, PLT and DI-Water as they interface with galvanised surface.

Initially, DI-Water was used as a baseline value. Mean CA of three samples, 10s after deposition was first recorded at 77° and reduced to 75° after 60 s. When comparing the two coatings, it can be observed both initial CA values reduce over a sustained period. In addition to this, the CA of PrimeCoat on initial deposition was significantly smaller than PLT, showing a greater tendency to wet to the steel surface (level out). The average CA of PLT when in contact with HDG steel's surface was first recorded at 72° and reduced to 68° after 60 s. In comparison, the CA of PrimeCoat was first recorded at 64° and reduced to 31° after 60 s, showing a significant reduction in CA with increased time.

Both PLT and PrimeCoat demonstrate a higher affinity to wet to the HDG surface in comparison to DI-Water. Furthermore, PrimeCoat shows a significantly higher tendency to wet to the surface in comparison to PLT. Therefore, it can be hypothesised that PLT has stronger intramolecular attraction between its molecules, with dispersion happening at a slower rate. This shows that PLT has a greater difference in surface tension between itself and the HDG steel's surface, in comparison to PrimeCoat (141).

4.3.4 Simultaneous thermal analysis

Characterising the thermal stability and enthalpy changes of the two coatings is key to understanding their drying profiles. Figure 25 and Figure 26 show thermogravimetric analysis (TGA) and differential scanning calorimetry (DSC) data for PrimeCoat and PLT when tested over a 90 min period. Both coatings display almost identical thermal behaviour, which is largely due to their high water content and formulation similarities. TGA displays that both coatings behave similarly between 20°C – 90°C, and material weight percentage decreases with increasing temperature. PrimeCoat is seen to follow this decay until approximately 96°C, where only 5% of coating material remains, after this point the material weight percentage plateaus, regardless of the increase in temperature and thus the change recorded is negligible. Therefore, it can be assumed most of the material mass is removed before this point.

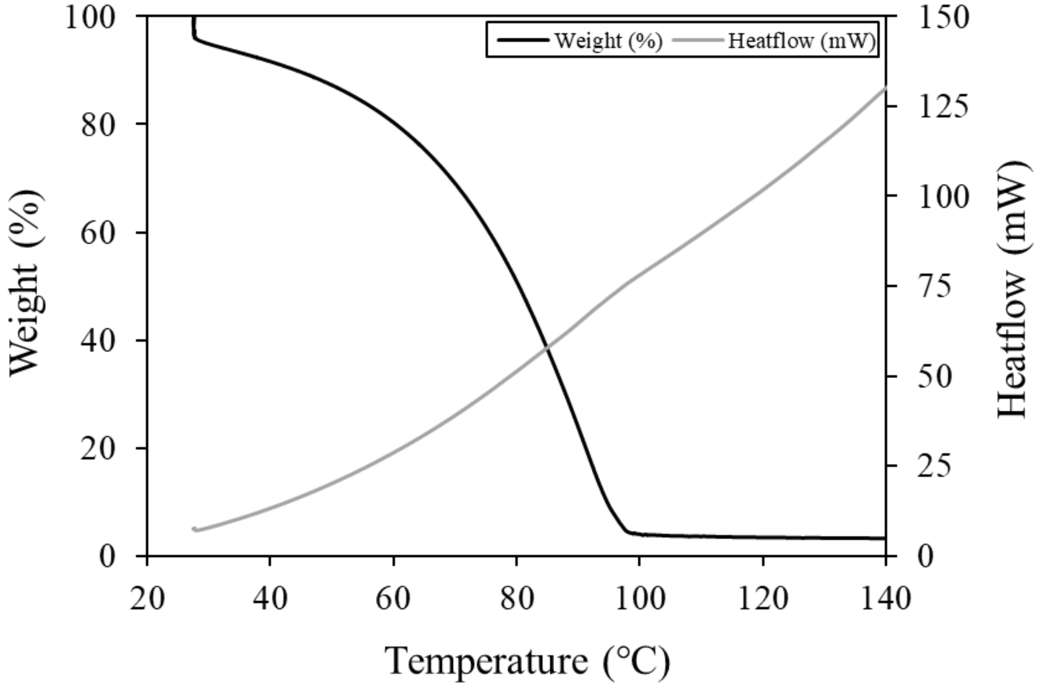

Figure 25. Simultaneous thermal analysis data obtained for PrimeCoat.

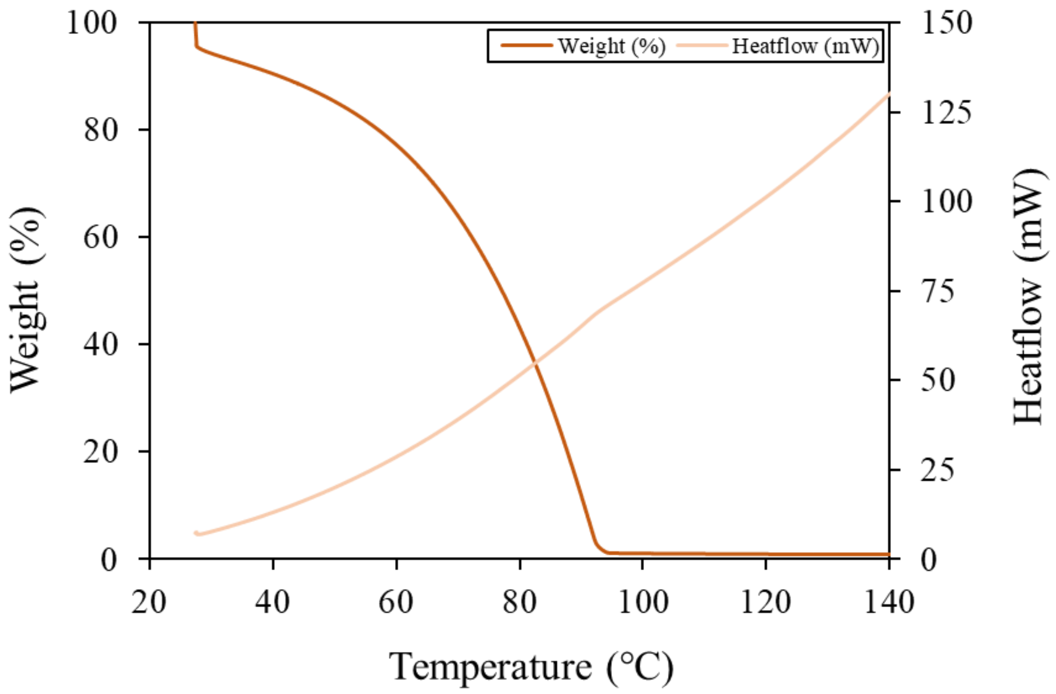

Figure 26. Simultaneous thermal analysis data obtained for PLT.

PLT displays similar behaviour and like PrimeCoat, upon heating, weight percentage experiences negative decay until a plateau point is reached at approximately 93°C, where 2.5% coating material remains. A similarity between the two coatings is that the majority of the material weight percentage is lost before the samples are heated above 100°C, this may be attributed to the evaporation of water, present in the coatings.

DSC data demonstrates that for both PrimeCoat and PLT, increased temperature sees an increase in heat flow. Again, PrimeCoat and PLT demonstrate almost identical behaviour, both curves show an inflection point at approximately the same temperature weight percentage begins to plateau (approximately 96°C and 93°C respectively). This endothermic inflection reinforces that there is a change in state and that all water has been evaporated from the sample. Table 5 illustrates some key data points from STA.

Table 5. Key data points observed from simultaneous thermal analysis of PrimeCoat and PLT.

Coating	**Drying temperature (°C)**	**Heat flow required to cause change in state (mW)**
PrimeCoat	96	74.1
PLT	93	69.5

Both coating chemistries demonstrate very similar drying temperatures and energy requirements to reach a change in state. This data positively reinforces that both coatings should behave similarly when used on an industrial coating line, like that at ZODIAC. This is beneficial as it suggests different drying programmes will not be necessary for the two coatings and therefore, they can be easily interchangeable, increasing efficiency and reducing downtime.

4.3.5 Tribology

4.3.5.1 Linear friction testing

Linear friction testing was conducted by coupling two coated coupons together and holding them in plane contact with each other. One coupon was immobilised into position and the other was pulled across the other's surface via a pulley and sled system. The recorded force was then utilised to calculate the coefficient of friction, μ. It is observed that the frictional behaviour of PLT and PrimeCoat are different. Three tests were completed for each coating and a mean coefficient of friction was recorded at 0.16 and 0.35 with a standard error of 0.01 for PLT and PrimeCoat respectively. PrimeCoat recorded a noticeably larger μ value in comparison to PLT. Figure 27 demonstrates the mean coefficient of friction recorded for each coating.

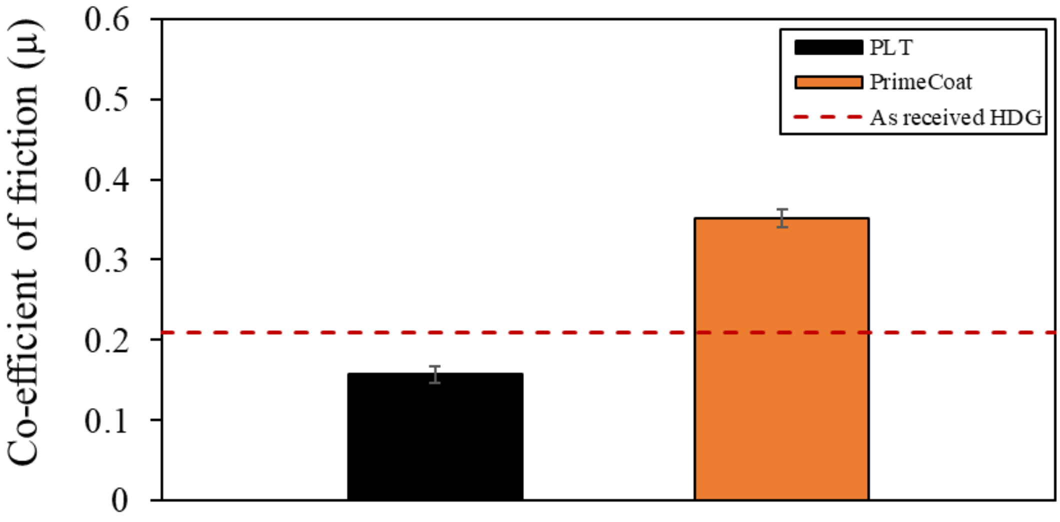

Figure 27. Mean coefficient of friction data from LFT.

As a pre-lubrication layer, PLT must display reduced frictional properties across its surface. By reducing the coefficient of friction over the substrate surface the strain distribution experienced in the forming process by manufacturers will be different from that of its PrimeCoat counterpart. The success of the forming process is often dependent on this strain distribution, as a lower coefficient of friction will enable lower stamping forces to be utilised in the forming process. A more lubricated surface will enable higher formability of parts, in turn reducing overall energy consumption in the forming process and minimising the risk of damaging the substrate and forming tool (142).

Figure 28 demonstrates a typical profile reading recorded from the linear friction test. Both coatings behave reasonably linearly with time and show similar µ values throughout the testing period. PLT experiences a slight increase in µ around 200s, this slight rise is likely where the coating has experienced degradation, due to its very thin nanolayers and it is likely breakthrough has started to occur. Regardless of this inflection, the PLT sample still records considerably lower µ values than its PrimeCoat counterpart, even after suspected breakthrough. Additionally, it is observed that the coefficient of friction profile for PrimeCoat experiences more sporadic behaviour, this is also suspected due to the coating homogeneity of the PrimeCoat layer, its thickness is in the order of microns thus meaning there may be more variability in overall surface roughness, affecting its frictional performance over time.

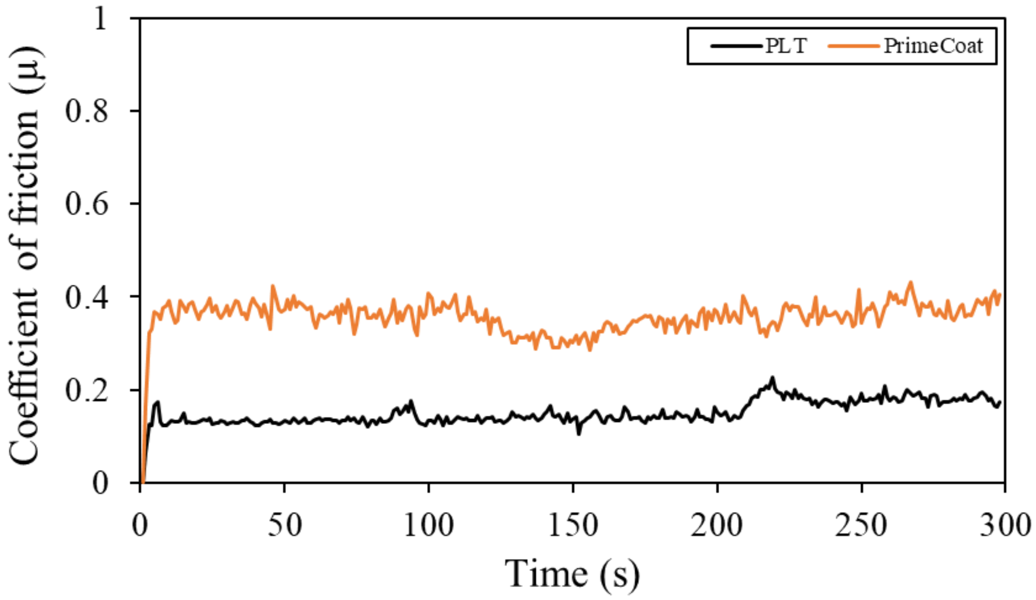

Figure 28. Example of coefficient of friction data of both PrimeCoat and PLT for 300s from LFT.

The LFT results conclude that PLT as a pre-lubrication layer may significantly enhance hot-dipped galvanised steel's surface resistance to friction and aid positively later on during the forming process. In comparison, PrimeCoat's increased frictional behaviour at the surface will negatively impact the forming process and thus should be removed before further processing to negate surface defects.

4.3.5.2 Dynamic friction testing

Dynamic friction testing (DFT) was completed utilising a novel Pin-on-Disk setup. The data collected from DFT reinforces the results obtained during LFT. Samples were tested for both PrimeCoat and PLT at varying coatings weights, as measured by XRF analysis, where P was the tracer element and measured in mg/m^2. Various coating weights were analysed to understand the effect coating weight would have on tribological performance. Despite coating weights for PLT and PrimeCoat ranging from 8.7 – 28.6 mg/m^2 and 45.5 – 77.9 mg/m^2 respectively, there was little variation in µ measured over the sample sets. The mean coefficient of friction was recorded at 0.17 and 0.36 with a standard error of 0.01 for PLT and PrimeCoat respectively. As was observed in LFT, PLT recorded a significantly lower µ value in comparison to PrimeCoat and as received, uncoated HDG steel. Figure 29 demonstrates the mean coefficient of friction for each coating.

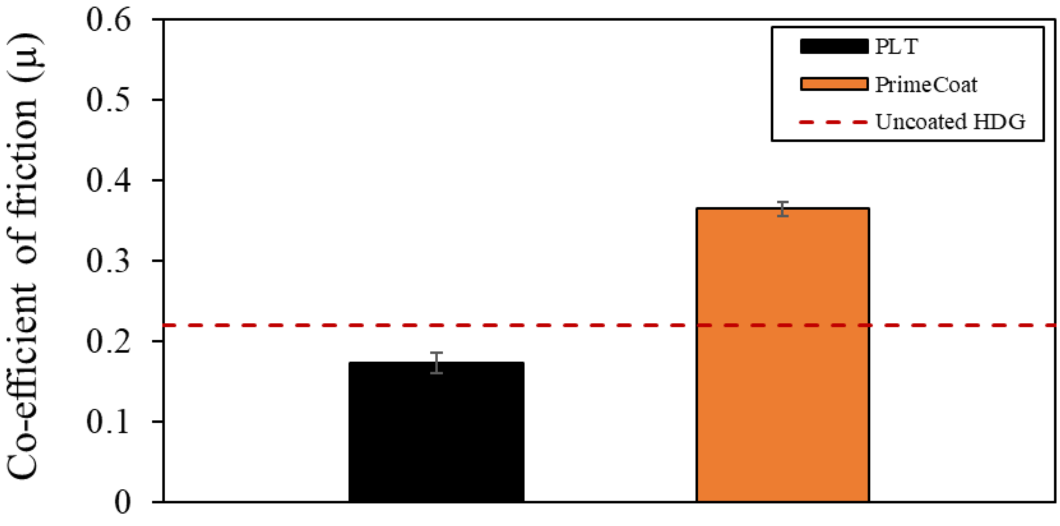

Figure 29. Mean coefficient of friction data from DFT.

Despite no additional oiling, PLT displayed a significant reduction in µ in comparison to as received and readily oiled HDG steel samples. Thus, this data infers not only that PLT can be utilised to gain greater surface lubricity, but it may be utilised without the additional oiling process, proving more economically viable and saving time throughout production. Figure 30 shows a typical profile reading recorded from DFT.

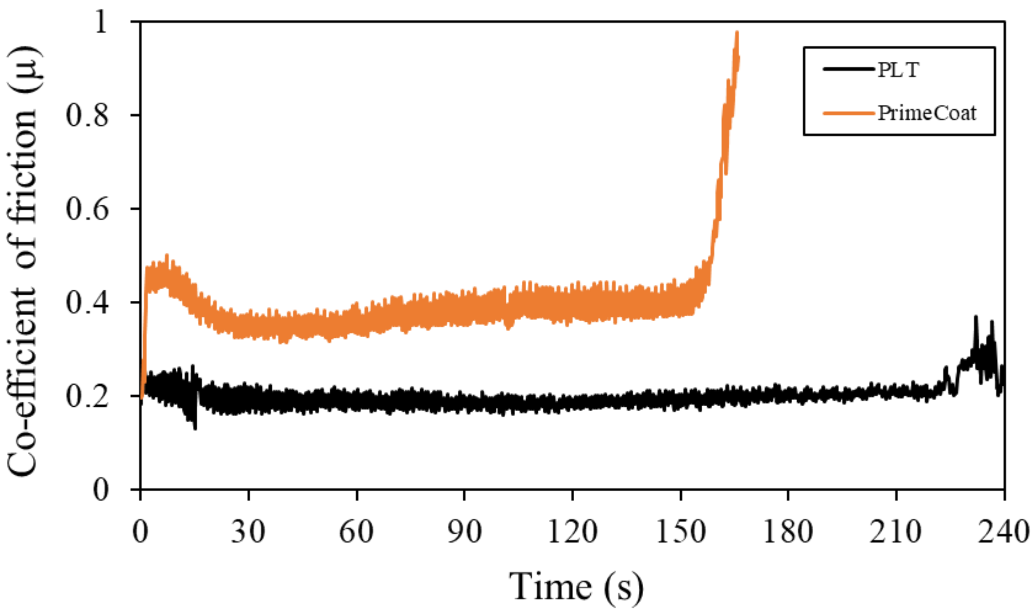

Figure 30. Example of coefficient of friction data of both PrimeCoat and PLT for 180s from DFT.

The profile for PrimeCoat and PLT differ throughout the test period. For both PrimeCoat and PLT, initial static friction is overcome and an initial bedding in period is observed at the start of the data set, before eventually plateauing to a linear value for the majority of the test duration. This plateaued period is where the data for µ was obtained to provide accurate and concurrent results. For both PLT and PrimeCoat after the plateaued period, a sharp rise in µ is observed, at approximately 160s and 120s respectively. These inflection points are hypothesised to be a result of surface degradation and wear of the coating layer, which in turn causes minute fragments of debris to interfere with the path of the pin, causing sudden spikes in µ data. Therefore, we can also associate these µ spikes with coating degradation and coating breakthrough points giving a key indicator of coating durability.

4.4 Conclusions

This chapter introduces two current coatings utilised within the industry by Tata Steel, PrimeCoat and PLT, to passivate and add a pre-lubrication layer to hot-dipped galvanised steel. Both coating chemistries have been characterised to gain a greater understanding of their behaviours as a solution and when applied to a HDG steel surface. This has included investigating surface morphology using microscopy techniques and EDS, rheological properties, surface energy, thermal stability, and enthalpy changes via simultaneous thermal analysis and also tribological behaviour via two concurrent and comparable techniques. Via this investigation, conclusions have been drawn to show the similarities and differences between the two coatings and how well they compare against each other:

- Both chemistries have very similar rheological characteristics with dynamic viscosity measuring within 0.05 mPas of each other.
- PrimeCoat displayed a higher affinity to wetting to a HDG steel surface when compared to PLT. A lower surface tension value of 30.6 mNm^{-1} was observed compared to 53.9 mNm^{-1}. Additionally, PrimeCoat displayed a faster levelling out time on the HDG steel surface as the contact angle of the coating reduced over time significantly faster than PLT.
- Both coatings demonstrated very similar thermal stability behaviour with similar drying temperatures and energy requirements. Therefore, it was hypothesised that there should be minimal issues when interchanging the coatings on an industrial line.
- Particular interest was paid towards understanding the tribological behaviour of both coatings with PLT in particular performing well as a dry film lubricant without the need for additional oiling.

The next chapter will delve further into the tribological aspect of coatings and explore further alternatives to PLT that could aid substrate performance by reducing the coefficient of friction.

5 Investigation of surface treatments to enhance surface lubricity for hot-dipped galvanised steel for increased post-production efficiency

5.1 Introduction

As discussed in Chapter 4, this chapter will delve further into the tribological aspect of coatings and explore alternative coatings that could aid substrate performance by reducing their coefficient of friction (μ). Tribological properties of a surface can be significantly improved by changing the involved materials, component design, or by employing advanced surface engineering techniques (79). Tribological properties can be altered by the application of specific coatings, potentially improving their overall performance. In turn, this can greatly improve the metal forming process by lowering tool loads, negating wear and avoiding debris pick-up during postproduction processes. (78–80,83). Reducing μ values can have varying implications on a substrate and its practical applications, especially on its performance in real-world environments. It can affect slip resistance, wear and energy efficiency, among other factors, making it a crucial variable for real-world application.

There has been gathering attention around the use of sulphate and sulphonate ions as lubricants and they have been shown to induce a strong reduction in friction and wear on substrates (143,144). As previously mentioned in Chapter 2 environmentally friendly lubricants were investigated to aid the sheet metal forming process. Showcasing an eco-friendly nature as well as independently demonstrating good lubrication potential (84). This study identified that significant friction reduction was observed when a solid lubricant within an oil matrix was used, due to reduced metal-to-metal contact, something particularly poignant for the metal sheet forming process.

More recently, a study investigated the use of ammonium sulphate treatment to improve the tribological performance of HDG steel via creating a Zn/ZnS solid lubricant matrix (85). Timma et al. found that when an ammonium zinc sulphate complex was produced on the surface in addition to a thin lubrication film, superior frictional properties were observed. Figure 12 shows the schematic of the lubrication layer, illustrating how the ZnS matrix assists in the reduction of friction by acting as a lubricating barrier between the metal to metal surface.

Lobnig et al. demonstrated ammonium zinc sulphate ($(NH_4)_2Zn(SO_4)_2{\cdot}6H_2O$) is one of the main components formed on HDG steel's surface when treated with ammonium sulphate. The chemical reaction for this is observed below (85,145):

$$ZnO + 2H_3O^+ \rightarrow Zn^{2+} + 3H_2O \quad (29)$$

$$2Zn + 8NH_4^+ + O_2 \rightarrow 2Zn(NH_3)_4^{2+} + 2H_2O + 4H^+ \quad (30)$$

$$4Zn(NH_3)_4^{2+} + 2(NH_4)_2SO_4 + 6H_2O \rightarrow (NH_4)_2Zn(SO_4)_2{\cdot}6H_2O + 6NH_3 + 2H^+ \quad (31)$$

This coating poses many significant benefits due to improving the frictional performance of the metallic surface, via a simple and effective procedure. Furthermore, there is minimal negative impact on users and the environment, due to the coating's low toxicity and simple chemistry. Thus, there is particular interest in exploring the use of a ZnS matrix and whether certain parameters can further improve its performance.

Magnesium addition within alloys has attracted lots of recent interest due to research revealing its greater corrosion resistance, improved frictional performance and improved galling behaviour in comparison to conventional hot-dipped zinc coatings (146–148). Therefore, it is of significant interest to understand how these sulphate coatings may interact with differing compositions, that are used in industry. The principle aims of this research chapter are to conduct a systematic study that:

- Investigates the tribological properties of HDG substrates with different alloying additions before and after coating via a dynamic testing method.
- Investigates how altering the pH of an ammonium sulphate coating formulation could affect the overall frictional performance of three different zinc-coated substrates.
- Investigates whether changing the solute used within the coating formulation has an overall effect on the frictional performance of three different zinc-coated substrates.

5.2 Materials and methods

5.2.1 Materials

Throughout this chapter, three different substrate grades were analysed to assess their frictional performance before and after coating. Standard HDG steel was investigated in addition to two compositions with an Mg-Al addition, ZM70 and ZM170. All substrate grades were produced by TATA Steel (Port Talbot, Wales) and were cut into 50 × 50 mm samples for the systematic study. Table 6 demonstrates the metallic coating specification and percentage weight of alloying additions for all substrates used throughout the systematic study.

Table 6. Coating parameters and percentage alloying additions for substrates.

Grade	**Coating Specification**		**Mg**		**Al**	
	Weight (gm^{-2})	**Thickness (µm)**	**Min.**	**Max.**	**Min.**	**Max.**
HDG	275	20	-	-	1.4	1.8
ZM70	70	5	1.4	1.8	1.4	1.8
ZM170	170	13	1.4	1.8	1.4	1.8

Standard HDG steel samples were 0.86 mm gauge and had a target coating weight of 275gm^{-2} (~20µm thickness on each side) comprising approximately 0.15% aluminium. Both Zn-Al-Mg alloys had the same target Mg-Al addition. What distinguishes the two, is the coating weight and thickness. ZM70 had a target coating weight of 70gm^{-2} (~5µm thickness each side) in comparison to ZM170 which had a target coating weight of 170gm^{-2} (~13µm thickness each side).

In addition to investigating three different zinc-coated substrates, three sulphate treatments were formulated to investigate the change in solutes' effect upon frictional performance. The three chemicals utilised for the solute were ammonium sulphate ($(NH_4)_2SO_4$), sodium sulphate (Na_2SO_4) and magnesium sulphate ($MgSO_4$). Na_2SO_4 was investigated alongside $(NH_4)_2SO_4$ because it is easily available and a cheaper alternative. Additionally, there was particular interest in investigating the use of $MgSO_4$ to see if this interacted differently with the Mg content within Mg-Zn coated alloys. 45g of ammonium sulphate was diluted and magnetically stirred in 0.5L of de-ionized water, giving a molarity of 0.68. This process was repeated with 48.5g of sodium sulphate and 41g of magnesium sulphate respectively to make three separate coating formulations. All chemicals were purchased from Sigma Aldrich (St. Louis, MO, USA) and were of reagent grade. The oil used throughout this systematic study was FERROCOAT 6130 (Quaker Chemical B.V) (Uithoorn, The Netherlands) as used by Tata Steel in production. This oil was used consistently throughout the study in order to keep results concurrent and accurate.

5.2.2 Methods

5.2.2.1 Sample Manufacturing

All substrate samples were cleaned thoroughly to mimic the industrial cleaning process (118). After drying was completed, coated samples were then additionally oiled via the same spin-coating method. Unless otherwise stated, 0.5 ml of oil was deposited into the centre of the coupon and spin-coated again at 5000 RPM for 30 s, to provide a second uniform layer.

5.2.2.2 Characterisation techniques

Surface morphology and analysis of the substrate surface was visualised using scanning electron microscopy (SEM) (Hitachi TM3000) (Tokyo, Japan) equipped with electron dispersive spectroscopy (EDS) as well as using digital microscopy (Keyence VHX-7000) (Osaka, Japan). Dynamic friction testing (DFT) was conducted via a novel Pin-on-Disk (POD) tribometer as described in Chapter 4. The dynamic friction method utilised a loaded pin and rotating sample stage and was designed, commissioned, and built in reference to ASTM G99-17. All samples were analysed at room temperature (~20°C).

5.3 Results and discussion

5.3.1 Surface morphology

SEM was used to visualise the sulphate coating on the HDG steel surface. Figure 31 shows a topographical image of the ammonium sulphate coating treated on HDG steel using 5kv accelerating voltage, a working distance of 9.8mm.

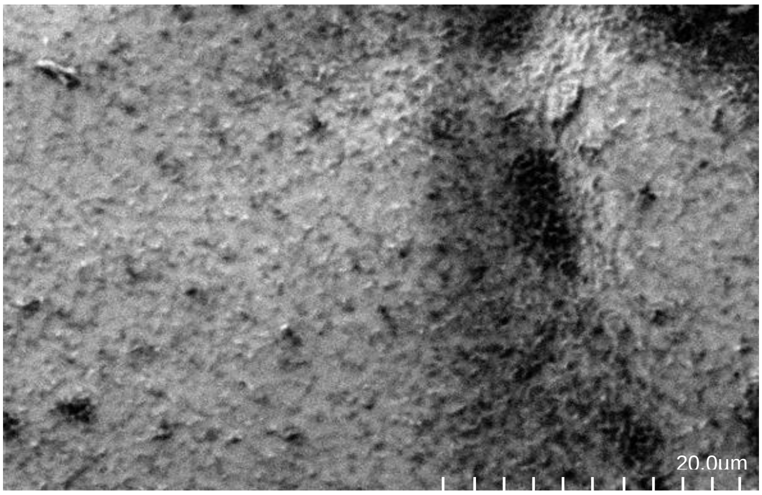

Figure 31. SEM imaging of ammonium sulphate coating on HDG steel surface at × 2500 magnification.

There are small globular particles identified on the surface of the substrate. These globular particles are recognised as the matrix of $(NH_4)_2Zn(SO_4)_2\cdot 6H_2O$ and $ZnSO_4$ on the surface. This hypothesis is reinforced by accompanying EDX images, showing maps of element S distributed over the substrate surface. Figure 32 demonstrates the corresponding EDX analysis completed of the ammonium sulphate treated HDG steel substrate, including the full layered EDX map and the element map of element S. EDX was unable to effectively work at the lower accelerating voltage of 5kV. Therefore, for analysis, secondary images were taken of the substrate using 15kV accelerating voltage in analytical mode at 100 µm scale.

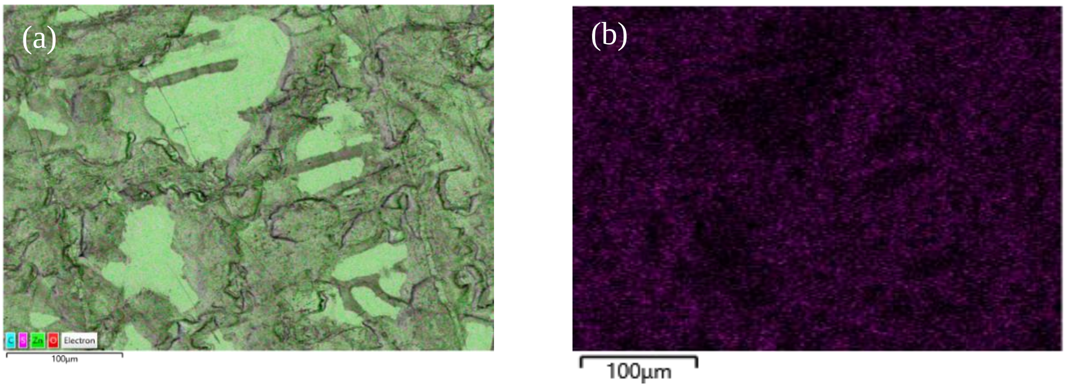

Figure 32. EDX images of ammonium sulphate coating on HDG steel, showing: (a) layered map and (b) element map of S.

5.3.2 Dynamic friction testing

5.3.2.1 Oiling replication investigation

Before analysing the effect of the sulphate coatings, it was crucial to understand and ensure a repeatable and homogeneous oil layer could be achieved within laboratory settings, mimicking that of industrial standards. An oiling replication study was carried out to identify what oil volume and parameters were needed for accurate replication of the as-received samples from Tata Steel.

Initially, all coupons were degreased with ethanol, before submerging in 1M sodium hydroxide solution for 15s at 50 °C. Incremental volumes of oil were spin-coated on to HDG steel substrate and then analysed via visual inspection and DFT. Table 7 displays μ data and whether the oil layer was sufficient across the substrate surface, for differing volumes of oil.

Table 7. Mean coefficient of friction data recorded for oil volume range used on HDG steel. .

Volume (ml)	**Cleaned**	**Mean μ**	**Coating layer homogeneity**
As received	✗	0.19	complete
0	✓	0.87	-
0.25	✓	0.19	incomplete
0.5	✓	0.18	complete
0.75	✓	0.17	complete
1	✓	0.16	complete
2	✓	0.16	complete

The as-received sample demonstrated a completely homogeneous oil layer across its surface and delivered a mean μ value of 0.19. After the HDG steel's surface was thoroughly cleaned and no additional oil was applied, the mean μ value dramatically increased to 0.87. This large increase reinforces why lubrication is necessary for post-production processes. The large increase in μ can be accredited to the removal of surface lubrication and the removal of ZnO and Al_2O_3 at the surface-to-pin interface, increasing overall surface roughness. Surface roughness has been shown to largely affect the coefficient of friction of a substrate, with rougher surfaces imparting higher μ values (149–151). Lee et al. established an empirical relationship between surface roughness, λ and μ, in order to show their relationship with eachother (150):

$$\mu = 0.24\lambda^2 - 0.346\lambda + 0.252 \tag{32}$$

0.25ml of oil was shown to deliver a mean coefficient of friction value of 0.19, the same as was recorded for the as-received sample. However, upon visual inspection, it was clear that the oil coating layer was not complete across the sample surface and thus could not be used as an accurate replication of as-received samples. 0.5ml of oil was observed to give the closest replication to as received coated samples. Figure 33 demonstrates a typical dynamic friction test run of a 0.5ml oiled sample.

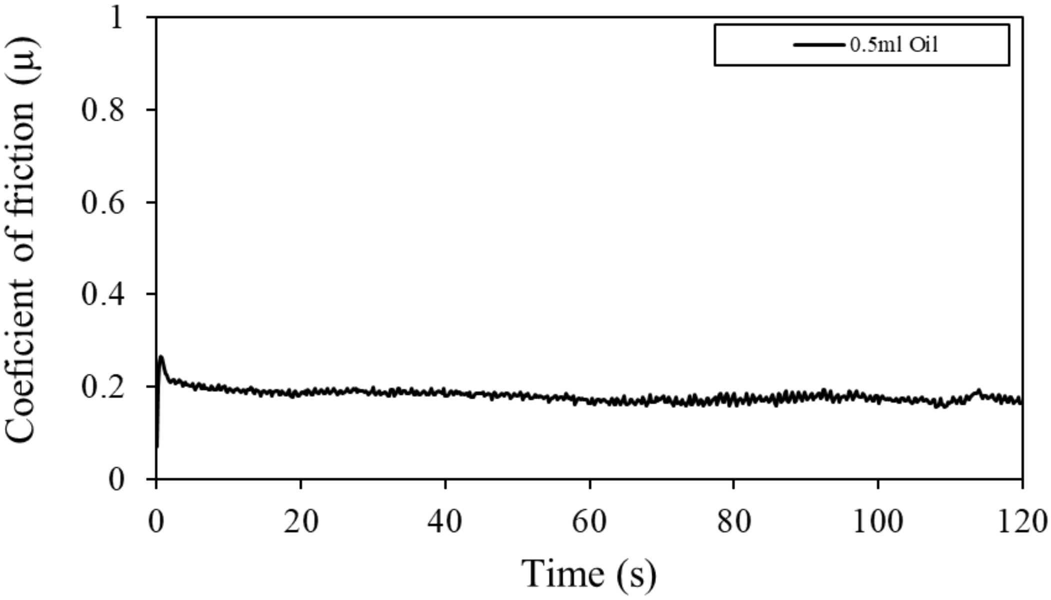

Figure 33. Coefficient of friction data recorded over 120 s for a 0.5ml oiled sample.

A mean µ value of 0.18 was recorded within 0.01 from the target value. In addition 0.5ml of oil allowed for a completely homogeneous coating layer across the sample surface. Throughout the rest of the study, all larger increments of oil volume demonstrated homogeneous layers across the surface after spin coating, however coefficient of friction values recorded continued to decrease, meaning they did not accurately replicate the as-received sample.

5.3.2.1.1 Wear track analysis

Due to the nature of the dynamic friction tests, the sample's surface becomes degraded through the friction experienced once the 2N force is repeatedly applied. A wear track is observed which shows the heavy deformation experienced by the sample after 120 s of testing. Table 8 shows the data recorded from the inspection of the wear track via digital microscopy.

Table 8. Wear track analysis data for as received standard HDG and after oiling with 0.5 ml.

Sample	**Mean width (μm)**	**Standard error (μm)**	**Mean depth (μm)**	**Standard error (μm)**
As received	200	± 2	12	± 0.3
0.5 ml oiled	189	± 2	10	± 0.4

Figure 34 and Figure 35 respectively showcase profiles of the wear track dimensions for an as-received standard HDG steel sample that has undergone 120 s of dynamic friction testing. The width and depth of the wear track identify how much deformation has occurred. The deeper the track the more surface contact there is with the pin and thus the wider the track will also be. The depth of the track is an important factor to analyse as it gives a quantitative idea of how much zinc coating is abraded and compressed or removed through the continuous frictional force applied via DFT.

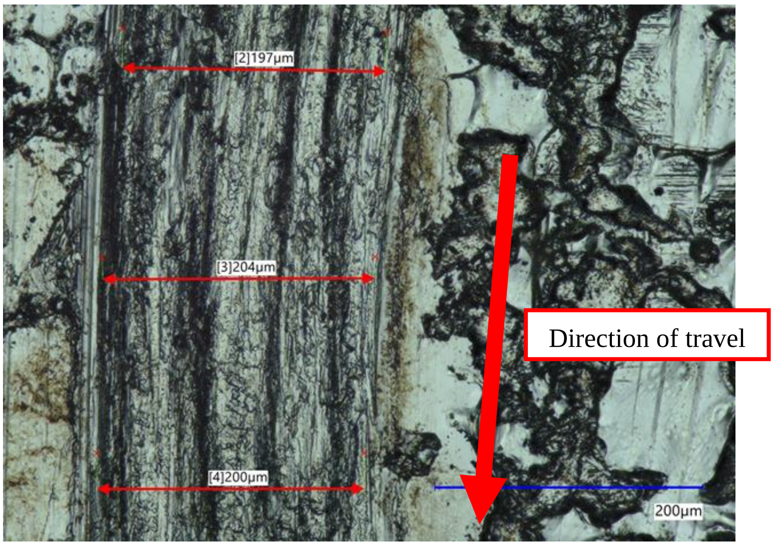

Figure 34. Image of wear track analysis for as received standard HDG steel after 120 s.

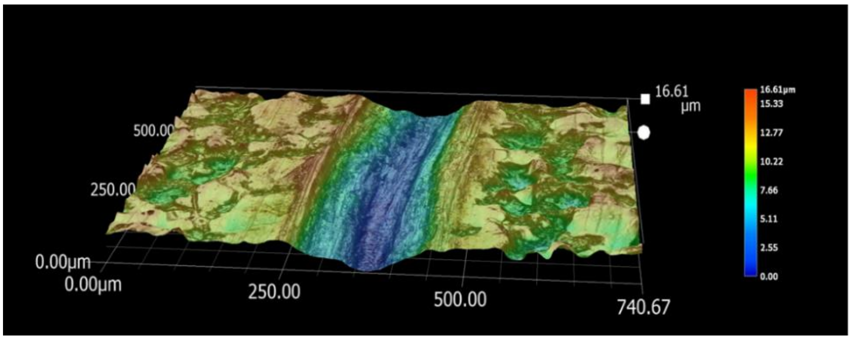

Figure 35. 3D profiling via digital microscopy for wear track analysis for as received standard HDG steel after 120 s.

Table 8 demonstrates that the mean width and depth dimensions of both substrates' wear tracks are similar. The 0.5ml oiled sample demonstrates slightly less deformation, with the wear track experiencing slightly reduced width and depth dimensions in comparison to the as-received sample. This data corroborates previously measured µ values that were recorded. The 0.5ml oiled sample delivered a mean µ value of 0.18 in comparison to the value of 0.19 from the as-received sample and thus lends itself to have slightly better frictional performance. Nonetheless, it was concluded that the similarity in µ values and wear deformation aligned close enough to the as-received sample to showcase similar behaviour under testing conditions. Therefore, it was decided throughout the systematic study to utilise 0.5ml of oil on each sample thereafter to recreate as close to industrial conditions as possible.

5.3.2.2 Substrate comparison

Standard HDG steel, ZM70 and ZM170 were the three different substrates analysed throughout the chapter. Firstly, it was key to understand each substrate's frictional performance before and after coating and thus a study was conducted to compare each substrate in its as-received state. Figure 36 demonstrates this for each substrate investigated. All samples were investigated over a period of 120 s unless intervention due to failure was necessary.

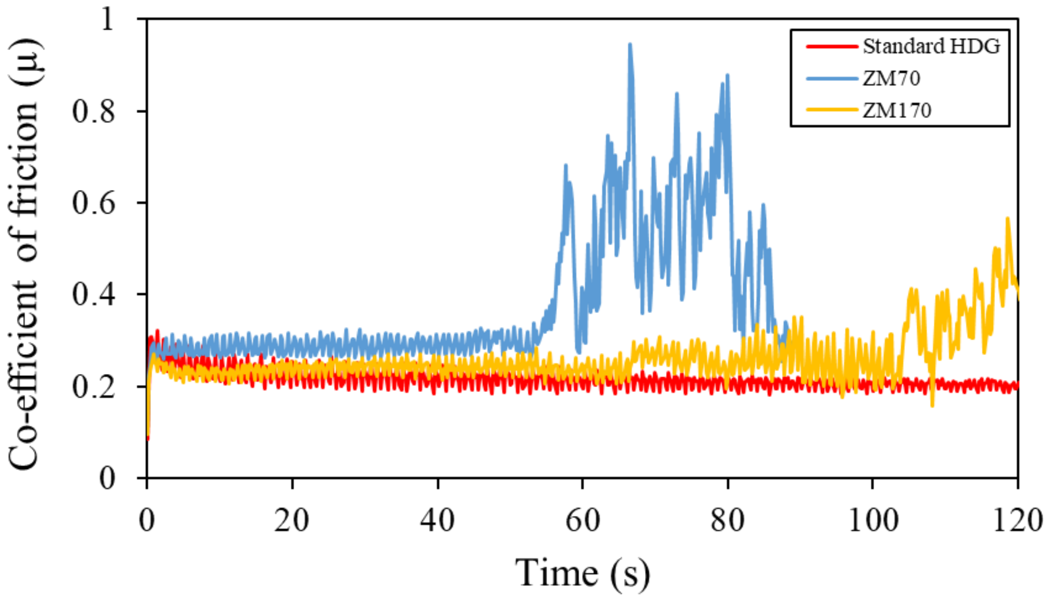

Figure 36. Coefficient of friction graphs comparing as received samples of standard HDG steel, ZM70 and ZM170.

Standard HDG steel displays constant frictional behaviour after overcoming initial static friction at the beginning of the investigation. The substrate performed the best over time with very limited fluctuation of µ value. This enabled the coefficient of friction value to be easily calculated and taken over the duration of the test (120s). Standard HDG steel delivered a mean µ value of 0.19.

The frictional behaviour of ZM70 was very different from that of its counterparts. Like standard HDG steel, initial static friction was overcome at the start of the test. After this, force measurements remained constant until at approximately 50s the test experienced drastic fluctuations in force recorded, returning unusually high µ values. This can be attributed to the high frictional forces experienced in breaking down the galvanised coating during testing. In turn, debris built up within the wear track radius and obstructed the path of the pin. This obstruction was detrimental and caused an increase in frictional force measurements through increased surface roughness. The test was run for a further 40s before being prematurely stopped due to the coating failure. The mean µ value was recorded up until the coating failure at 50 s. ZM70 delivered a mean µ value of 0.29.

Upon analysis of the ZM170 substrate, it performed somewhere in between that of standard HDG steel and ZM70. There was a longer, more consistent constant region when compared to ZM70. This was observed after overcoming initial static friction and bedding in period until approximately 100s. At this point, coating failure occurred. This was due to suspected breakthrough to the underlying substrate and increased surface debris from surface degradation causing large fluctuations in frictional forces recorded, as was observed with the ZM70 substrate. Up until this point, ZM170 delivered a mean μ value of 0.25. Table 9 displays the coefficient of friction data for each substrate in its as-received state.

Table 9. Coefficient of friction data for each substrate investigated.

Sample	**Coefficient of friction (μ)**	**Standard error**	**Failure time (s)**
Standard HDG Steel	0.19	0.01	> 120
ZM70	0.29	0.01	50
ZM170	0.25	0.01	100

5.3.3 pH investigation

Timma et al. demonstrated the increased frictional performance of a galvanised substrate by utilising a simple, ammonium sulphate coating with an additional lubrication layer to create a ZnS/S matrix on the surface (85). The study investigated a range of ammonium sulphate concentrations within the solution but did not consider the potential effect pH may have on the coating's performance. The pH of a formulation can play a significant role in how the coating behaves. By increasing the amount of free OH^- ions within the solution, you subsequently increase the pH of the solution. A reverse of this is seen when more H^+ ions are present, and the pH is reduced. Referring to equation (3), we can observe that H^+ ions are present in the solution and hence why the pH of the sulphate coating formulation is slightly acidic at 5.3. Given Le Chatelier's principle, by adding additional H^+ ions in solution, dropping the pH level could drive equations (2) and (3) towards the left, reducing the amount of ammonium zinc sulphate formed at the steel interface. Therefore, there is significant interest in analysing the effect of changing pH balance has on the coating's performance. As well as this, pH levels can affect the metallic coating corrosion products, as uneven coverage of the oxides can be created, negatively impacting corrosion rates of the substrate (152). Additionally, the pH influences the overall environmental impact a treatment may have, especially for end-of-life applications. Highly acidic/alkaline residues can have locally severe and long-lasting effects on some environments, posing as a threat to both terrestrial and aquatic ecosystems (153). There could be significant impact if neutralised chemicals can be used, reducing overall risk for users and the wider environment.

Therefore, a systematic study was conducted to assess the effect changing pH had on the coating adherence and performance for a sulphate-based coating on zinc-coated steel. Throughout the study, ammonium sulphate solution was utilised, and a range of pH levels were investigated incrementally from 3 – 11, in increments of 2. pH levels were measured using a pH colour strip as well as a pH meter to ensure concurrent results. At 0.68M, the ammonium sulphate solution was slightly acidic and gave a pH reading of 5. To reduce the pH of the solution 1M hydrochloric acid was dropwise added during magnetic stirring until a pH of 3 was reached. To increase the alkalinity of the solution, 1M of NaOH (aq) was dropwise added during magnetic stirring. Each formulation was individually coated onto the three different substrates to assess their performance. DFT was completed, immediately after coating and curing, this time frame was standardised for each sample set.

Figure 37 demonstrates the mean coefficient of friction data recorded for standard HDG steel samples when treated with ammonium sulphate over a ranging pH scale. As to be expected from the literature, the coated substrate shows a better frictional performance than its just oiled counterpart with reduced μ values.

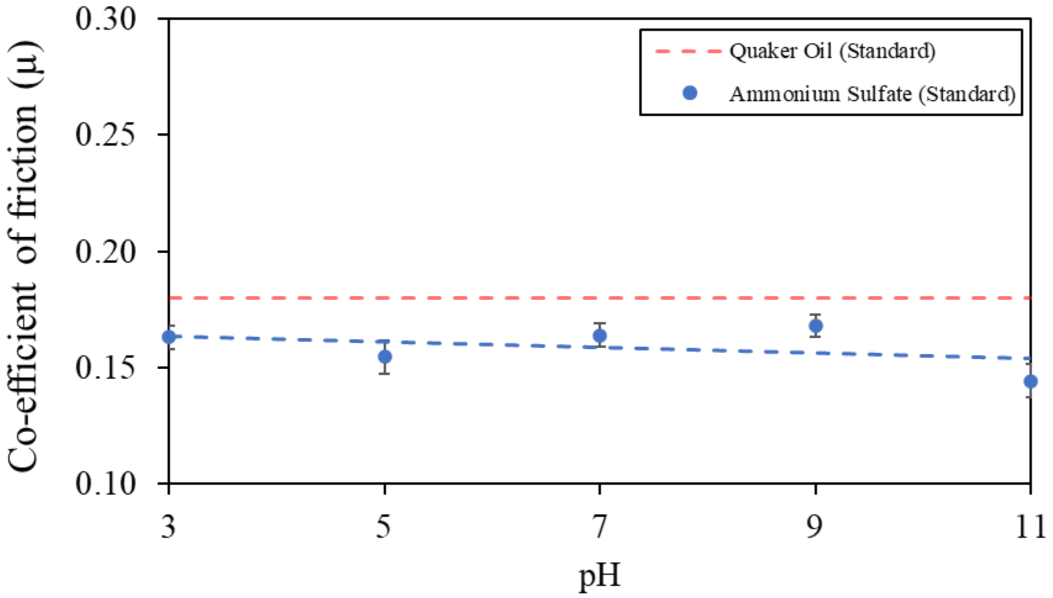

Figure 37. Graph displaying the effect changing pH of ammonium sulphate formulation and has upon the coefficient of friction on standard HDG steel.

The oiled substrate delivered a mean µ value of 0.18. In comparison, the coefficient of friction was reduced by approximately 15% with the ammonium sulphate treatment across the whole pH range. A pH of 5 delivered a mean µ value of 0.15 whereas, when the alkalinity was increased, and the pH raised to 11, a mean µ value of 0.14 was recorded. However, during the overall assessment, the mean µ values remained reasonably linear as depicted by the trendline. This suggests that the frictional performance of a standard HDG steel substrate is independent of pH when applying the ammonium sulphate formulation. This independence can be viewed positively, it suggests despite the pH of the solution, significant improvements can be achieved. Thus, within industry a more neutral solution may be utilised, reducing potential negative environmental effects. The same study was conducted on the ZM70 substrate and can be seen in Figure 38.

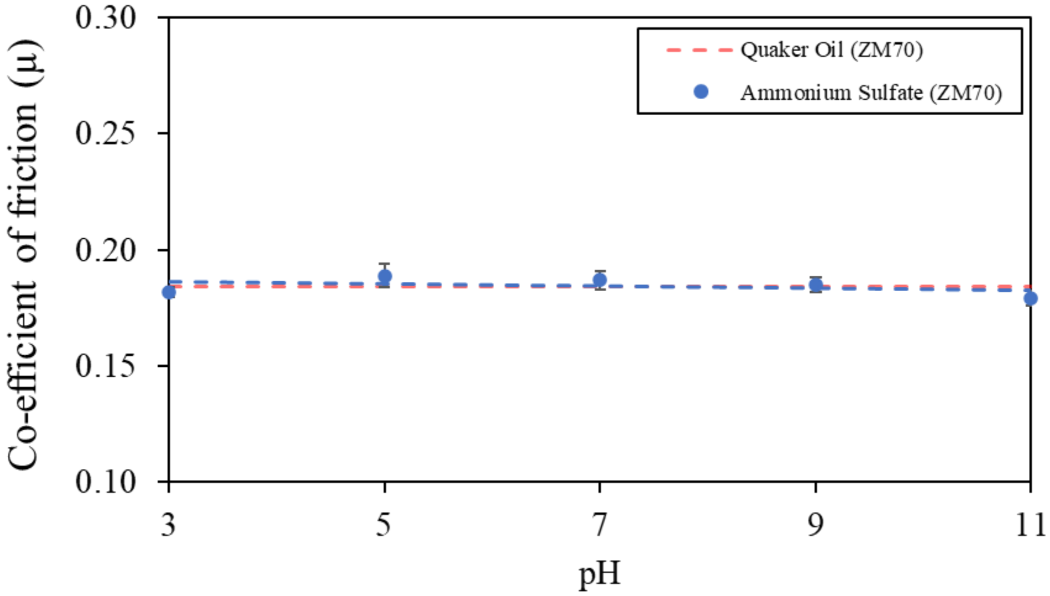

Figure 38. Graph displaying the effect changing pH of ammonium sulphate formulation and has upon the coefficient of friction on ZM70.

The ZM70 substrate showed no frictional improvement with the addition of the ammonium sulphate treatment. This was observed across the whole pH range, where there was no obvious change in mean µ values from pH 3 through to 11. The mean µ value for oiled samples and treated samples were both recorded at 0.18. It was hypothesised that the ammonium sulphate treatment did not efficiently coat the surface and fabricate enough ammonium zinc sulphate to affect the frictional performance of the ZM70 substrate. Due to the reduced metallic coating weight and thickness of ZM70, there is limited opportunity for $(NH_4)_2Zn(SO_4)_2{\cdot}6H_2O$ and $ZnSO_4$ molecules to propagate. Thicker metallic coatings are more abundant in Zn and ZnO at the substrate surface, meaning there is a greater opportunity for Zn^{2+} ions to be present at the coating interface and aid the formation of molecules within the lubrication coating matrix. Thus if $(NH_4)_2Zn(SO_4)_2{\cdot}6H_2O$ is insufficient the substrate's frictional performance will not be enhanced. The frictional performance of the ZM170 substrate throughout the pH study can be observed in Figure 39.

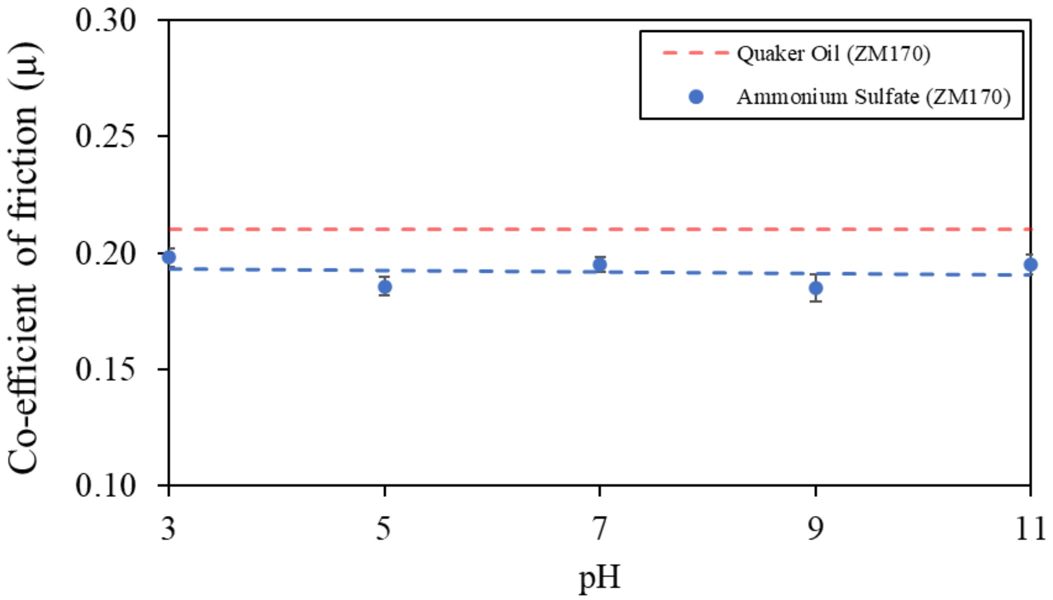

Figure 39. Graph displaying the effect changing pH of ammonium sulphate formulation and has upon the coefficient of friction on ZM170.

With the addition of the ammonium sulphate treatment, ZM170 sees an improvement in frictional performance. The oiled substrate delivered a mean µ value of 0.21. In comparison, the coefficient of friction was reduced by approximately 10% across the whole pH range when the ammonium sulphate treatment was applied. Throughout the overall assessment, although the improvement in frictional performance was not as high as seen with standard HDG steel, the coefficient of friction was notably reduced. Similarly, to standard HDG steel, the mean µ values and trendline depict a linear relationship, suggesting no change in performance with changing pH range. This suggests that the frictional performance of the ZM170 substrate is also independent of pH when applying the ammonium sulphate formulation. It is again hypothesised that the reduced lubrication capacity in comparison to standard HDG steel is linked to the coating weight and thickness of the metallic coating, as previously discussed with the ZM70 substrate. Another factor that could play an influential role in the ability for the lubrication matrix to aid the coefficient of friction is the surface roughness of the substrate.

5.3.4 Solute investigation

The use of ammonium sulphate has proved very effective in reducing the coefficient of friction of HDG steel and improving its frictional performance during dynamic testing both throughout this study and by Timma et al. (85). Given ammonium sulphates' performance, there is significant interest in investigating if other solutes may interact with a metallic-coating similarly and produce as good, if not better results. Sodium sulphate and magnesium sulphate were utilised within two other coating formulations and assessed via the same dynamic friction test. Sodium sulphate is neutral on the pH scale and thus makes it particularly interesting from an environmental standpoint. If a neutral solute can be utilised it can reduce end-of-life complications around cleaning and disposal. Magnesium sulphate is of particular interest due to the substrates ZM70 and ZM170 being analysed. Both have additions of Mg within the alloying matrix and thus it is of particular interest to see if this interaction will affect the coating production and results. The results comparison for the different coating formulations on the substrates can be seen in Figure 40.

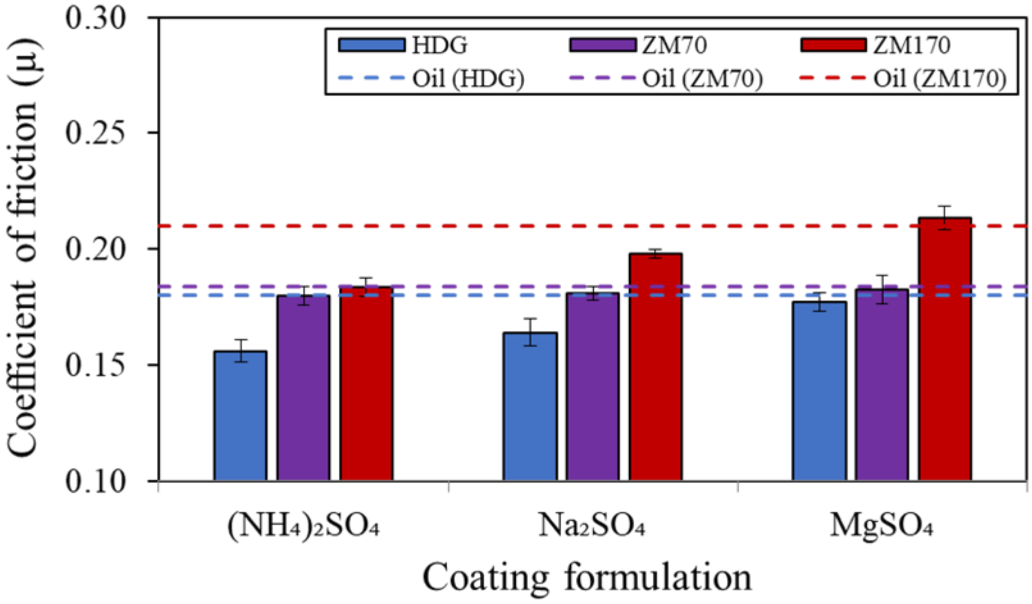

Figure 40. Chart displaying the effect that change in solute has upon the coefficient of friction for all three substrate grades.

The data presented shows ammonium sulphate to be the best-performing coating formulation when applied to standard HDG steel. The mean µ value for ammonium sulphate formulation is approximately 0.15, in comparison to sodium sulphate at 0.16 and magnesium sulphate at 0.18, the same as an uncoated oiled sample. When the ZM70 substrate was studied, despite the change in solute there was no frictional improvement observed for any of the substrates. Ammonium sulphate, sodium sulphate and magnesium sulphate all demonstrated a mean µ value of 0.18, the same as an uncoated oiled ZM70 substrate. This suggests inefficient coating has occurred, despite the solute used. As previously discussed, this may be linked to limited free Zn^{2+} cations from oxidation of the surface due to reduced metallic-coating weight.

Additionally, reduced metallic-coating weight will affect the coated surface's microstructure and properties. The reduced coating weight and introduction of magnesium will cause the microstructure to have a varying range of zinc dendrites with less complex binary/ternary eutectic phases, which has been shown to effect corrosion resistance (154,155). Changes in microstructure and coating thickness can also play an influential role in the substrate's overall surface roughness, with reduced coating weights generally showing higher surface roughness, ultimately contributing to reduced frictional performance (156,157). ZM170 substrate showed similar trends in behaviour to standard HDG steel. Ammonium sulphate formulation produced a mean µ value of approximately 0.18, in comparison to sodium sulphate at 0.19 and magnesium sulphate at 0.21, the same as an uncoated, oiled ZM170 sample. Here we observe different behaviour to the ZM70 substrate hypothesised because of the link between heavier metallic-coating weights and surface roughness.

It is apparent across all substrates that magnesium sulphate yields the worst results and sodium sulphate sees some improvements in frictional behaviour. However, ammonium sulphate is shown to enhance the surface lubricity by the greatest margin.

It is important to note at 25°C, ammonium sulphate has a relative solubility of 76.4g/100g in water. Comparatively, sodium sulphate and magnesium sulphate have relative solubility of 28.1g/100g and 35.7g/100g in water, respectively. Present cations within the solution can affect the formation of the coating product. NH_4^+ cations have a greater influence in comparison to Na^{2+} and Mg^{2+} and thus there is a favourable proportion of $(NH_4)_2Zn(SO_4)_2 \cdot 6H_2O$ and $ZnSO_4$ molecules formed when ammonium sulphate is utilised (158). When Na_2SO_4 and $MgSO_4$ are the solutes, the main product formed due to the displacement reaction is $ZnSO_4$ alone. Ammonium zinc sulphate aids the frictional performance of the coating and thus explains why ammonium sulphate may perform better than its counterparts in enhancing surface lubricity. It can be noted that the use of both ammonium and sodium sulphate treatments may enable a reduction in oil volume to be used on the substrate for enhanced lubricity, in turn reducing excess material needed and reducing overall costs.

5.4 Conclusion

This chapter studied the tribological aspect of coatings and introduced the use of sulphate-based treatments to aid substrate performance by reducing the coefficient of friction. Three different zinc-coated substrates with different alloying additions and characteristics were investigated for their frictional performance with and without a functional coating. A systematic study was conducted to analyse whether changing the pH of the ammonium sulphate formulation and whether changing the solute type had an effect on the coefficient of friction. Throughout these studies, surface microscopy techniques and novel dynamic friction tests have been completed to draw key conclusions.

Standard HDG steel, ZM70 and ZM170 substrates were analysed in their as-received state to identify frictional characteristics before coating. μ values were recorded at 0.19, 0.29 and 0.25 respectively.

The pH of ammonium sulphate treatment was altered incrementally from 3 – 11 before being coated onto three different substrates. For standard HDG steel and ZM170, ammonium sulphate treatment was seen to enhance surface lubricity by 15% and 10% respectively across the range of pH values. It was concluded that improvement in the coefficient of friction is independent of the pH of the ammonium sulphate treatment. Thus, within industry a more neutral solution may be utilised, reducing potential negative environmental effects. For the ZM70 substrate, no frictional improvement was observed. It was hypothesised that coating thickness and as a result surface roughness played a major role in coating efficiency.

Sodium sulphate and magnesium sulphate were introduced as alternative solutes and compared with ammonium sulphate. Despite the solute used, the ZM70 substrate failed to see any improvement in frictional performance. Ammonium sulphate and sodium sulphate treatment were both seen to improve the frictional performance of the remaining substrates, however, magnesium sulphate had negligible effect. Ammonium sulphate was shown to improve surface lubricity by the greatest margin due to the influence of cations present. The use of both ammonium and sodium sulphate treatments may enable a reduction in oil volume to be used to reduce material needed and overall costs.

The use of sulphate-based treatments as functional coatings has been shown to improve the frictional performance of HDG steel. The next chapter of work will further investigate the use of alternative functional coatings that can be applied to zinc-coated steel to add value to the end product.

6 The investigation of novel hydrophobic coatings for hot-dipped galvanised steel

6.1 Introduction

This chapter will further investigate alternative functional coatings that can be applied to zinc-coated steel to add value to the overall product. There has been growing interest in the use of hydrophobic coatings (HCs) to improve the corrosion resistance of metallic substrates and to provide functionality, such as self-cleaning (86,97–101). These coatings are inspired by the natural surface of lotus leaves, which have nano-structured surfaces coated with low-surface-energy materials that provide an interface between the coating and liquid (102). The interface is created by retaining air within the nano-scale topography of the surface, which reduces the contact area of water droplets, producing a highly non-wetting, low-adherence surface (100,101,104). A superhydrophobic surface (SHS) refers to a surface with a contact angle of more than 150° (86–88). SHSs have been shown to provide effective corrosion protection on a range of metallic substrates, such as steel (89,90), copper (91), magnesium (92) and zinc (93–97).

The preparation of superhydrophobic coatings on metallic substrates can be achieved using a variety of methods, such as electrodeposition, chemical etching and hydrothermal growth (101,105–108). However, many of these methodologies require complex two-step processes that would be difficult to implement in an industrial application. Due to these issues, there have been recent advances to develop simple one-step methods to produce a superhydrophobic surface. Li et al. implemented a one-step immersion method to produce a superhydrophobic coating on zinc using a solution of stearic acid containing silver nitrate (109).

The coating was applied at room temperature within 1 min, and the reported results indicated excellent corrosion protection; however, the use of silver nitrate would be prohibitive for industrial applications due to cost. Chen et al. used a rapid one-step electrodeposition process to produce a superhydrophobic coating on copper using a nickel chloride-based electrolyte solution. The resulting surface was reported to achieve up to a 164° contact angle and less than a 2° rolling angle; however, the corrosion resistance was not reported (110).

Liang et al. produced a superhydrophobic coating on a zinc surface implementing a simple one-step hydrothermal growth technique using stearic acid and silicon dioxide (SiO_2) particles (88). The authors reported excellent corrosion performance when the coating was immersed in an aqueous sodium chloride solution and contact angle measurements were recorded of up to 160°. The zinc layer on the surface of hot-dipped galvanized (HDG) steel reacted with stearic acid to form low surface energy zinc stearate. The chemical reaction for this is observed below (88):

$$\mathrm{Zn} - 2\mathrm{e}^- = \mathrm{Zn}^{2+} \tag{33}$$

$$\mathrm{Zn}^{2+} + 2\ \mathrm{CH_3(CH_3)_{16}COOH} = \mathrm{Zn[CH_3(CH_2)_{16}COO]_2} + 2\ \mathrm{H}^+ \tag{34}$$

However, the coating required up to 6 h to form, which would be impractical for industrial applications. The methodology described by Liang et al. provides a foundation for further improvements to reduce the time required to produce a suitable coating, thereby, making the coating more appropriate for industrial applications (88). Therefore, the principal aims of this research chapter were to conduct a systematic study that:

- Produced a simple one-step hydrophobic coating on a HDG steel substrate.
- Used a variety of analytical techniques to evaluate the coating’s effectiveness and corroborate previous literature findings.

- Investigated a range of formulations and processing windows to improve the coating’s performance and identify whether it can be made more industrially appropriate.
- Investigated the use of a higher boiling point solvent to assess whether changing solution temperature affected hydrothermal growth of zinc stearate creation rate.

6.2 Materials and Methods

6.2.1 Materials

Sodium hydroxide, hydrogen peroxide (30%), stearic acid and silicon dioxide (9–20 nm) were purchased from Sigma Aldrich (St. Louis, MO, USA). Ethanol, IPA and L-butanol were all purchased from Fisher Scientific (Hampton, VA, USA). Fumed silicon dioxide (Aerosil 300, Essen, Germany, 0.2–0.3 µm) was obtained from Evonik. All chemicals used were of reagent grade. Hot-dipped galvanized (HDG) steel was provided by Tata Steel UK (Llanwern, Wales) and cut into 10 × 10 mm samples for the initial systematic study.

6.2.2 Methods

6.2.2.1 Coating Production

A one-step immersion method was used to coat HDG steel samples. First, the HDG samples were prepared by degreasing using ethanol. They were then submerged in 1 M sodium hydroxide solution for 15 s at 50 °C, which replicates the industrial cleaning process (118). The coating formulation used either ethanol or isopropyl alcohol (IPA) as the solvent, which is given in Table 10. The formulation was prepared by adding 0.05 M stearic acid to 100 mL of the relevant solvent.

Hydrogen peroxide (2 mL) was added dropwise to the formulation whilst magnetically stirred for 1 min. Silicon dioxide (1% wt.) was added to the formulation and magnetically stirred for 30 min to ensure the stearic acid was fully dissolved and the silicon dioxide was evenly dispersed. The particle size of silicon dioxide was a variable investigated, which can be seen in Table 10. The formulation was heated and held at 70 °C using a hotplate before HDG samples were immersed for up to 360 min. The samples were then removed, rinsed with ethanol and blown dry.

Table 10. Formulations used to produce hydrophobic coatings.

Formulation	**Solvent**	**Molarity of Stearic Acid (M)**	**SiO_2 Size (nm)**	**NaOH Addition**
1	Ethanol	0.05	200–300	✗
2	IPA	0.05	200–300	✗
3	Ethanol	0.05	200–300	✓
4	Ethanol	0.1	200–300	✗
5	Ethanol	0.2	200–300	✗
6	IPA	0.05	200–300	✓
7	IPA	0.1	200–300	✓
8	IPA	0.2	200–300	✓
9	Ethanol	0.05	9–20	✓
10	Ethanol	0.1	9–20	✓
11	Ethanol	0.2	9–20	✓
12	IPA	0.05	9–20	✓
13	IPA	0.1	9–20	✓
14	IPA	0.2	9–20	✓

6.2.2.2 Characterization Techniques

Surface morphology and analysis of the hydrophobic surface was visualised using scanning electron microscopy (SEM) (Hitachi TM3000) (Tokyo, Japan) equipped with electron dispersive spectroscopy (EDS). The wettability of the surface was determined by analysing the contact angle (CA) (FTA1000 manual system, First Ten Angstroms) (Portsmouth, VA, USA) of de-ionised water in contact with the coating film. CA measurements were recorded with an error measure of ±1° under optimized illumination and optical conditions.

Fourier-transform infrared spectroscopy (FTIR) (PerkinElmer spectrum-100) (Waltham, MA, USA) was used to characterise the surface chemical constituents. Atomic force microscopy (AFM) (JPK nanowizard 3) (Berlin, Germany) was used to measure the topography of the substrate surface.

6.2.2.3 Initial Studies

An initial study investigated the feasibility of reducing the time required to produce a hydrophobic coating using the experimental procedure published by Liang et al. (88). Samples of HDG steel were immersed in formulation 1 and removed at regular intervals. The initial study revealed that the time required to achieve a suitably hydrophobic surface using the parameters published by Liang et al. (88) was after an immersion time of 120 min whereby a contact angle of >100° was measured. The contact angle versus immersion time is given in Figure 41. The 120 min required to produce a suitable hydrophobic coating is used as a minimum time for the systematic study with a maximum time of 360 min as published by Liang et al.

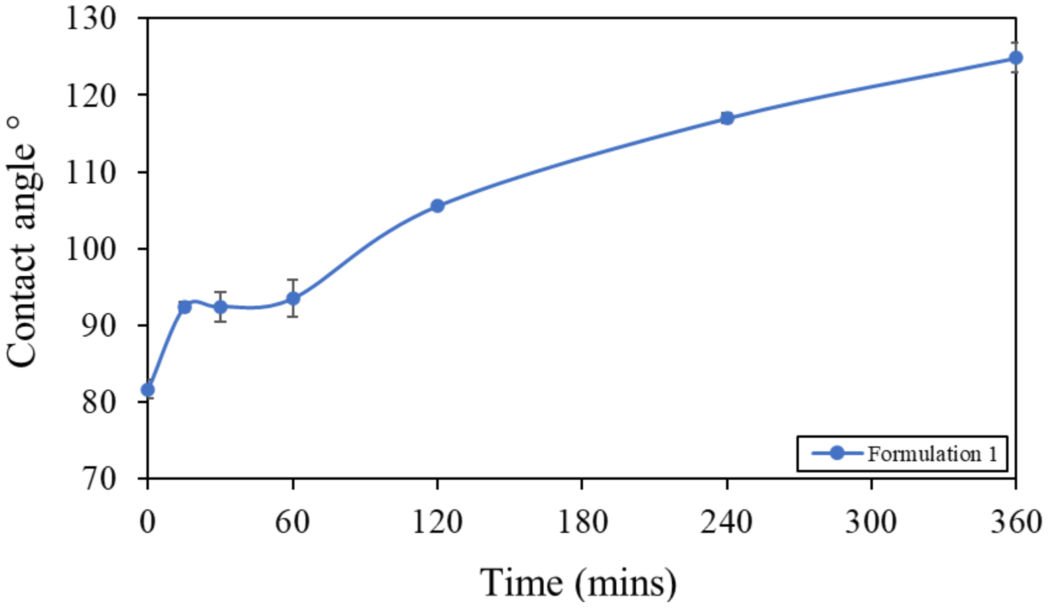

Figure 41. CA vs. immersion time for formulation 1 over 360 min immersion.

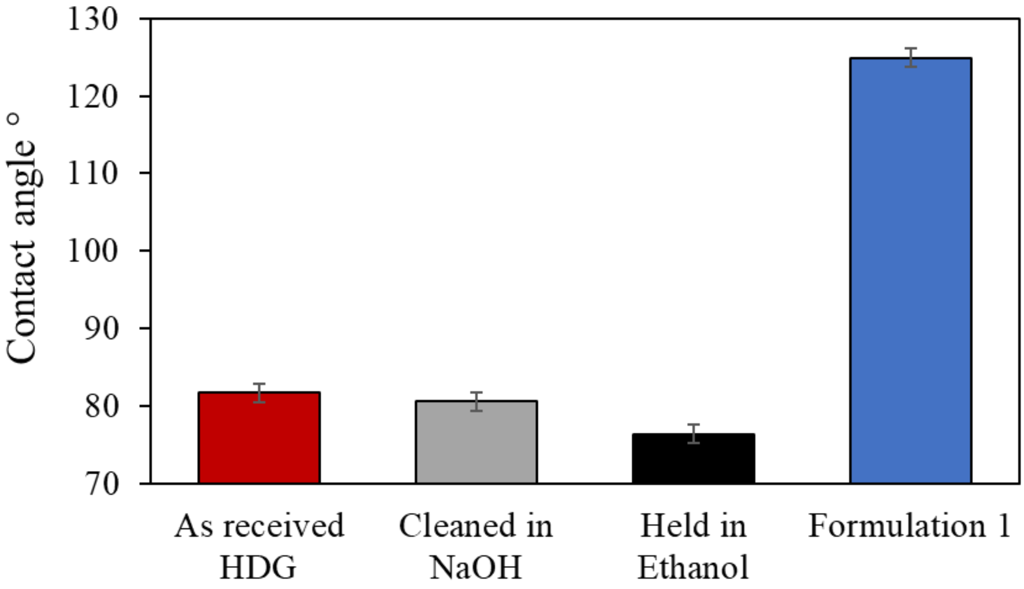

Figure 42. Recorded CA of HDG steel, which has been "as received", cleaned in NaOH, cleaned in NaOH and immersed in ethanol and cleaned and immersed in the coating formulation.

The contact angle of HDG steel samples with each surface treatment is shown in Figure 42. There was very little change in CA for HDG samples that were cleaned or rinsed in ethanol compared to the as received HDG steel sample. However, there was a significant increase in CA (>120°) recorded for HDG steel immersed in formulation 1. This demonstrates that the surface cleaning conditions typically employed in industry do not contribute to increased CA.

An additional study was conducted to assess the performance of the coated surface using the experimental procedure published by Liang et al. with and without the addition of SiO_2 (88). Figure 43 showcases how the addition of SiO_2 increases the contact angle when in comparison to the stearic acid control. This study determines that SiO_2 plays a positive role in contributing to increasing the hydrophobicity of the surface as well as the formulation of Zinc Stearate. Furthermore, the addition of NaOH to the formulation shows a positive relationship in improving surface hydrophobicity.

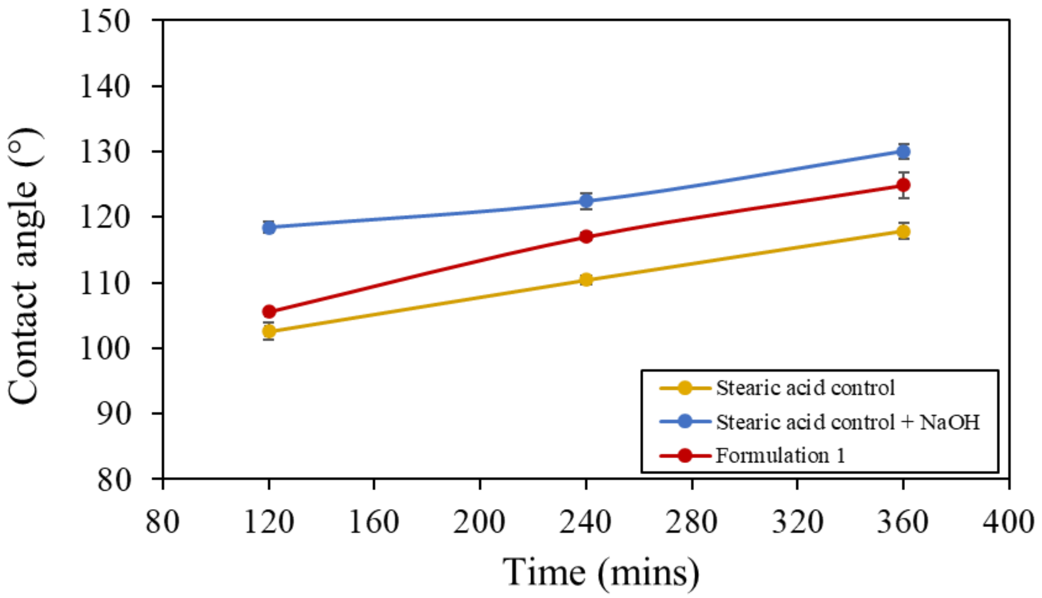

Figure 43. Relationship between CA against immersion time for stearic acid formulation with and without 2% wt. NaOH addition.

The minimum time of 120 min was used in a systematic study to investigate variables including the solvent, the addition of NaOH, stearic acid molarity and SiO_2 particle size. Surface morphology and CA were assessed as a function of the formulation shown in Table 10. Throughout the systematic study, 14 formulations were investigated; however, the key findings and trends will be reported by examining a subset of these.

6.3 Results and Discussion

6.3.1 Surface Morphology and Wettability

The published methodology used by Liang et al. used ethanol to dissolve stearic acid. However, stearic acid has been shown to be more soluble in isopropyl alcohol (IPA) than in ethanol (159,160). The increased solubility provided by using IPA would allow for higher concentrations of stearic acid to be used and may also have different morphology of the resultant hydrophobic coating when compared to that produced using ethanol.

Hydrophobic surfaces were produced by submerging HDG steel samples in formulations 1–3 given in Table 10 for up to 360 min. The surface morphology was observed using SEM imaging, which is shown in Figure 44 (a–d). Figure 44 (a) shows a HDG steel surface that has been cleaned in 1 M sodium hydroxide solution for 15 s at 50 °C. Figure 44 (b–d) shows that the surface morphology of the HDG steel dramatically alters after immersion in the experimental formulation compared to that of the cleaned HDG steel surface shown in Figure 44 (a). Figure 44 (b) shows the surface morphology consists of lamellar structures when using ethanol as the solvent. Liang et al. reported similar structures in their work and suggested that the structures observed here are zinc stearate with silicon dioxide entrapped amongst the structure, shown by the lighter areas (88).

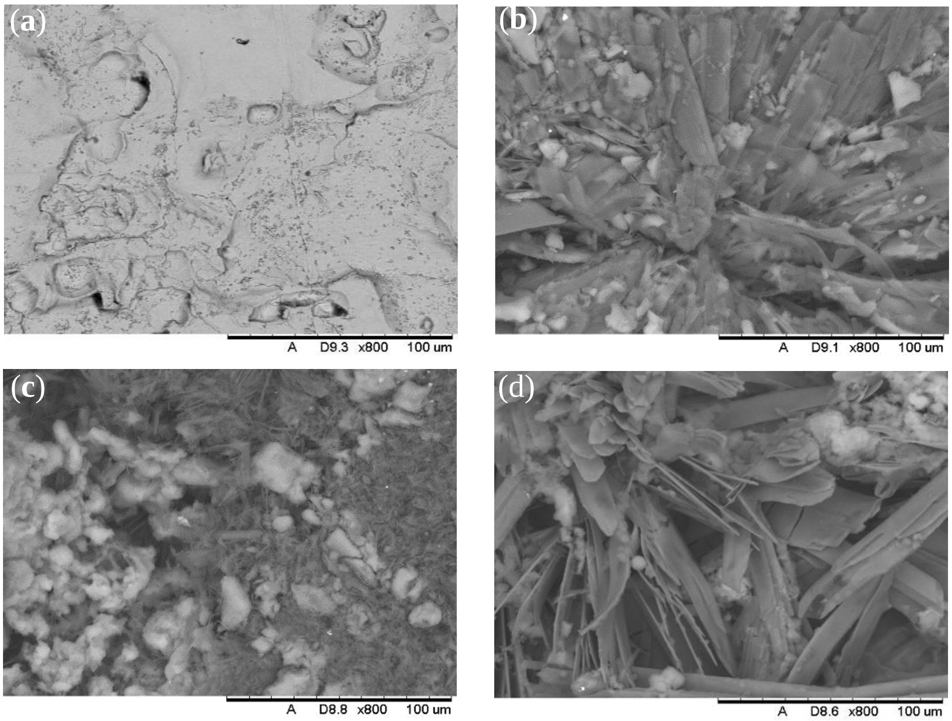

Figure 44. SEM images of fabricated coatings after immersion (a) uncoated, (b) formulation 1 (ethanol, 0.05 M stearic acid and micro-SiO2) for 360 min, (c) formulation 2 (IPA, 0.05 M stearic acid and micro-SiO2) for 360 min and (d) formulation 3 (ethanol, 2% wt. 1 M NaOH (aq), 0.05 M stearic acid and micro-SiO2) for 360 min.

The surface morphology observed in Figure 44 (c) is produced from formulation 2, whereby IPA is used as the solvent, replacing ethanol. Here, the zinc stearate has formed in a dense needle-like precipitate compared to Figure 44 (b) allowing larger floccules of silicon dioxide to be entrapped. Figure 44 (d) shows the surface morphology produced from formulation 3, which is ethanolic-based containing an addition of 2% wt. 1 M NaOH (aq). The morphology shown here is similar to that shown in Figure 44(b); however, the lamellar structures appear to be larger and less densely packed compared to that shown in the non-NaOH addition shown in Figure 44 (b).

CA measurements for HDG steel samples immersed in formulations 1–3 for up to 360 min are shown in Figure 45. The maximum CA recorded for each sample generally occurred after 360 min of immersion with 125° for formulation 1, 135° for formulation 2 and 125° for formulation 3. The increase in CA recorded for formulation 2 can be attributed to the different surface morphology compared to that formed by samples immersed in formulation 1 or 3. Studying Figure 44(b-c), the morphology is significantly altered when using IPA as a solvent compared to that of ethanol, due to stearic acids higher solubility within IPA. The dense needle-like precipitate entraps more silicon dioxide and would provide a rougher surface, which could explain the increase in CA observed. Increased surface roughness can impart functionality to the surface via hydrophobicity. A higher density of surface features entraps air, which limits the liquid droplet’s ability to rest on the surface and permeate through to the underlying substrate. This increase in surface roughness corresponds to an increase in CA (161,162).

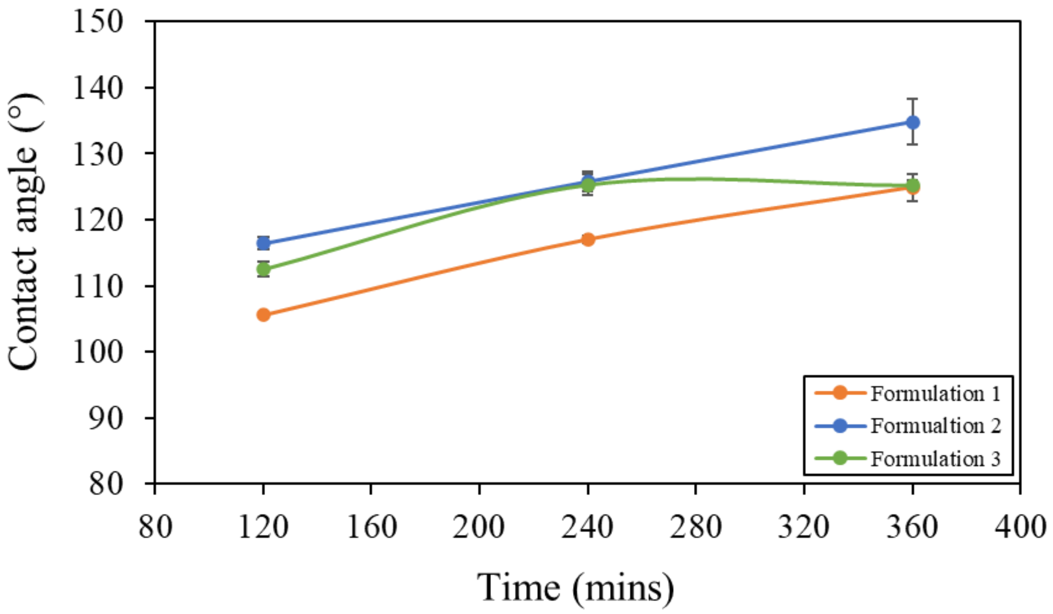

Figure 45. CA against immersion time for formulations 1–3 from Table 10.

Formulation 3 has an addition of 2% wt. 1 M NaOH (aq) compared to that of formulation 1. Figure 46 showcases the difference in coating homogeneity when an addition of 2% wt. 1 M NaOH is present within the coating formulation. NaOH was introduced to increase the pH, which acts to activate the HDG steel surface and assist in increasing the homogeneity of the coating across the substrate surface. Zinc stearate structures form in similar lamellar plate shapes to those formed from formulation 1.

The maximum CA recorded is the same as that for formulation 1, which can be explained by the very similar surface morphology. However, the main advantage of the addition of NaOH was that of improved coating homogeneity. The improved coating homogeneity can be attributed to the increased activation of the HDG surface through the introduction of NaOH (163). Due to the increased homogeneity of coating formation, it was decided to include 2% wt. 1 M NaOH within all subsequent formulations.

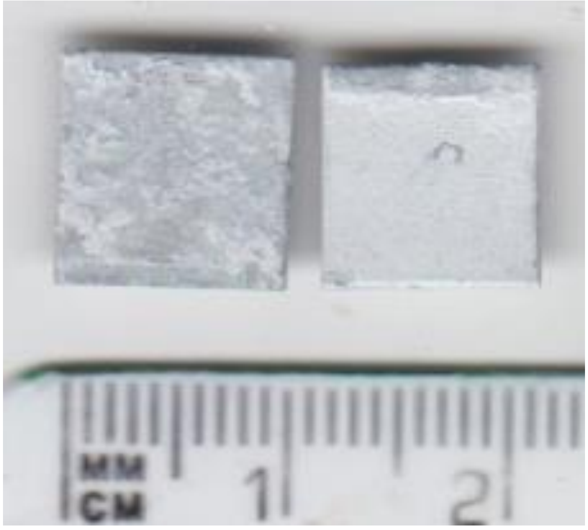

Figure 46. Image taken of hydrophobic samples coated with formulation 1 (left) and 3 (right) without and with 2% wt. 1 M NaOH addition, respectively.

Altering the molarity of stearic acid within the solution provided improved results by increasing surface CA whilst simultaneously decreasing immersion time. Additions of Stearic acid at concentrations of 0.05, 0.1 and 0.2 were evaluated within ethanol and IPA. Figure 47(a–c) shows the increase in molarity visibly affects the crystalline structure formed after a 360-min immersion period. Molarity increases over the three samples showed zinc stearate transition from needle-like structures to form lamellar structures. There is an increase in the population of zinc stearate and SiO_2 over the sample's surface, filling in open crevices left within the coating. CA measurements, shown in Figure 48, show that 0.2 M gave a negligibly higher CA in comparison to 0.1 and 0.05 M, recorded at 128°, 127° and 126°, respectively, when immersed for 360 min.

However, with increased molarity, higher CA was achieved in a shorter immersion time. This is demonstrated by formulations 7 and 8. Formulation 8 returned the greatest CA of 146°, in an immersion time of 120 min. Reducing the immersion time required to produce the coated surface is a crucial factor in improving the coating's industrial viability. Figure 47(d) shows the surface morphology of this sample, zinc stearate is formed in needle-like structures encapsulating floccules of SiO_2. The smaller needle structures are distributed more evenly across the surface, thereby, achieving better coating surface homogeneity. This enables air to be retained between zinc stearate and SiO_2 molecules. In turn, this contributes to a rougher surface that stops water droplets from permeating between pores, increasing the CA measured and surface hydrophobicity (88,164).

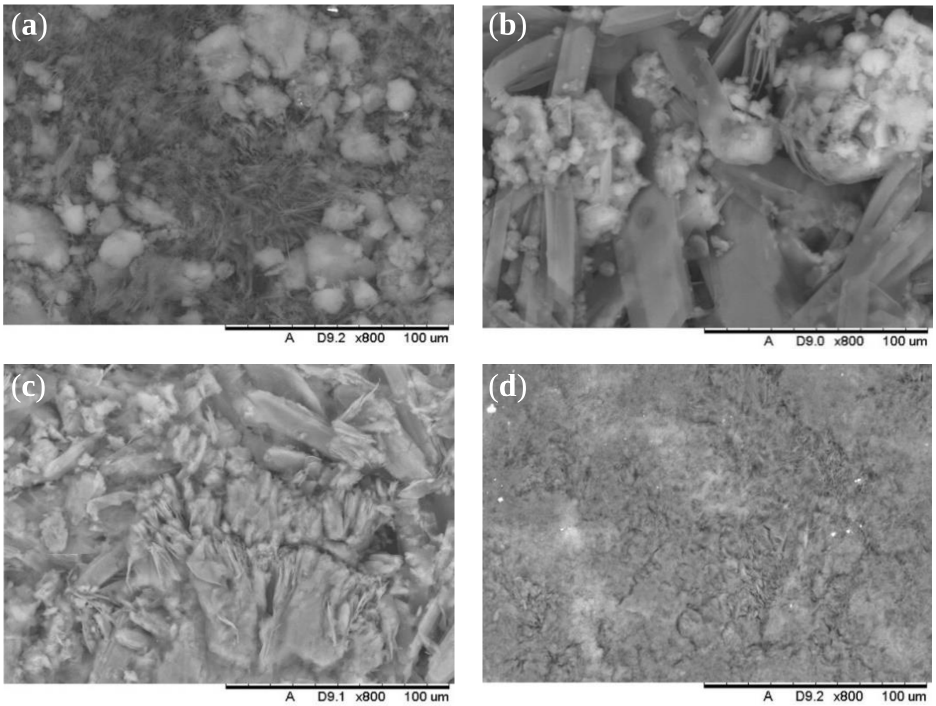

Figure 47. SEM images of fabricated coatings after immersion in (a) formulation 6 (IPA, 2% wt. 1 M NaOH (aq), 0.05 M stearic acid and micro-SiO2), (b) formulation 7 (IPA, 2% wt. 1 M NaOH (aq), 0.1 M stearic acid and micro-SiO2), (c) formulation 8 (IPA, 2% wt. 1 M NaOH (aq), 0.2 M stearic acid and micro-SiO_2) all for 360 min and (d) formulation 8 (IPA, 2% wt. 1 M NaOH (aq), 0.2 M stearic acid and micro-SiO_2) for 120 min.

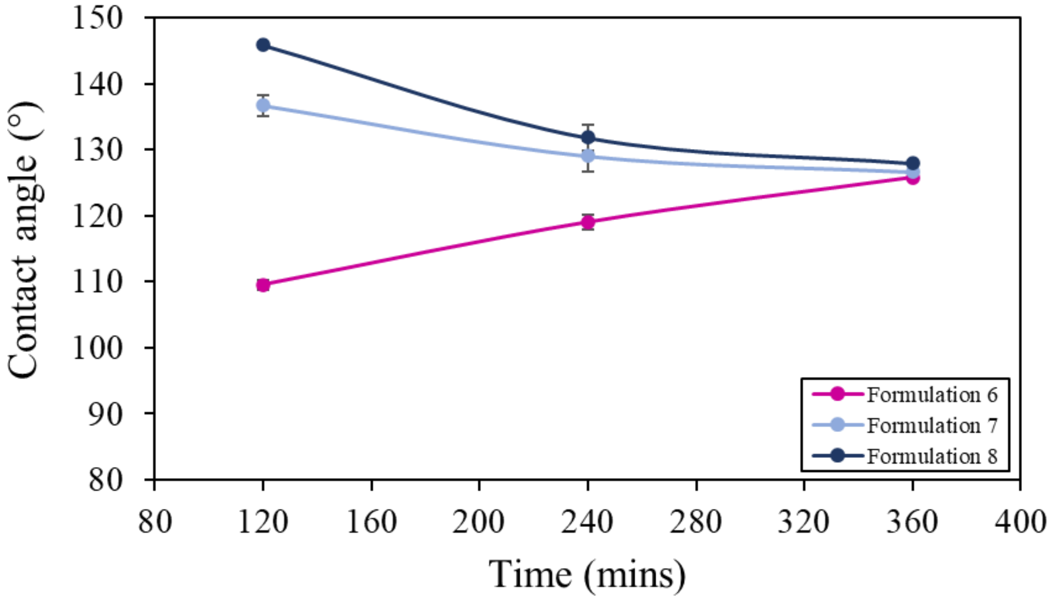

Figure 48. CA against immersion time for formulations 6–8 from Table 10.

The particle size of additive SiO_2 was also assessed. Particle sizes of 9–20 nm were used, compared to the 0.2–0.3 µm that was used throughout the systematic study. Figure 49 demonstrates that a similar trend was found between CA and immersion time for the nanoparticles and microparticles of SiO_2. When the molarity is low, there is a positive relationship between immersion time and CA. As the molarity is increased, the initial CA is found to be higher but then decreases with increased immersion time. This is demonstrated by formulation 12, which has a CA of 118° and 129° at 120 and 360 min, respectively. In comparison, formulation 14 has a CA of 135° and 131° at 120 and 360 min, respectively.

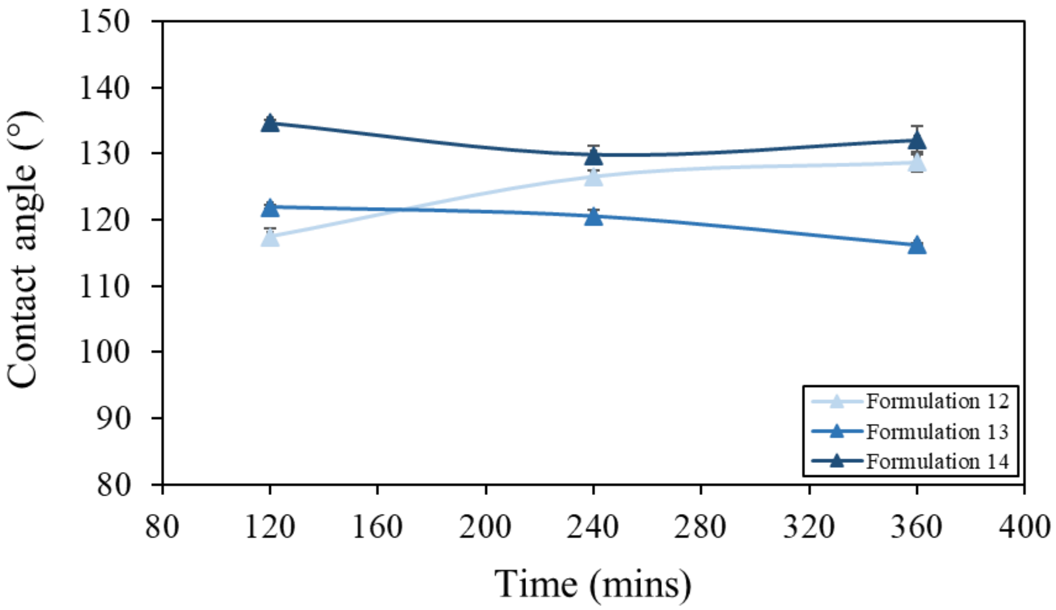

Figure 49. CA against immersion time for formulations 12-14 from Table 10.

One theory for why CA decreases with increased immersion time is due to the SiO_2 formation blanketing the crystalline structure on the substrate surface. Increased SiO_2 deposition leads to decreased surface roughness and contributes to reducing the hydrophobicity of the substrate surface over time. The surface morphology is demonstrated in Figure 50(a-b), and the change in structure with increased immersion time is attributed to the increased SiO_2 deposition. AFM was utilised to validate this theory by evaluating the surface roughness of the specimens from formulation 8 at 120 min and formulation 14 at 120 and 360 min. When analysing the data on formulation 14 from Table 11, we observe that the roughness values decreased between the two samples. This validates the previous assumption showing that hydrophobicity can be negatively impacted in comparison to when lower concentrations are used within a solution. The AFM maps for the surface roughness are shown in Figure 51.

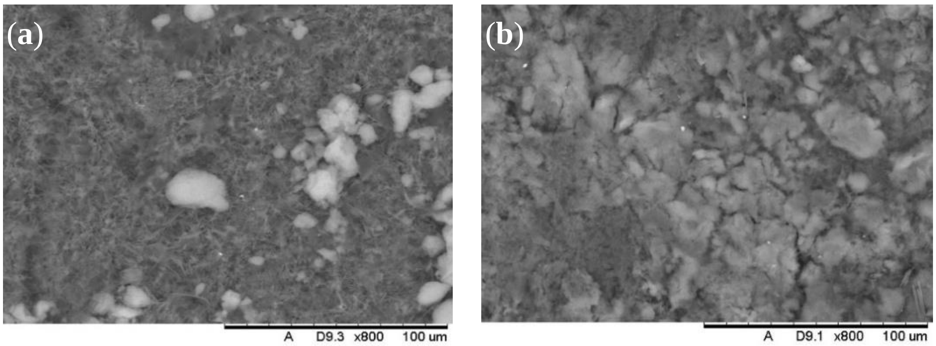

Figure 50. SEM images of fabricated coatings after immersion in formulation 14 (IPA, 2% wt. 1 M NaOH (aq), 0.2 M stearic acid and nano-SiO2) for (a) 120 min and (b) 360 min.

Table 11. Surface roughness data via AFM from samples coated in formulation 8 and 14.

Surface Roughness	**Formulation 8**	**Formulation 14**	
	120 min	**120 min**	**360 min**
Average, S_a	194 nm	77 nm	47 nm
RMS, S_q	243 nm	101 nm	64 nm

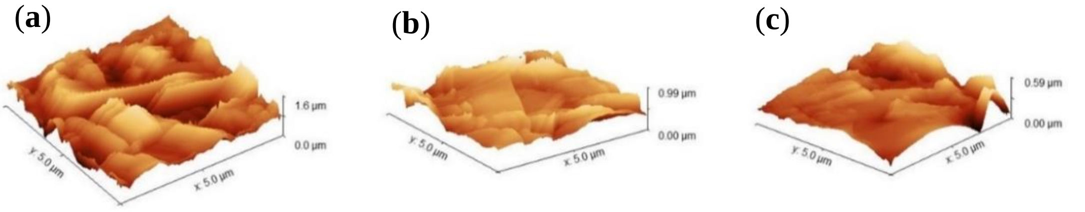

Figure 51. Topographical images produced by AFM of samples coated (a) in formulation 8 for 120 min, (b) formulation 14 for 120 min and (c) formulation 14 for 360 min.

6.3.2 FTIR Analysis

FTIR analysis was conducted to determine the changes in the different functional groups that form due to the reaction of stearic acid and zinc. Figure 52 shows FTIR spectra for SiO2, the hydrophobic surface formed and stearic acid. Peaks at 1099 and 810 cm−1 in Figure 52 (a) relate to the symmetric and asymmetric stretching vibration of Si-O-Si bonds, whilst 462 cm−1 relates to the Si–O bending vibration absorption (32,33). The 2915 and 2850 cm−1 peaks in Figure 52 (b-c) correspond to C–H bonds on the hydrophobic surface and in stearic acid, respectively.

Figure 52 (c) shows peaks located at 1705 and 940 cm−1, which represent C–O stretching vibration and the absorption peak of the hydroxyl group (–OH) in the carboxyl group (–COOH). These peaks are not present in Figure 52 (b) and are instead replaced by peaks at 1540 and 1397 cm−1. These changes demonstrate the –COOH present in stearic acid has changed, with H replaced by Zn (10,34). This change demonstrates the preparation of the zinc stearate hydrophobic surface onto the HDG steel surface. The chemical reaction observed is stated in Equations (33) and (34).

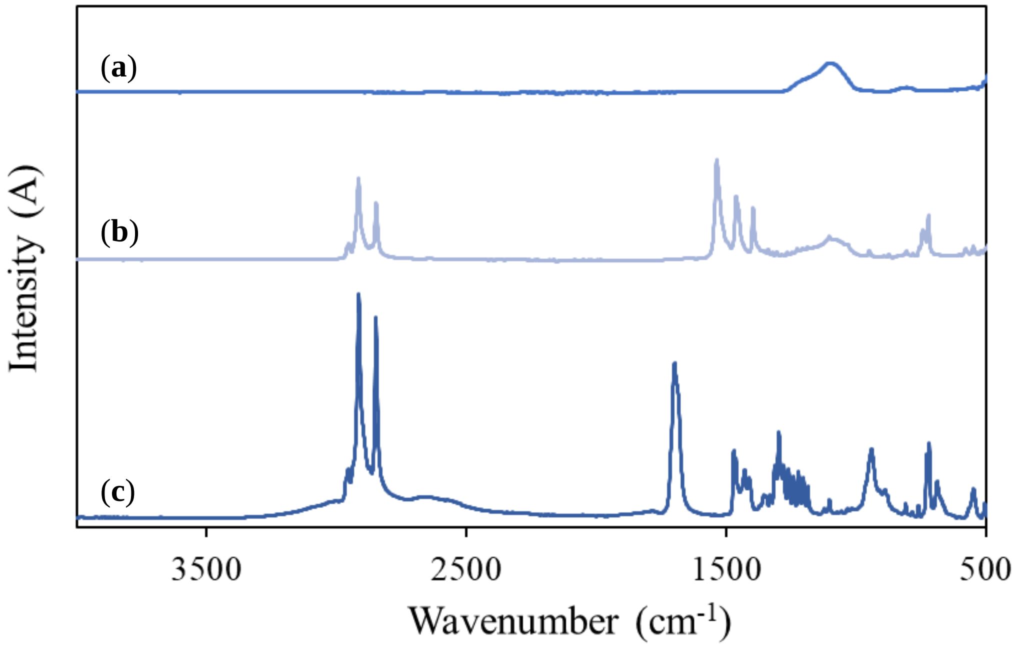

Figure 52. FTIR spectra of (a) SiO2 (b) hydrophobic sample and (c) stearic acid.

6.3.3 Investigation into the use of a higher boiling point solvent

It was hypothesised that the production of the zinc stearate coating could be limited by the kinetic rate of hydrothermal growth that occurred when in solution. Thus, it was questioned whether altering conditions and increasing solution temperature could improve zinc stearate creation rate, potentially reducing production time and/or improving the coating performance altogether. Under the same coating procedure utilised throughout the systematic study, the processing temperature was limited by the solvent boiling point, which, for ethanol and IPA is approximately 70 °C. The alcohol, L-butanol presented significant interest as it has a significantly higher boiling point (117 °C) and is more stearic acid soluble than IPA (165). Therefore, if used in solution it could allow operating temperatures to be increased. From there an assessment could be made on whether the coating formulation was improved and if there was a successful balance between stearic acid and zinc stearate solubility. Figure 53 illustrates the CA data recorded for HDG steel samples submerged in butanol as the solvent for two different temperatures, 70°C and 100°C.

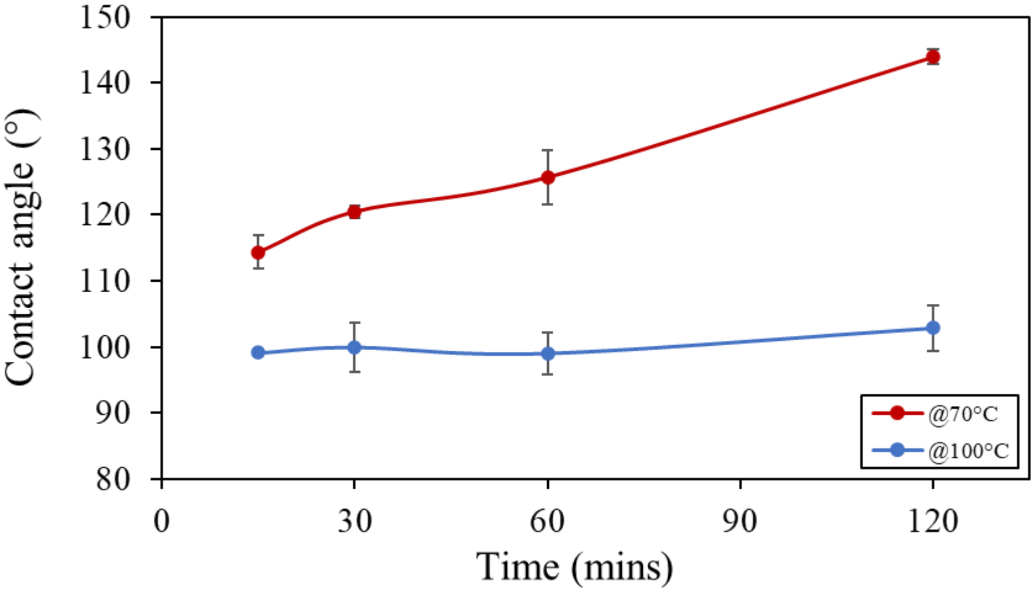

Figure 53. CA against immersion time for both formulations using butanol as the solvent at a temperature of 70°C and 100°C.

It is apparent from both data sets illustrated on the graph that temperature plays a significant role in the development of the zinc stearate coating. Firstly, analysing the data shown for temperatures at 70°C a positive linear relationship is shown between increased immersion time and CA recorded. A maximum CA of 145° is recorded after 120 min immersion. This is very similar behaviour to that observed when formulation 8 was utilised. However, the most significant finding is that even at relatively low immersion times of 15 and 30 min, CA is significantly increased in comparison to uncoated HDG steel. CA is measured at 114° for 15 minutes of immersion, a significant increase in surface hydrophobicity of uncoated HDG steel by ~140%. The improvement in hydrophobic performance is considerable for such a short immersion time and demonstrates the validity of utilsing L-butanol as a solvent. SEM images for the coating morphologies produced throughout the study are shown in Figure 54.

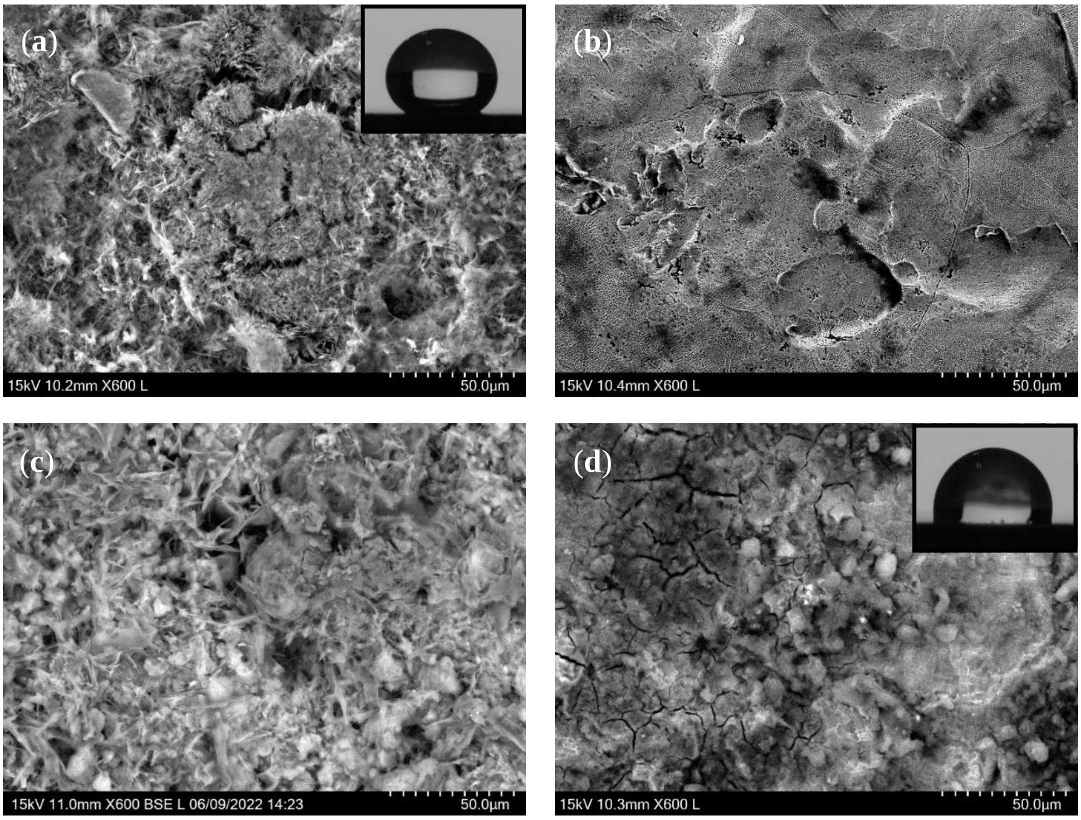

Figure 54. SEM images of fabricated coatings after immersion in formulation utilising L-butanol as the solvent (butanol, 2% wt. 1 M NaOH (aq), 0.2 M stearic acid, and micro-SiO_2) at (a) 70°C for 15 min, (b) 100°C for 15 min, (c) 70°C for 120 min and (d) 100°C for 120 min.

The crystalline structure formed when butanol was utilised at 70°C is shown in Figure 54 (a) and (c) for 15 and 120 minutes respectively. The morphology of the crystalline structure shows a distinctive change between the two time periods. After 120 minutes lamellar/feather-like zinc stearate structures are formed with the encapsulation of SiO_2, is regularly observed with the other versions of the zinc stearate coating, promoting good hydrophobicity. Despite the shorter period of immersion for the sample in Figure 54 (a) the morphology clearly shows the formation of the hydrophobic zinc stearate coating. The notable difference between the 15 and 120 min samples, is the reduced development of the crystalline structure. This is attributed to the reduced period of immersion necessary to elicit greater hydrothermal crystal growth. Encouragingly, even with a much-reduced immersion time, suitable coating homogeneity is achieved with good hydrophobicity. Reducing the coating production time by ~90% and making the process much more industrially viable.

In contrast, the study at 100°C returned significantly different results. The CA data recorded, remained nearly constant over the investigation, with all samples returning measurements of approximately 100°. This was due to insufficient coating of the substrate at higher formulation temperatures. SEM images of the substrate after 15 minutes and 120 minutes at 100°C are shown in Figure 54 (b) and (d) respectively. For the 15 min sample, it is quite obvious that the coating has not sufficiently formed across the substrate and thus this can explain why a low CA of 99° was recorded. On investigation of the 120 min sample in Figure 54 (d), there is also insufficient coating observed. Larger areas of SiO_2 'blanket' cover the substrate surface, adhering poorly and leaving a dusty residue. Thus, hydrophobicity is not significantly improved and is recorded at 103°. Insufficient coating occurs due to the higher working temperature of 100°C.

It is hypothesised that raising the temperature of the solvent too high can negate zinc stearate formation on the substrate surface. Increased temperatures can increase the esterification reaction between butanol, stearic acid and zinc. If these temperatures are raised too high it could cause the esterification rate of zinc stearate to become inefficient for coating, with the reaction consuming the available reactants (166). Additionally, increased formulation temperatures can cause the solubility of zinc stearate to be significantly increased due to increased kinetic energy experienced within the system, breaking intermolecular bonds between the solute and solvent. The increase in solubility of zinc stearate in solution means that the lamellar zinc stearate structures are unable to grow at the substrate surface and create a homogeneous coating layer.

6.3.4 Optimal Coating Parameters

It was observed that the optimal coating system was shown to be formulation 8. This formulation consisted of 0.2 M stearic acid, 1% wt. SiO_2 (0.2–0.3µm), 2% wt. 1 M NaOH and was immersed for 120 min achieving a mean contact angle of 146°. This system provided the most hydrophobic surface and demonstrated a more homogeneous coating throughout.

6.3.4.1 Cut edge analysis

To analyse the thickness of the coating, a prefabricated sample coupon coated in formulation 8 was held and set in resin at 90°. The sample was then meticulously ground and polished to expose the cross-section of the sample. EDX was utilised in order to chemically assess and characterise the coating layers apparent in the image. This can be observed in Figure 55. The average coating thickness was observed at 27µm with a standard error of ±1.2µm.

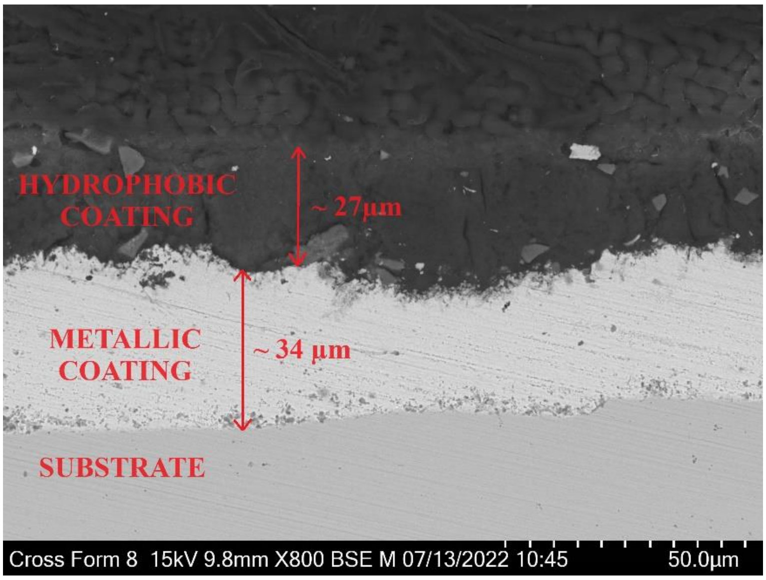

Figure 55. Cross-section SEM image of formulation 8 displaying coating thickness layers.

6.4 Conclusions

A systematic study was employed to improve the processability of a one-step hydrophobic coating for HDG steel and to make it more industrially appropriate. The variables highlighted throughout the study included the immersion time, the solvent used, the addition of NaOH, molarity and SiO_2 particle size. The best-performing coating demonstrated a CA of 146° from an immersion time in formulation 8 for 120 min. The formulation variables were IPA used as the solvent, 2% wt. 1 M NaOH (aq), 0.2 M stearic acid and micro-SiO_2 (0.2–0.3 µm). It was observed higher molarities of constituent elements led to higher CA recorded and subsequently decreased immersion times. This was due to higher concentrations of the active ingredients available, which was hypothesised to improve the coatings ability to form Zinc Stearate on the substrate surface.

When comparing this methodology to other one-step processes by Li et al., we observed that, despite a longer processing time, the use of more commercially available, economically viable and safer constituents within the formulation justifies its development. The methodology displays significantly reduced health and safety risks and avoids the use of toxic chemical nitrates (100,109). In comparison to Laing et al., the processing times were reduced by 67%, and the use of chemical additions, such as fumed silica, provided a vastly cheaper and safer alternative to nano-silica (88).

While the processing times were reduced by 67%, the process of creating hydrophobic coatings remains in hours not minutes. In practice, this means that it is suitable for batch processing only given that inline residence times require processing times in tens of seconds. The limiting factor is the kinetic rate of hydrothermal growth of the zinc stearate, and it has been demonstrated that this cannot be manipulated through changes in stearic acid solution concentration.

The processing temperature is limited by the solvent boiling point, which, for ethanol and IPA, limits this to ~70 °C. Any further increase would risk boiling, altering the chemistry of the bath and producing a significant health and safety risk. Any change to a higher boiling point solvent would need to balance the solubility of the stearic acid and zinc stearate to ensure that the stearate can be added to the solution while retaining the insolubility (or sparing solubility) of the zinc stearate. The utilisation of L-butanol as the solvent showed a significant reduction in processing times to produce a hydrophobic surface. Under the same experimental parameters, a CA of 114° was produced after only 15 minutes of immersion. This was a ~140% increase in surface hydrophobicity in comparison to uncoated HDG steel. Raising the temperature of the formulation to 100°C did not have a positive effect on the hydrothermal crystal creation rate. Increased temperatures increased the solubility of stearic acid within the formulation, as a result inadequate coating conditions were present to effectively fabricate the hydrophobic coating.

Zinc is the dominant metal used in galvanising; however, it is also common that other alloying materials, such as magnesium and aluminium, are added to the metallic coating to further improve the corrosion resistance. The inclusion of these alloying compounds offers the possible formation of other metal-organic compounds as well as zinc stearate. The impact on hydrophobicity should also be investigated for these materials. This would help to identify the universality of the coating across the broad range of zinc-coated steel substrates. The coating demonstrated a significant improvement in corrosion resistance during industry standard humidity testing; however, the physical robustness also needs to be considered in any lifetime prediction. Further evaluation of the relative abrasion resistance and friction would be beneficial in estimating the real-world product lifetime extension provided by the zinc stearate coating.

7 Further investigation of a novel hydrophobic coating for hot-dipped galvanised steel

7.1 Introduction

The functional coating studied in Chapter 6, demonstrated a significant improvement in corrosion resistance and enhanced hydrophobicity during industry-standard testing methods. Throughout this chapter, it was chosen to continue the investigation into the hydrophobic coating. Although processing times were reduced by 67%, the coating process remained in hours not minutes. Developing a coating appropriate for roller coating was the primary aim of this thesis. However, interest from Tata Steel and feedback from the publication of the original work investigating the hydrophobic coating (167) highlighted that, the coating could play an interesting role in post-production processes and therefore was worthy of further study. This further study was driven to explore more definitive physical robustness testing and analysing metrics of corrosion resistance beyond visual attributes and surface tension measurements as examined in Chapter 6.

Previous literature has stated that the hydrophobic coating demonstrates a considerable improvement in corrosion resistance (88). Polarisation resistance (R_p) is a key metric used to determine the resistance of a substrate during a corrosive process and it is inversely proportional to the corrosion rate. Previous literature has stated that the zinc stearate hydrophobic coatings, similar to formulation 1, had reduced the corrosion current density, indicating an improvement in the corrosion resistance when analysed via EIS. It was demonstrated that hydrophobic coated samples produced larger charge transfer resistance compared to uncoated zinc, which represented the slower corrosion processes observed (88).

However, additional corrosion analysis was necessary to provide quantitative and qualitative data on the coating's real-life resistance to corrosion. Evaluation of the physical robustness was necessary to assess the coating's formability and durability. This allowed the real-world product lifetime extension provided by the zinc stearate coating to be evaluated appropriately. The principal aims of this research chapter were to conduct a systematic study that:

- Further investigated the corrosion resistance of the zinc stearate coating quantitively using advanced techniques such as SVET, EIS and accelerated exposure tests.
- Evaluated the physical robustness of the zinc stearate coating via two novel tests looking specifically at formability and durability.

7.2 Methods

7.2.1 Materials

Sodium hydroxide, hydrogen peroxide (30%), stearic acid, and silicon dioxide (9–20 nm) were purchased from Sigma Aldrich (St. Louis, MO, USA), ethanol and IPA were purchased from Fisher Scientific (Hampton, VA, USA). Fumed silicon dioxide (Aerosil 300, Essen, Germany, 0.2–0.3 µm) was obtained from Evonik. All chemicals used were of reagent grade. Hot-dipped galvanized (HDG) steel was provided by Tata Steel (Port Talbot, Wales).

7.2.2 Methods

7.2.2.1 Sample preparation

A one-step immersion method was used to coat HDG steel samples via the same process and parameters as observed in Chapter 6 unless otherwise stated. For the formability study, HDG steel specimens were cut into appropriate dog bone specifications, appropriate to standard ISO-6892-1, and then coated with formulation 8 to produce the zinc stearate coating (168).

7.2.2.2 Characterisation techniques

Many of the same techniques used to characterise the surfaces were repeated from Chapter 6. Surface morphology was visualised using SEM and EDS (Hitachi TM4000) (Tokyo, Japan). CA was measured with a goniometer system comprised of a CCD camera, and contact angle software (Software version 4.0.3.1, Osilla) (Sheffield, UK) with an error measure of ±1° under optimized illumination and optical conditions. FTIR (PerkinElmer spectrum-100) (Waltham, MA, USA) and XRD (Bruker D8 Discover with copper source 40 kV and 40 mA) (Billerica, MA, USA) were used to characterise the surface chemical constituents. XRD was conducted with a glancing angle setup consisting of a 2° incidence angle in true parallel beam configuration and increments of 0.02°.

7.2.2.3 Corrosion tests

Advanced corrosion resistance was evaluated via the Scanning Vibrating Electrode Technique (SVET) (Built in-house, Swansea University, Wales) and Electrical Impedance Spectroscopy (EIS) (Gamry Instruments Interface 1010E^{TM}) (Warminster, PA, USA) further details on these techniques can be seen in Chapter 3.

Additionally, humidity testing was utilised to assess the real-life corrosion resistance of the coated substrate. Samples were placed at 45° and held at 35 °C and 100% humidity as per Standard ASTM D2247-15. Formulation 8 was utilised to fabricate the hydrophobic surface on HDG steel coupons measuring 80 mm × 65 mm. The investigation was conducted for up to 1000 hours. At intervals of 0, 250, 500 and 1000 hours a canon EOS 5D camera within a lightbox was used to photograph the samples, mass measurements were taken of each sample. Epoxy resin was used to seal the cut edges of the samples, and the water uptake of the resin was negated for and deducted from the final mass change values to achieve accurate and concurrent readings.

7.2.2.4 Physical robustness tests

Two novel techniques were carried out to assess the physical robustness of the zinc stearate coating after application to HDG steel. It is important to understand the formability of the coated steel strip and the effect that plastic deformation may have on the coating's effectiveness. Thus, a formability study was conducted whereby coated specimens were clamped into position and plastically deformed at 1mm/min in a Hounsfield double-column tensile tester, as seen in Figure 56. Dog bone specimens were manufactured in line with standard ISO-6892-1 (168). Four specimens were coated identically and three were subjected to elongation at 5%, 15%, and 30% strain. SEM images of the surface morphology were taken, and CA measurements were made to assess the relationship between coating hydrophobicity and coating deformation.

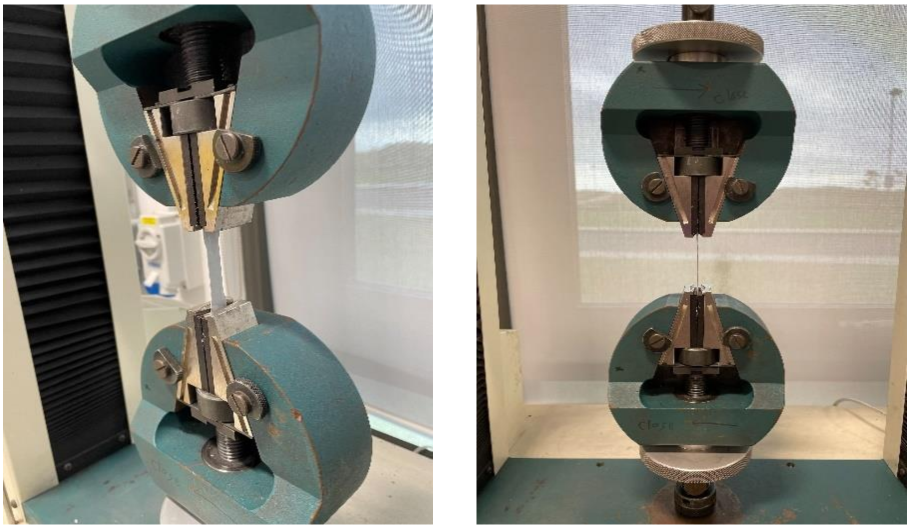

Figure 56. Images of Hounsfield tensile tester used to elongate coated dog bone samples during formability study.

Coating durability was evaluated via a novel test to analyse the surface hydrophobicity after significant abrasion to the surface. The test was completed by taking a precoated sample and performing a tape "pull-off" test, removing the top surface layer. Adhesive tape used in line with ASTM D3359 was utilised to perform the tape pull. The test targeted three 20 × 20 mm areas of the sample, and three tape pulls were repeated on each area. After each pull, gravimetric scales were used to measure the mass of the sample and deduce how much coating mass was removed after each test. CA measurements were then made across the three different target surface areas. This data was then used to assess coating durability via the relationship between surface hydrophobicity and reduction in coating weight.

7.3 Results and discussion

7.3.1 Corrosion analysis

7.3.1.1 Scanning vibrating electrode technique

Figure 57 shows the SVET derived normal current density false colour maps obtained for (a) uncoated and (b) coated HDG steel immersed in near neutral 1 wt % NaCl for 1 hr, 12 hrs, and 24 hrs. Net anodic regions, for which positive current density values are obtained, are shown as red on the maps, whereas the blue areas represent net cathodic regions. The optical images of the sample surfaces following 24 hr immersion in 1% w.t. NaCl solution are also shown in Figure 57.

Localised anodic regions can be observed in the bottom left of the uncoated sample (Figure 57a) from the start of the experiment, at ~ 0.45 Am^{-2}. As time progresses, the anodic activity spreads across the substrate's surface and several pit-like features can be observed (169). After 24 hours a large proportion of the HDG surface is covered by a white corrosion product typically formed during the anodic dissolution of zinc (134). The corroded regions on the sample surface correspond to regions of net anodic activity on the SVET false colour map, thus demonstrating the ability of the SVET to detect anodic dissolution. a direct comparison between the optical image and SVET derived surface maps shows a clear correlation between pitting and areas of significant anodic current density. The total integrated anodic current density as a function of time is shown in Figure 58. The anodic current density decreases as a function of time from ~0.45 Am^{-2} to ~0.15 Am^{-2} between 1 – 12 hr respectively. This decrease in current density can be associated with anodic activity becoming less localised and spreading over a greater area of the substrate’s surface. After this point, plateauing occurs, and anodic current density activity is seen to remain constant at ~0.15 Am^{-2}. It is believed that this is a result of the cathodic oxygen reduction reaction limiting the corrosion rate at the surface, this typically occurs when a corrosion product is present on the substrate’s surface (170).

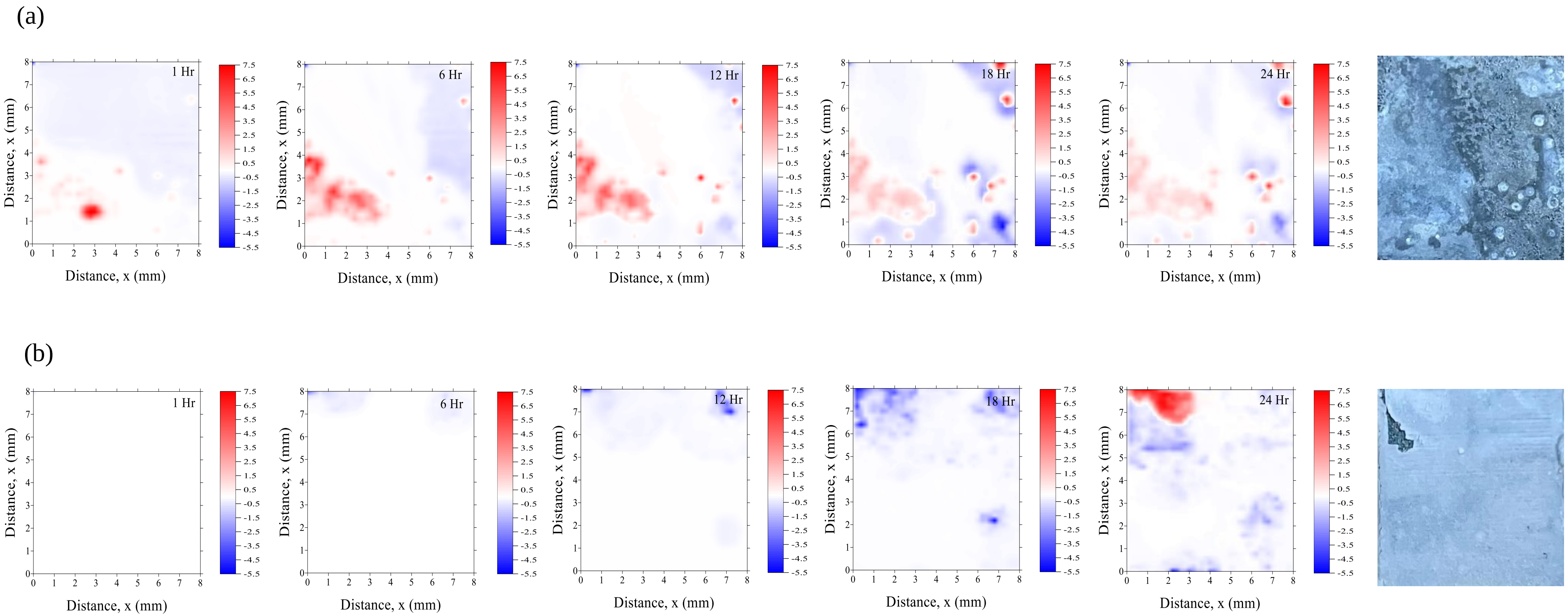

Figure 57. SVET derived surface maps and optical images of substrate surfaces showing the distribution of normal current density jz above intact (a) uncoated HDG steel and (b) formulation 8 coated HDG steel samples freely corroding in near neutral 1% w.t. NaCl after various immersion time plotted on Surfer 8.

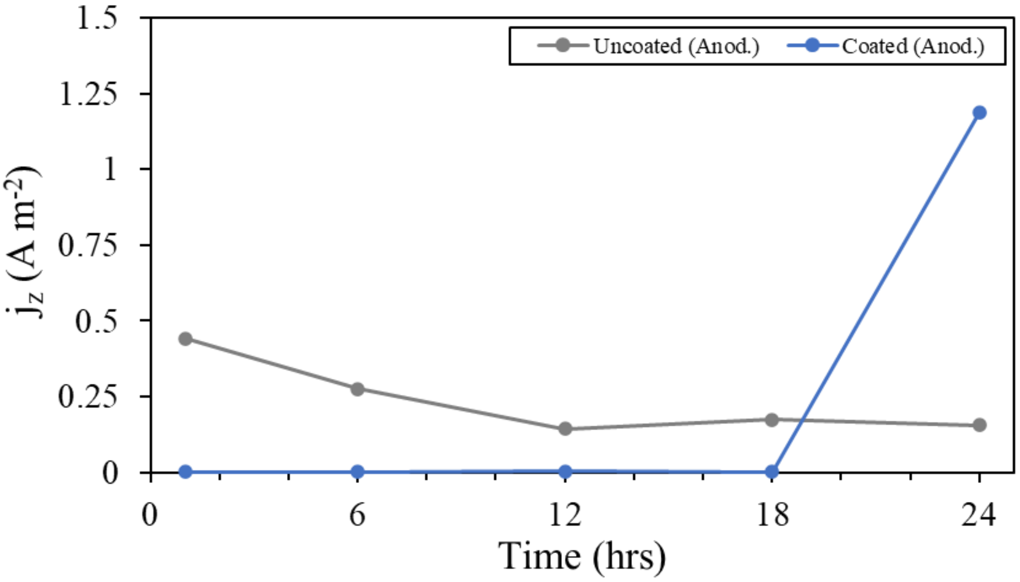

Figure 58. SVET derived data of anodic current density (j_z) as a function of time in the case of uncoated HDG steel and formulation 8 coating on HDG steel, immersed in 1% w.t. NaCl for 24 hours.

In comparison, when the hydrophobic coating was applied to the HDG steel, little-to-no anodic activity is observed between 1 and 18 hours of immersion. After 24 hours a net anodic region was observed in the top left corner of the sample. The data observed from Figure 58 corroborated this as minimal anodic current density activity was recorded up until 18 hours of immersion. After this point, anodic current density showed a sharp increase in net anodic current density to ~ 1.2 Am^{-2}. As previously observed in Chapter 6, the hydrophobic coating is white and dusty in nature (Figure 46). The optical image showing the substrate after SVET analysis (Figure 57b) shows an area of the coating was removed from the surface in the top left-hand corner of the sample. This removed area of coating corresponded with the SVET derived map (Figure 57b) and explained the increase in red anodic activity observed due to an exposed area of the substrate. It is hypothesised that the defected area of the coating was removed as a result of a defect within the film, which allowed columns of electrolyte to come into direct contact with the HDG sample surface through the porous structure, leading to potential delamination.

It is important to note that SVET detects net current values and is only able to detect localised corrosion currents that arise from anodic and cathodic sites separated by distances greater than the scan height (for this case it is ~100µm). Some current flux lines do not cross the scan plane and are not detected in situations when the separation is less than the scan height. This can cause issues in assessing some general corrosion problems (134,171). Despite this, it was concluded, that the hydrophobic coating delivered significant barrier properties, reducing high areas of anodic activity and protecting the metallic substrate surface beneath it against corrosion. Some porous areas of the coating were susceptible to electrolyte permeation, which in turn led to targeted areas of anodic activity. This delamination highlighted a potential concern for the long term durability of the coating. Therefore, further investigation was required to determine the longevity and more in-depth analysis of the coating for future application.

7.3.1.2 Electrical impedance spectroscopy

EIS was used in addition to SVET analysis as a supplementary method of analysis to generate non-destructive, quantitative data to compare the corrosion performance of formulation 1 and formulation 8. Due to the sensitive nature of EIS analysis, the response can indicate changes in the coating integrity long before any obvious damage manifests itself, as was observed with SVET analysis (137,172). Exposure to corrosive mediums/electrolytes can cause the capacitance and resistance of coatings to change over time. Figure 59 shows the Nyquist and Bode plots obtained for formulation 1 and formulation 8 after immersion in 5% w.t. NaCl for 24 hours.

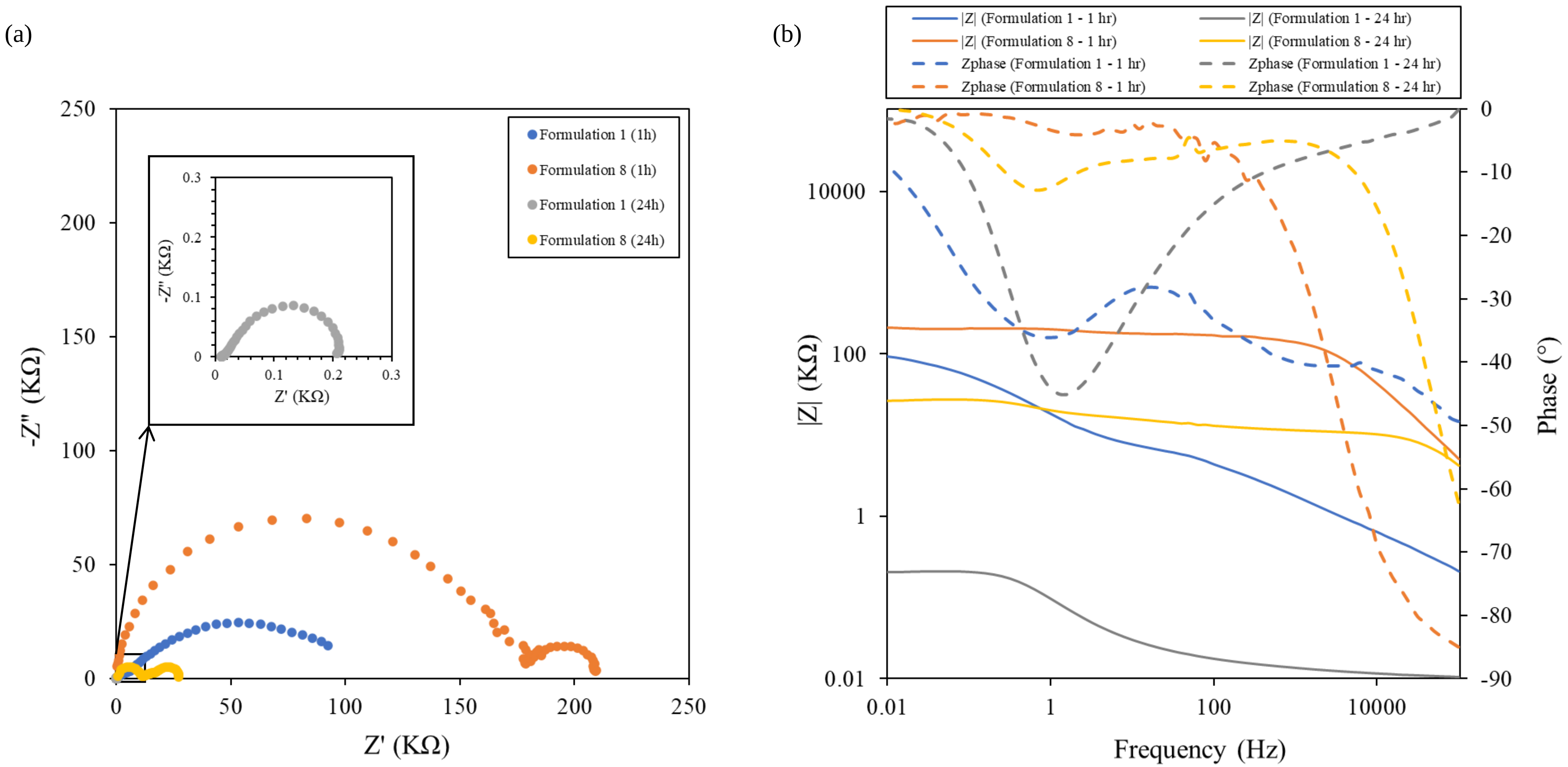

Figure 59. (a) Nyquist and (b) Bode plots produced using data obtained during EIS investigations of formulation 1 and formulation 8 coatings immersed in 5% w.t. NaCl for 24 hours. The input AC amplitude was 10 mV, the frequency range was from 0.01 Hz to 100 kHz and targeted a 10 cm^{2}area.

Figure 60 shows the equivalent electric circuit diagrams that were used for analysing the EIS spectra of formulation 1 and formulation 8. For formulation 1 a Randle's circuit was analysed (Figure 60a). For this equivalent circuit, solution resistance (R_s) was modelled in series with the parallel combination of substrate polarisation resistance and the double layer capacitance (C_{dl}) at the substrate/electrolyte interface. formulation 1 is plotted as a single semi-circle shape on the Nyquist diagram (Figure 59a), from the diameter of this plot we can derive C_{dl} and R_p respectively.

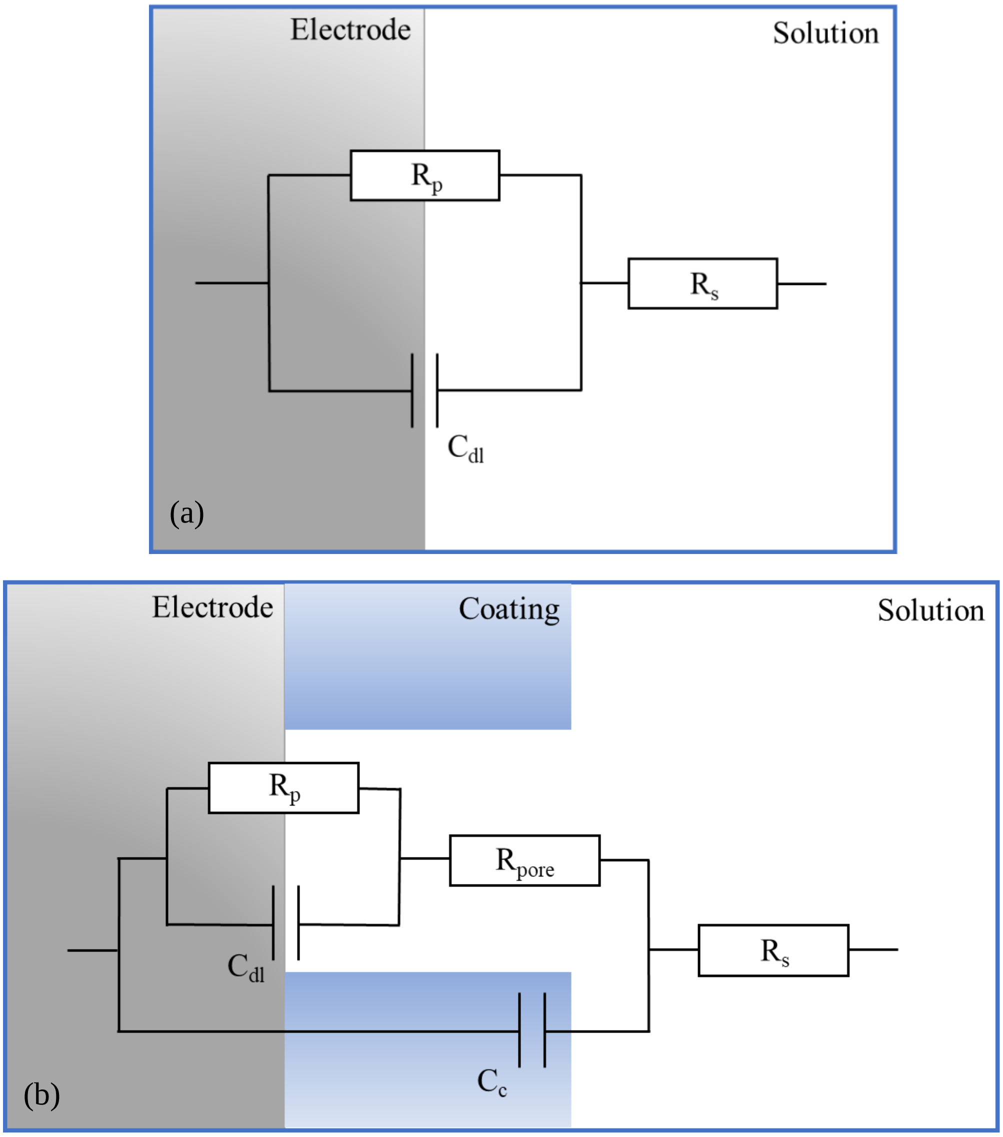

Figure 60. Equivalent electric circuit diagrams of coated HDG steel substrate with: (a) formulation 1 and (b) formulation 8 after 24 hrs immersion in 5% w.t. NaCl solution.

For formulation 8 the system is modelled using the circuit shown in Figure 60 (b). The data obtained for formulation 8 is shown on the Nyquist plot (Figure 59a) as two semi-circles. The diameter of the left-hand semi-circle is used to derive the pore resistance of the substrate (R_{pore}) and the diameter of the right-hand semi-circle is used to derive R_s. For this equivalent circuit R_p, $C_{dl,}$ and R_s are modelled as well as R_{pore}, due to the electrolyte permeation within the coating and the coating capacitance (C_c). Theoretical calculations were carried out to validate experimental values obtained through EIS analysis; these are shown in Table 12. Equations for calculating C_c and impedance, Z, for formulation 8 after 1 hr immersion in 5% w.t. NaCl solution are shown below. These calculations relate to the dark blue semi-circle pictured on the Nyquist plot (Figure 59).

$$\text{Coating capacitance, } C_c = \mathcal{E}_o \mathcal{E} A \,/\, d \tag{35}$$

$$C = (8.85 \times 10^{-12})((3+4.5)/2)(10) \,/\, (27 \times 10^{-6}) = 1.2 \times 10^{-9}\ \text{F}$$

$$\text{Impedance, } Z = 1 \,/\, 2\,\pi\, f\, C \tag{36}$$

$$Z = 1 \,/\, (2)(\pi)(2507)(1.2 \times 10^{-9}) = 52900\ \Omega$$

Where $\mathcal{E}_O$ is the permittivity of free space, $\mathcal{E}$ is the dielectric constant of the coating (for this coating is assumed to be equivalent to that of zinc stearate and silicon dioxide = 3.75)(173), A is the target area of coating exposed ($10 cm^2$) and d is equivalent to the coating thickness, 27 µm in this case. Theoretical solution resistance was estimated based on previous literature for 5% w.t. NaCl solution at room temperature (174).

Table 12. Theoretical parameter values calculated for formulation 8 after 1 hr immersion in 5% w.t. NaCl solution.

Parameter	Hr 24
C_c (nF)	1.2
Z (kΩ)	52.9
R_s (kΩ)	0.12

Table 13 displays the key metrics derived for formulations 1 and 8 derived from the equivalent electric circuits. The theoretical values calculated (Table 12) were compared to that of the EIS derived metrics (Table 13) ensuring consistency between theoretical calculations and practical results.

Table 13. EIS derived metrics for formulation 1 and formulation 8 coatings after immersion in 5% w.t. NaCl solution.

	Time (Hrs)	**Formulation 1**	**Formulation 8**
|Z| (kΩ)	1	58.5	108
	24	0.16	23
R_{pore} (kΩ)	1	-	180
	24	-	11.5
R_p (kΩ)	1	110	33
	24	0.2	16
C_c (F)	1	-	3.5×10^{-10}
	24	-	2.8×10^{-5}

Analysis of Nyquist and Bode plots (Figure 59) showed that for formulation 8, |Z| remained fairly uniform over the frequency range until higher frequencies were reached and a decline in |Z| was observed. Increasing the immersion time to 24 hours also saw the same trend in results, but with reduced |Z| values. The value of |Z| was observed at 108 kΩ for 1 hour of immersion, however with increased immersion up to 24 hours, |Z| reduced by ~ 80% to 23 kΩ. Phase angle remained near zero (~ -10 °) for the majority of the frequency range, before decreasing at the highest frequencies, suggesting capacitor impedance was becoming more dominant.

The values of |Z| recorded for formulation 1 were significantly smaller than those measured for formulation 8. After 1 hour of immersion, |Z| was recorded at 58.5 kΩ and reduced dramatically to 0.16 kΩ after 24 hours of immersion. During the initial immersion time, the phase angle values recorded at the lowest frequencies indicated that the overall circuit impedance was dominated by resistive elements. |Z| values recorded upon initial immersion were low in magnitude, suggesting that the coating may have inherent porosity. Additionally, values for C_c and C_{dl} for formulation 8 after 24 hours of immersion were shown to be 28 µF and 20 µF respectively. The values' similarity in magnitude, corroborated the theory of porosity being present within the coating and gave justification for choosing the embedded equivalent circuit diagram (Figure 60b) used for analysis. This porosity is commonly associated with this type of coating and supports the hypothesis made via initial SVET analysis that the porous coating film could have led to detrimental damage to the film.

The value of |Z| is likely to tend toward that of the resistance associated with the coating (R_{pore}), which was believed to originate from columns of electrolyte forming within the porous structure of the coating and allowing limited contact between the electrode and solution. For formulation 8, the reduction in R_{pore} observed was dramatic. R_{pore} reduced by ~ 90%, from 180 kΩ to 11.5 kΩ, between 1 and 24 hours of immersion. This demonstrated the coating's susceptibility to degradation when suspended in electrolyte for longer periods.

Conclusions can be drawn from the analysis of the impedance spectra of the coated samples immersed in 5% w.t. NaCl solution at room temperature. Key metrics displayed that formulation 1 had a higher susceptibility to corrosion in comparison to formulation 8. Further analysis of formulation 8 showed that with increased immersion time the corrosion resistance of the coating was dramatically reduced due to inherent porosity within the coating layer.

7.3.1.3 Humidity Testing

7.3.1.3.1 Method and Results

High humidity can cause failure of metal substrates, and thus high humidity environments are utilised to assess the real-life corrosion performance of a substrate. Conditions can be mimicked closely within laboratory settings using a humidity cabinet. Figure 61 (a-d) and Figure 62 (a-d) show photographs taken of uncoated and coated samples throughout humidity testing.

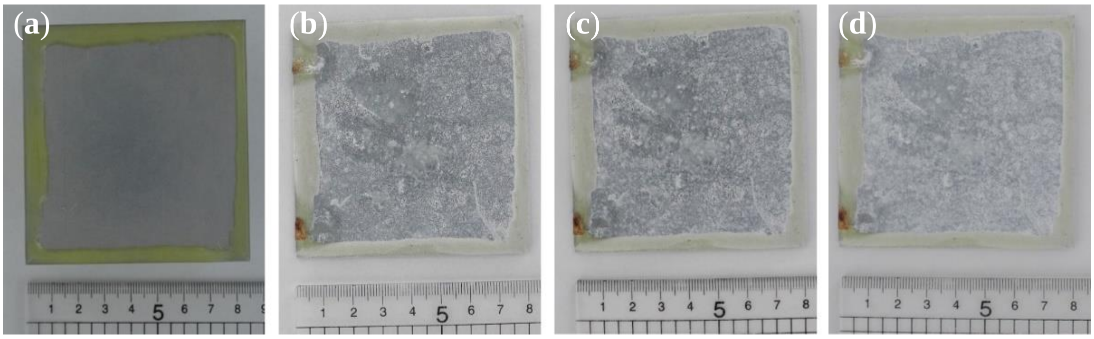

Figure 61. Humidity samples of uncoated HDG at (a) 0 h (b) 250 h (c) 500 h and (d) 1000 h.

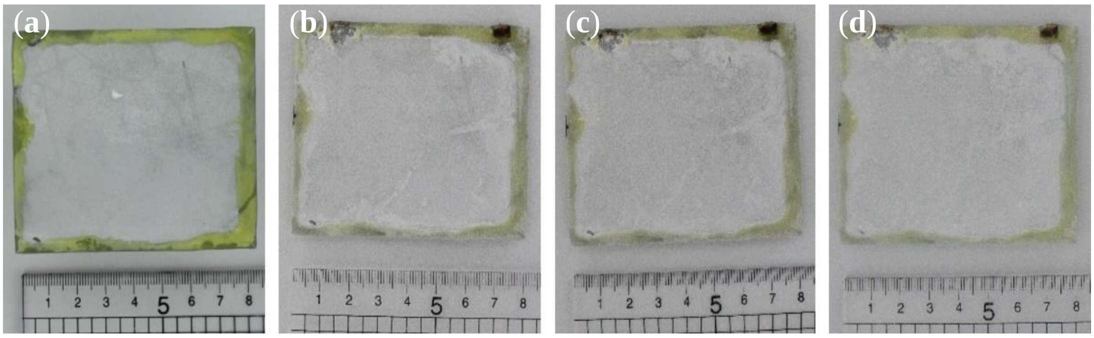

Figure 62. Humidity samples of coated HDG at (a) 0 h (b) 250 h (c) 500 h and (d) 1000 h.

Figure 63 demonstrates the increase in mass gained by both sample sets over this period. The uncoated sample visibly changes as a white precipitate is formed across the substrate surface. In contrast, the coating layer formed from zinc stearate and SiO_2 does not significantly change over the testing period. The mass change differences showcase the coated sample sees a significantly reduced mass increase and thus a higher corrosion resistance when compared with the uncoated sample.

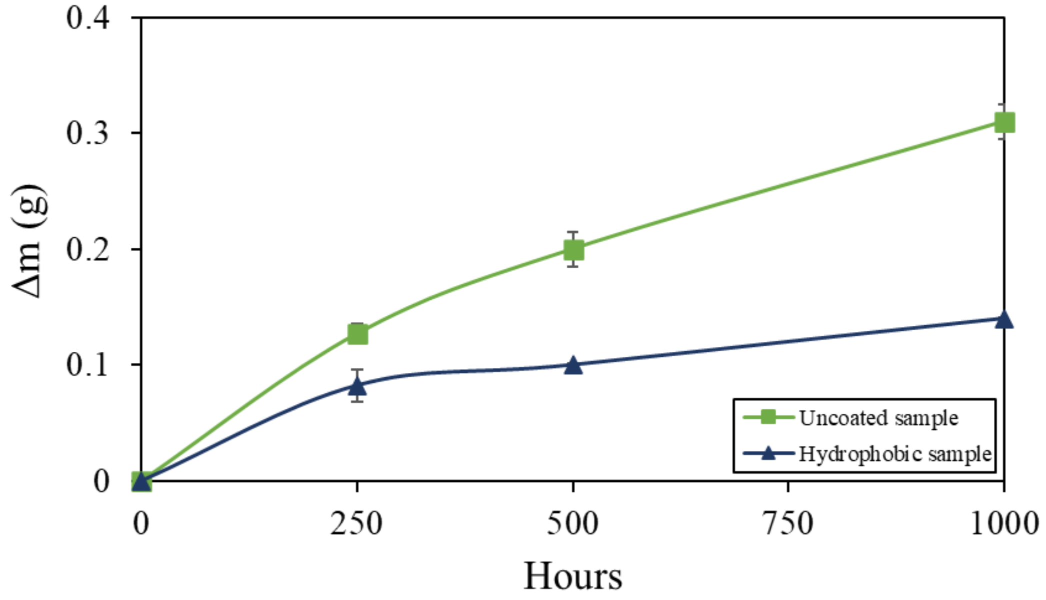

Figure 63. Mass gain of humidity samples over 1000 h displaying uncoated sample and hydrophobic sample.

7.3.1.4 XRD and FTIR Analysis of Humidity Results

Compositional analysis from XRD is given in Figure 64, which is used to determine the phase structure of the hydrophobic coating. A comparison is shown between the uncoated sample and the hydrophobic sample after 1000 h of humidity testing. By comparison, we observed that zinc stearate ($Zn(SA)_2$ where SA represents the stearate complex) is formed on the hydrophobic sample surface, and this signifies the reaction of zinc and stearic acid as shown in Equation (1). SiO_2 can also be seen in the XRD pattern, showcasing that SiO_2 has been encapsulated within the coating by physical action and not changing physical composition. The notable peak, which is observed in the uncoated sample and not the coated sample is that of zinc carbonate hydroxide and zinc hydroxide (88,100,175–177). This is created via the mechanisms:

$$5\,ZnO + 2\,CO_2 + 3\,H_2O = Zn_5(CO_3)_2(OH)_6 \quad (37)$$

$$Zn + 2\,H_2O = Zn(OH)_2 + 2\,H_2 \quad (38)$$

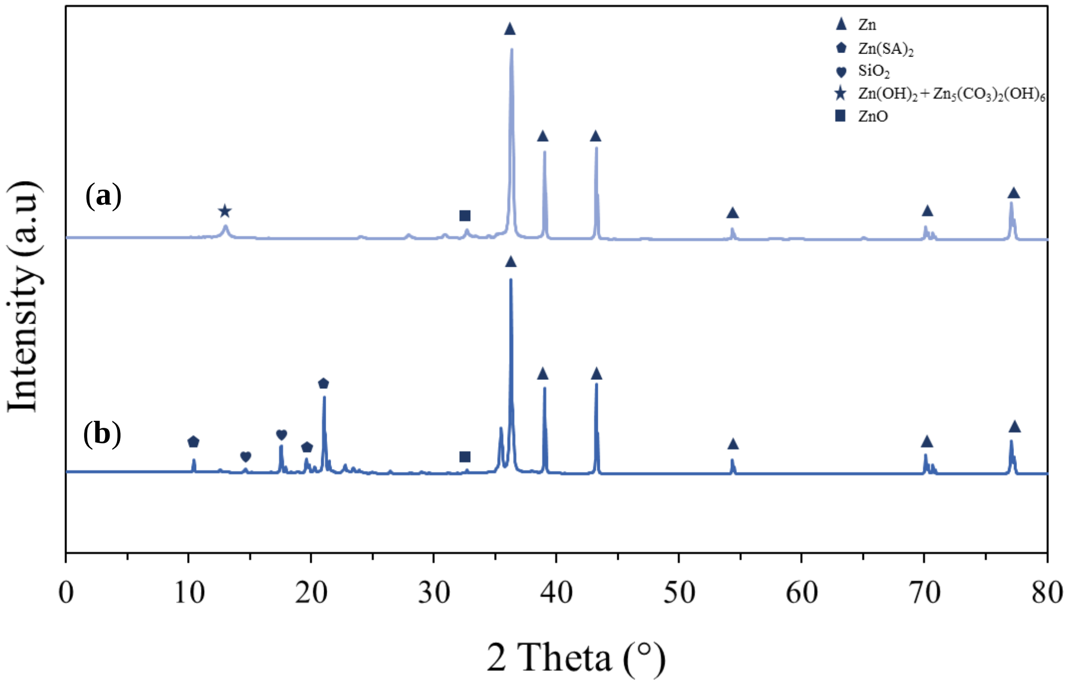

Figure 64. XRD patterns of humidity samples after 1000 h (a) uncoated sample and (b) hydrophobic sample.

FTIR analysis was completed alongside XRD to corroborate the observation of carbonate ($(CO_3)^{2-}$) bonds within the uncoated sample, this data is presented in Figure 65. This is highlighted by the peaks observed at 1500 and 1390 cm^{-1} relating to the antisymmetric stretching modes of $(CO_3)^{2-}$ (178).

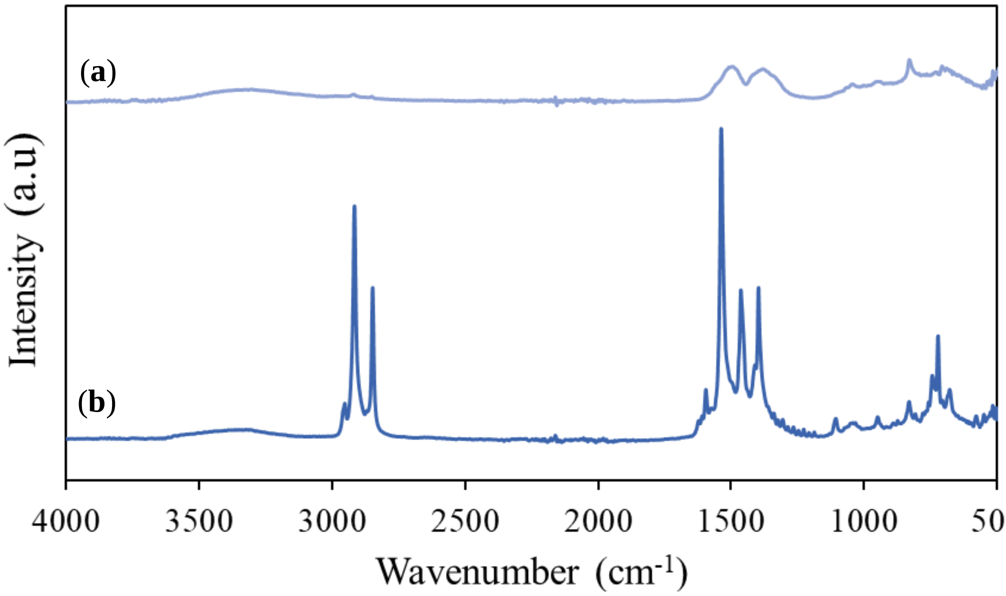

Figure 65. FTIR spectra of humidity samples after 1000 h: (a) uncoated surface and (b) hydrophobic surface.

This data provides validation that the white precipitate observed in Figure 62 can be mainly accounted to zinc carbonate hydroxide and zinc hydroxide formation on the surface. The mass change of both the uncoated and coated samples after humidity testing is assumed to be attributed to this and thus reinforces the theory that the coated sample has a higher resistance to corrosion due to a smaller change in mass.

7.3.2 Physical robustness

7.3.2.1 Formability

The formability of the coating is an important characteristic to assess for post-processing purposes. Having a greater understanding of how the coating behaves before, during, and after deformation will give a key indication of the coating’s suitability for industrial processing, post manufacturing. Complex geometries can be produced during forming processes, where the substrate is subjected to large amounts of strain (179). If the coating can demonstrate good hydrophobicity after deformation, it reduces the manufacturer's need to coat after the forming/stamping processes. In turn, reducing manufacturing time and overall costs, making it more industrially viable. The formability test investigated four different specimens at 0%, 5%, 15%, and 30% strain. The CA was measured at each, to assess the hydrophobicity. The results of the formability test are displayed in Figure 66.

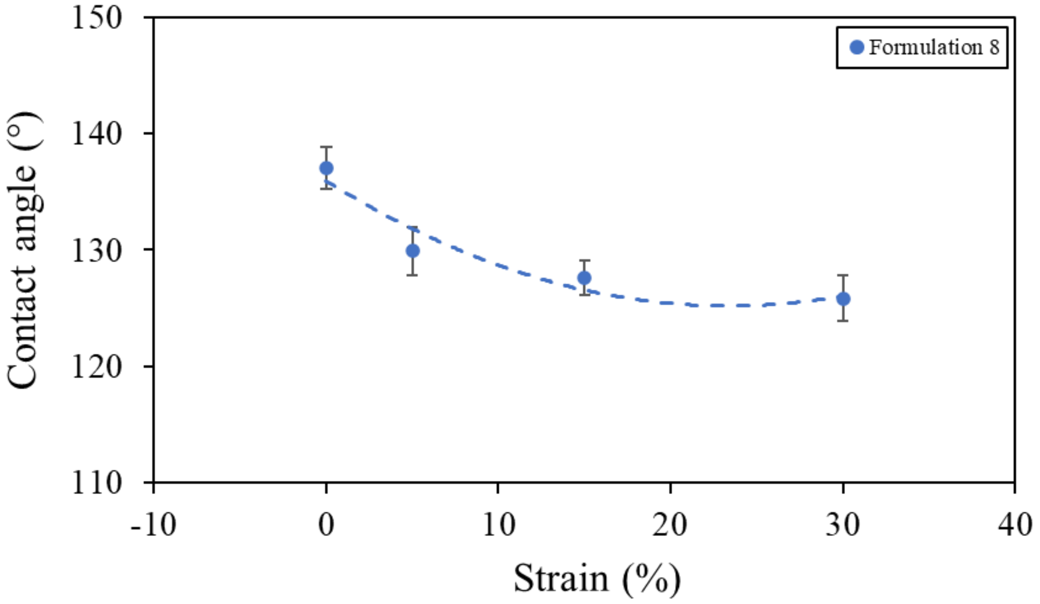

Figure 66. Graph displaying CA of the specimen with increased uniaxial strain.

There is a negative relationship between increased uniaxial strain and CA. Initially, CA drops by approximately 7° when strain goes from 0 - 5%. After this initial drop, CA decreases by 2° at 15% and 30% strain respectively, accumulating a 9° decrease at 15% strain and 11° for 30% strain. This relationship is depicted by the shape of the trendline shown between points on the graph. The hydrophobicity is seen to decrease steeply initially, before plateauing for higher strains. This suggests up until a certain deformation point the coating's hydrophobic performance is reduced, however, after this point there is negligible effect on hydrophobicity.

Through visual inspection, the strained specimens demonstrated no visible cracks or dislocation across the coating surface. Therefore, to understand why CA had decreased, SEM images were taken of the unstrained and strained surfaces at a 50µm scale. Studying the change in surface morphology at this scale indicates the potential factors that may contribute to the reduction in surface hydrophobicity. The SEM images for a specimen with no deformation and a specimen at max deformation (30% strain) can be observed in Figure 67. The area for imaging was selected by analysing the uniaxially strained area of the dog bone sample, in order to investigate the coating at its largest area of deformation.

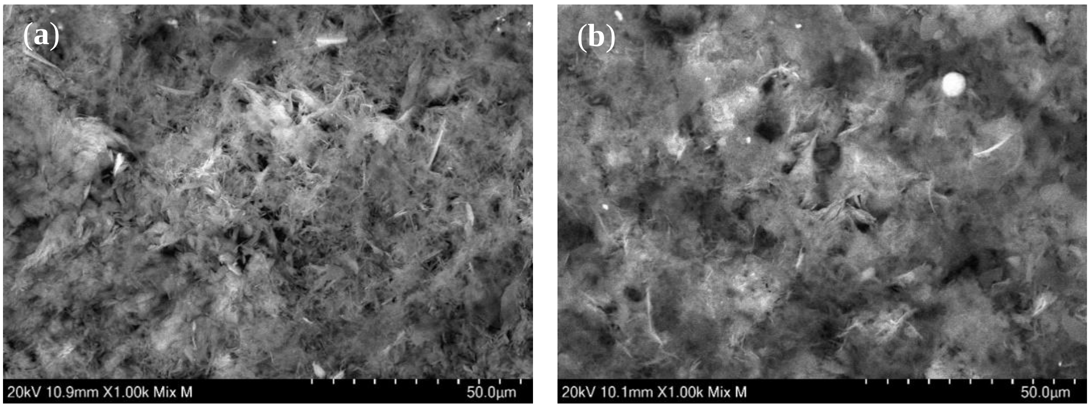

Figure 67. SEM images of zinc stearate coating: (a) no deformation and (b) 30% strain deformation.

Similar to previous images shown in Chapter 6, formulation 8 when unstrained displays a homogeneous coating of zinc stearate in needle-like structures that encapsulate floccules of SiO_2. Many small air pockets are created between these zinc stearate and SiO_2 molecules, which contribute to a rougher surface and as a result, increased surface hydrophobicity (88,164). The noticeable difference between the surface morphology of the unstrained and strained sample is the dark areas located in between the zinc stearate-SiO_2 coating in Figure 67 (b). These areas are identified as discontinuities in the coating morphology at the macro-scale and may explain why surface hydrophobicity is reduced. These dislocations reduce overall coating homogeneity and introduce less frequent air pockets within the coating, this, in turn, reduces the surface roughness, reducing overall surface hydrophobicity. Regardless of this, the two surface morphologies display similar structures and characteristics. This is not surprising as despite experiencing 30% strain, there is only a reduction in mean CA recorded by approximately 8%.

In conclusion, despite significant straining, formulation 8 still demonstrated significant surface hydrophobicity. This is positive for processing, and post-manufacturing and shows that the coating may have suitable formability properties for certain processes. However, to gain a greater overall picture of how formable the coating is, additional testing is required. This could include testing that utilises torsional forces to assess how the coating performs after bending.

7.3.2.2 Durability

Within industry, prepared hydrophobic coatings on substrates are vulnerable to abrasion damage. Their mechanical stability and durability can often be limiting factors when assessing their real-world viability (180). A specific novel test was carried out to provide information about the coatings' mechanical stability, durability, and performance after abrasion. As mentioned in section 7.2.2.4, a “pull-off” test was performed and targeted separate areas of the coated substrate. The contact angle was measured to assess coating performance against coating mass loss. The results of the durability test are displayed in Figure 68.

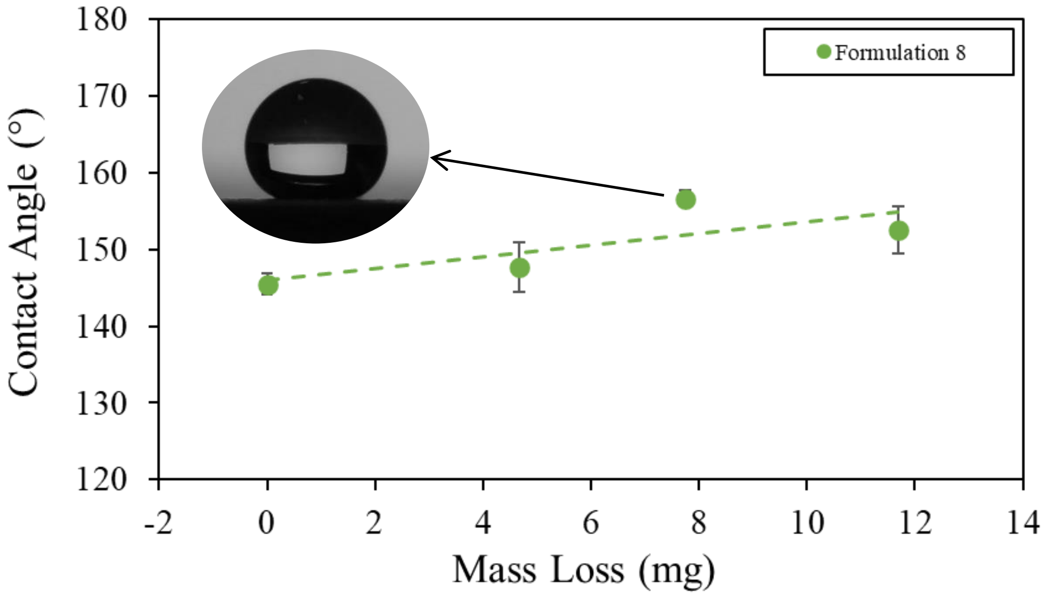

Figure 68. Graph displaying mean CA across sample against mass of coating removed after the pull-off test.

There are some significant results to discuss from this study. The overall trend in CA data shows a positive linear relationship between mass loss and hydrophobicity. It can be seen that up until 8mg is removed from the substrate surface, CA significantly improves, after this point CA begins to slightly decline with further coating removal. The CA data for the freshly coated substrate was recorded at 146°. After the first tape pull, approximately 4.5mg of coating mass was removed, and CA was seen to increase to 148°. The second tape pull removed a further 3.5mg of coating (~8mg total), and a large increase in CA was recorded at 158°. This large increase in surface hydrophobicity, with a CA over 150°, deems the surface superhydrophobic (88,181,182). On the third tape pull, a further 4mg was removed (~12mg total). A slight reduction in CA was recorded at 153°, with the surface remaining superhydrophobic.

The relationship between coating mass loss and CA showcases that when the top coating layers are removed, surface hydrophobicity can be significantly improved. It was hypothesised that this CA increase occurs due to the removal of excess SiO_2 deposited on the surface. It is hypothesised that the excess SiO_2 did not adhere to the substrate as part of the crystalline structure and instead blanketed itself over the surface. This layer contributed to reduced surface roughness, negated against the entrapment of air within rough surface features, and consequently reduced the overall surface hydrophobicity (161,162). As the tape pulls were performed during this investigation, deposited SiO_2 that blanketed the surface was able to be removed, exposing larger areas of the crystalline matrix below. This theory can be used to explain why the initial removal of coating mass (up to ~8mg) increased recorded surface hydrophobicity. After the excess SiO_2 was removed from the surface, the tape began to interfere with the integrity of the crystalline matrix of zinc stearate and SiO_2 (at ~12mg) and this may explain why CA was seen to slightly reduce at later stages in the investigation.

To corroborate this theory, it was important to analyse the coating material being removed and identify which components were being removed from the surface via the tape pull. Therefore, analysis of the coating mass removed by the tape was completed via SEM imaging equipped with EDX and shown in Figure 69.

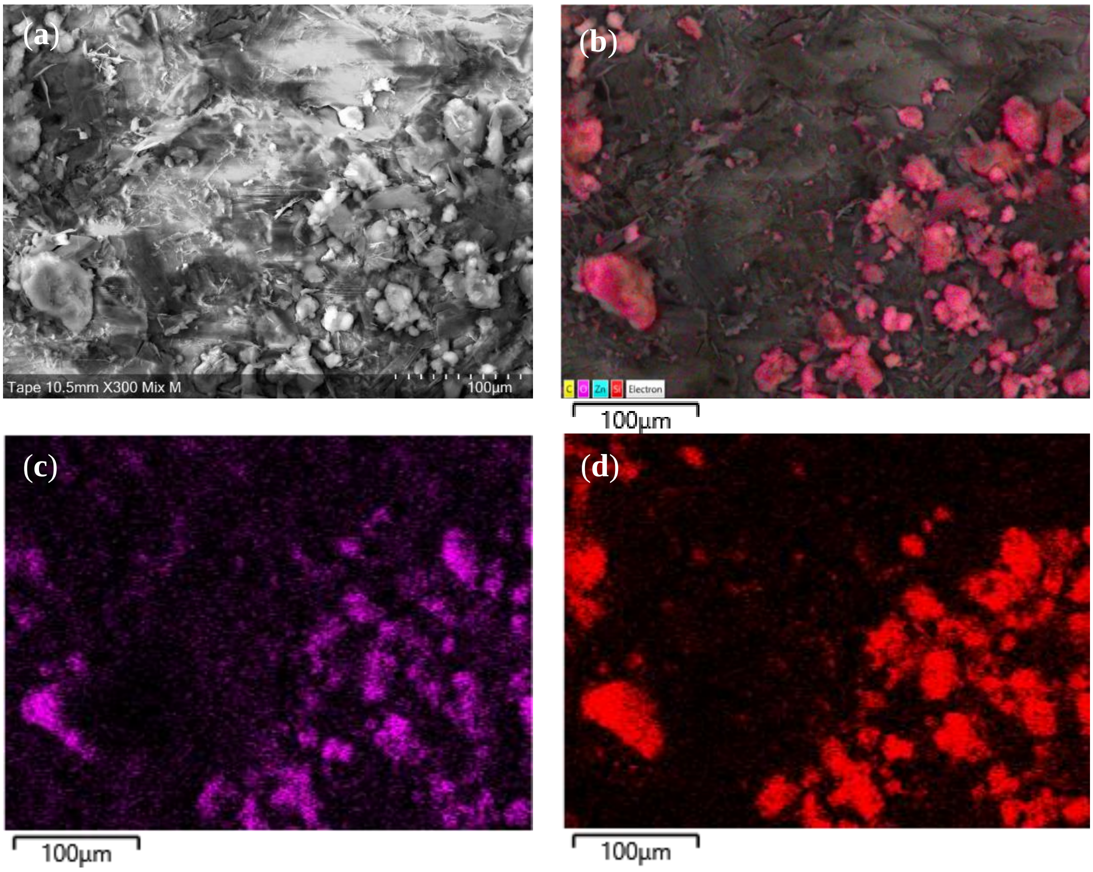

Figure 69. Surface imaging of removed coating mass on tape: (a) SEM image of tape and coating removed (b) layered EDX map of removed coating (c) element map for O (d) element map for Si.

Figure 69 (a) shows an SEM image of the tape after removing the coating, at 100µm scale. There are significant areas of flocculent material identified and this is assumed to be SiO_2, as it shares the same shape and structure as SiO_2 previously analysed. Figure 69 (b)-(c) validates this assumption via EDX. The layered EDX map illustrates that the main elements observed in the image are Si and O, with minimal counts recorded for elements C and Zn, which are associated with zinc stearate. The individual element maps for Si and O, show high intensity and confirm that the removed flocculent mass can be attributed to SiO_2.

7.4 Conclusions

This chapter has further studied the hydrophobic coating developed for hot-dipped galvanised steel from Chapter 6. Previously, processing times were drastically reduced but significant interest remained in further assessment of the coating's performance and its industrial viability. Additional mechanical tests and analytical techniques were necessary to accurately assess its industrial feasibility.

SVET was completed to quantitatively assess the corrosion resistance of the hydrophobic coating. SVET showed the hydrophobic coating delivered significant barrier properties to HDG steel. However, the hydrophobic coating can be susceptible to permeation if coating homogeneity/thickness is not consistent. Which can negatively impact the coating's resistance to corrosion through targeted anodic activity within pores. EIS data corroborated that of SVET and showed the corrosion resistance of formulation 8 to be superior to formulation 1 by demonstrating larger $|Z|$ and R_{pore} values and smaller capacitance values after 24 hours of immersion in 5% wt. NaCl solution. Despite this, with increased immersion time the corrosion resistance of both coatings was reduced due to inherent porosity within the coating layer. Under standard accelerated exposure tests, the uncoated samples were seen to increase in mass by approximately three times the amount of the coated samples, thus, inferring that considerable corrosion resistance was gained from the coating.

Novel physical robustness tests were completed to assess the formability and durability of the hydrophobic coating for industrial application. The formability of the coating was seen to be good, with only an 8% reduction in hydrophobic performance after 30% strain was induced. The novel durability test identified that excess SiO_2 was forming on top of the zinc stearate surface, removal of this excess layer saw an improvement in hydrophobicity by 8%, with a CA of 158° recorded. Sufficient evidence was provided to show the coating’s performance remained good even after significant abrasion and targeted coating removal.

8 Conclusions and future work

8.1 Conclusions

The research presented throughout this thesis had the main objectives of characterising, reviewing and evaluating current coatings employed by Tata Steel via their chemcoater system at their ZODIAC galvanising line in Llanwern and investigating the potential for novel coatings to add functionality and/or value to the hot-dipped galvanised steel substrate. A range of conclusions have been made, as outlined below.

The comparison between PrimeCoat and PLT coatings showed that they have very similar rheological characteristics, with PrimeCoat displaying a higher affinity to wetting to a HDG steel surface than PLT. PrimeCoat displayed a faster levelling out time on the HDG steel surface as the contact angle of the coating reduced over time significantly faster than PLT. Both coatings demonstrated very similar thermal stability behaviour with similar drying temperatures and energy requirements, and therefore it was hypothesised that there should be minimal issues when interchanging the coatings on an industrial line. Particular interest was paid towards understanding the tribological behaviour of both coatings with PLT in particular performing well as a dry film lubricant without the need for additional oiling.

A successful adaptation to a common laboratory polishing unit was carried out to create a novel Pin-on-Disk (POD) tribometer, which gave an effective and reliable method for measuring the dynamic coefficient of friction of a coated substrate over an extended period. The novel POD system was designed, built and commissioned in reference to ASTM G99-17 and provided a repeatable technique for measuring coefficient of friction. The adapted unit showed that reputable, accurate tribological results could be obtained within laboratory settings at a fraction of the cost of purchasing a purpose built, standard tribometer.

The use of sulphate-based treatments as functional coatings was shown to improve the frictional performance of zinc-coated steel substrates by reducing the coefficient of friction. Surface microscopy techniques and dynamic friction tests were conducted to compare the effects of different pH levels and solutes, such as ammonium sulphate, sodium sulphate and magnesium sulphate. Results showed that a neutral ammonium sulphate solution improved surface lubricity by 15% and 10% on HDG steel and ZM170 respectively, while sodium sulphate and magnesium sulphate had a negligible effect on ZM70. Even though the ZM70 substrate failed to see an improvement in frictional performance, it was hypothesised that coating thickness played a major role in the coating's efficiency. It was concluded that the use of ammonium and sodium sulphate treatments were deemed suitable for the coil coating procedure and could reduce the oil volume required, post-galvanising, in turn reducing overall costs.

A systematic study was conducted to improve the processability of a one-step hydrophobic coating for HDG steel. The variables studied included immersion time, the solvent used, the addition of NaOH, molarity and SiO2 particle size. The best-performing coating had a CA of 146° from an immersion time of 120 min, using IPA as the solvent, 2% wt. 1 M NaOH (aq), 0.2 M stearic acid and micro-SiO2 (0.2–0.3 µm). Compared to other one-step processes, this method has a significantly reduced processing time and fewer health and safety risks, while avoiding the use of toxic chemicals. Despite this, the process of creating hydrophobic coatings remains in hours, which makes it more suitable for batch processing rather than coil coating.

It was highlighted that; the hydrophobic coating could play an interesting role in post-production processes and was worthy of further study. Further investigations were completed to gain a better understanding of the coating's electrochemical and physical characteristics.

Corrosion analysis via SVET, EIS and Humidity testing identified that the coating provided good barrier properties to the HDG steel but could be prone to permeation if the coating was not consistent. Formulation 8 was shown to be superior to formulation 1. The physical robustness tests showed that the coating was formable and durable, with no significant reduction in hydrophobic performance after 30% strain was induced and no significant degradation in performance after abrasion. In conclusion, these results suggest that the coating could be a viable option for industrial applications.

8.2 Study limitations

Throughout this thesis, despite meticulous research conducted with concurrent execution and adherence to high standards, certain limitations became evident. Uncontrolled or unmeasured variables introduced variability in data acquisition, potentially influencing the precision of results. To mitigate these challenges, a methodical and statistically rigorous approach to data collection was implemented to ensure consistency and accuracy. Furthermore, the study's conduction within a bustling educational environment presented both advantages and drawbacks. The coexistence of numerous researchers and academics in the laboratory setting posed the risk of spatial congestion and equipment neglect. Therefore, strategic experiment planning and routine equipment maintenance were imperative to maintain optimal laboratory functionality and mitigate potential disruptions. Additionally, the changing research environment during and post the COVID-19 pandemic introduced great challenges. These shifts encompassed alterations in laboratory access and availability, disruptions in research schedules and timelines, and changes in safety protocols for all. These changes impacted the research workflow and posed potential hurdles to data collection, analysis, and the overall research process.

8.3 Future work

The POD tribometer should be utilised in future applications as an inexpensive and accurate method to measure a material’s dynamic frictional properties. The modular system means the tribometer can be easily assembled and configured to make quick and accurate tribometry readings for flat substrates. Some additional improvements to the system could include further dampening of the POD tribometer’s outer frame, interfering background noise can have an undesirable effect on the recorded values if not appropriately mitigated.

Further investigation should be paid to analysing the relationship between metallic coating thickness and its ability to form a suitable lubrication matrix with sulphate based-coatings for reduced coefficient of friction. The hypothesis that the coating thickness plays a significant role in the coating's efficiency provides interesting insight and should be further explored to understand the coating’s effectiveness for industrial application.

Further industrial evaluation techniques would be beneficial in estimating the real-world product lifetime extension provided by the zinc stearate coating. Additional mechanical tests and analytical techniques would be necessary to accurately assess its industrial feasibility, including relative abrasion resistance, frictional properties, adhesion and ductility. Industrial tests such as the pull-off strength of the coating membrane (ASTM D4541) and the mandrel bend test of attached organic coatings (ASTM D522) are examples of industrially recognised tests that could be used to further analyse the coating’s adhesion and ductility for practical application. Furthermore, it would be highly beneficial to analyse whether the hydrophobicity elicited from the zinc stearate coating has a negative effect on the substrate’s suitability for further coating, or if it is necessary for coating removal beforehand.

Attention should be paid to analysing the end-of-life process required once the coated product has reached obsolescence. Due to the chemical nature of both the sulphate-based and stearate-based coating, they contain relatively low hazardous materials. However, special attention should be placed on recyclability and whether post-processing, such as alkaline cleaning, is necessary to negate negative environmental effects.

9 Bibliography

1. Chatterjee B. Chatterjee : Hot Dip Galvanizing Chatterjee : Hot Dip Galvanizing Hot Dip Galvanizing. 2017;(January 2014).
2. Duarte RG, Bastos AC, Castela AS, Ferreira MGS. A comparative study between Cr(VI)-containing and Cr-free films for coil coating systems. Prog Org Coatings [Internet]. 2005 Apr 1 [cited 2019 Mar 4];52(4):320–7. Available from: https://www.sciencedirect.com/science/article/pii/S0300944004002243
3. HSE. EIS 32 - Chromate primer paints. (32).
4. Di Schino A. Environmental Impact of Steel Industry. Handb Environ Mater Manag [Internet]. 2019 [cited 2022 Jun 13];2463–83. Available from: https://link.springer.com/referenceworkentry/10.1007/978-3-319-73645-7_101
5. Long Y, Liu C, Peng S. Enhanced performance of a green inorganic-based passive film on the batch hot-dip galvanized steel by organic additives. Int J Electrochem Sci. 2020;15(3):2568–80.
6. Carneiro E, Castro JD, Marques SM, Cavaleiro A, Carvalho S. REACH regulation challenge: Development of alternative coatings to hexavalent chromium for minting applications. Surf Coatings Technol. 2021 Jul 25;418.
7. Coyle DJ. Knife and Roll Coating. In: Liquid Film Coating [Internet]. Dordrecht: Springer Netherlands; 1997 [cited 2019 Mar 25]. p. 539–71. Available from: http://link.springer.com/10.1007/978-94-011-5342-3_15
8. Fedrizzi L, Ciaghi L, Bonora PL, Fratesi R, Roventi G. Corrosion behaviour of electrogalvanized steel in sodium chloride and ammonium sulphate solutions; a study by E.I.S. J Appl Electrochem. 1992;22(3):247–54.
9. Almeida E, Diamantino T., Figueiredo M., Sá C. Oxidising alternative species to chromium VI in zinc galvanised steel surface treatment. Part 1—A morphological and chemical study. Surf Coatings Technol [Internet]. 1998 Jul 10 [cited 2019 Apr 17];106(1):8–17. Available from: https://www.sciencedirect.com/science/article/pii/S0257897298004642
10. Zarras P, Stenger-smith JD. Smart Inorganic and Organic Pretreatment Coatings for the Inhibition of Corrosion on Metals/Alloys. In: Intelligent Coatings for Corrosion Control [Internet]. p. 59–91. Available from: http://dx.doi.org/10.1016/B978-0-12-411467-8.00003-9
11. Berger R, Bexell U, Mikael Grehk T, Hörnström SE. A comparative study of the corrosion protective properties of chromium and chromium free passivation methods. Surf Coatings Technol. 2007;202(2):391–7.
12. Verma C, Ebenso EE, Quraishi MA. Corrosion inhibitors for ferrous and non-ferrous metals and alloys in ionic sodium chloride solutions: A review. J Mol Liq [Internet]. 2017;248:927–42. Available from: https://doi.org/10.1016/j.molliq.2017.10.094
13. Saikia, SK, Mishra AK, Tiwari S, Pandey R. Hexavalent Chromium Induced Histological Alterations in Bacopa monnieri (L.) and Assessment of Genetic

Variance. J Cytol Histol. 2012;03(02).

14. Tata. Strip products and services catalogue 2018. 2018;

15. Cook TH. Designing a general/pipes hot dip galvanizing plant. Met Finish. 1991;89(5).

16. Cook TH. Composition, Testing, Dip Galvanizing Flux. Met Finish. 2003;101(7–8):22–35.

17. Persson D, Thierry D, Karlsson O. Corrosion and corrosion products of hot dipped galvanized steel during long term atmospheric exposure at different sites world-wide. Corros Sci [Internet]. 2017 Sep 1 [cited 2019 May 21];126:152–65. Available from: https://www.sciencedirect.com/science/article/pii/S0010938X1631469X

18. Smith WJ, Goodwin FE. Hot Dip Coatings. Ref Modul Mater Sci Mater Eng [Internet]. 2017 Jan 1 [cited 2019 May 21]; Available from: https://www.sciencedirect.com/science/article/pii/B9780128035818092146

19. Kuklík V, Kudláček J, Kuklík V, Kudláček J. 2 – Hot-dip galvanizing. In: Hot-Dip Galvanizing of Steel Structures. 2016. p. 7–16.

20. ISO. Corrosion of metals and alloys - basic terms and definitions [Internet]. Vol. 8044, ISO. 2015. Available from: https://www.iso.org/obp/ui/#iso:std:iso:8044:ed-4:v1:en

21. Amirudin A, Thierry D. Corrosion mechanisms of phosphated zinc layers on steel as substrates for automotive coatings. Prog Org Coatings [Internet]. 1996 May 1 [cited 2019 May 22];28(1):59–75. Available from: https://www.sciencedirect.com/science/article/pii/0300944095005544

22. Edavan RP, Kopinski R. Corrosion resistance of painted zinc alloy coated steels. Corros Sci. 2009;51(10):2429–42.

23. Singh R, Singh R. Coating for Corrosion Prevention. Corros Control Offshore Struct [Internet]. 2014 Jan 1 [cited 2019 Apr 26];115–29. Available from: https://www.sciencedirect.com/science/article/pii/B9780124046153000085

24. Manoj Kumar Chaudhury, A. V. Pocius and DAD. Adhesion Science and Engineering: Surfaces, Chemistry and Applications. Elsevier Science & Technology; 2002. 303–343 p.

25. The Chemistry and Physics of Coatings. The Chemistry and Physics of Coatings. Royal Society of Chemistry; 2008.

26. Arthur A. Tracton, editor. Coatings Technology. Coatings Technology. CRC Press; 2010.

27. Boger D V. An Introduction to Rheology. J Nonnewton Fluid Mech. 1989;

28. Chandran N, Sarathchandran C, Thomas S. Introduction to rheology [Internet]. Rheology of Polymer Blends and Nanocomposites: Theory, Modelling and Applications. Elsevier Inc.; 2019. 1–17 p. Available from: http://dx.doi.org/10.1016/B978-0-12-816957-5.00001-X

29. Eugene C. Bingham. An investigation of the laws of plastic flow / by Eugene C. Bingham. In National Bureau of Standards; 1916. p. 309–53.

30. Weidner DE, Schwartz LW, Eley RR. Role of surface tension gradients in

correcting coating defects in corners. J Colloid Interface Sci. 1996 Apr 15;179(1):66–75.

31. Gao L, McCarthy TJ, Zhang X. Wetting and Superhydrophobicity. Langmuir. 2009;25(24):14100–4.

32. Mittal KL. Advances in Contact Angle, Wettability and Adhesion, Volume 3. John Wiley & Sons, Incorporated; 2018. 428 p.

33. Mittal KL. The role of the interface in adhesion phenomena. Polym Eng Sci. 1977;17(7):467–73.

34. Jokar M, Aliofkhazraei M. 3.20 Surface Preparation and Adhesion Tests of Coatings. Compr Mater Finish [Internet]. 2017 Jan 1 [cited 2019 Apr 17];306–35. Available from: https://www.sciencedirect.com/science/article/pii/B9780128035818092018

35. Vayeda R, Wang J. Adhesion of coatings to sheet metal under plastic deformation. Int J Adhes Adhes. 2007;27(6):480–92.

36. Xie Y, Hawthorne HM. Effect of contact geometry on the failure modes of thin coatings in the scratch adhesion test. Surf Coatings Technol. 2002;155(2–3):121–9.

37. Weldon DG. Failure Analysis of Paints and Coatings: Revised Edition. Fail Anal Paint Coatings Revis Ed. 2009;1–362.

38. McKeen LW, McKeen LW. Application of Liquid Coatings. Fluorinated Coatings Finish Handb [Internet]. 2016 Jan 1 [cited 2019 Apr 17];171–83. Available from: https://www.sciencedirect.com/science/article/pii/B9780323371261000102

39. Drufke R. An introduction to coil coating: Finishing process leads to consistent quality and appearance in metal parts. Met Finish [Internet]. 2006 Apr 1 [cited 2019 May 7];104(4):35–7. Available from: https://www.sciencedirect.com/science/article/pii/S0026057606800942

40. Bahadori A, Bahadori A. Chapter 2 – Engineering and Technical Guidelines for Painting. In: Essentials of Coating, Painting, and Lining for the Oil, Gas and Petrochemical Industries. 2015. p. 107–56.

41. Bahadori A, Bahadori A. Surface Preparation for Coating, Painting, and Lining. Essentials Coating, Paint Lining Oil, Gas Petrochemical Ind [Internet]. 2015 Jan 1 [cited 2019 May 20];1–105. Available from: https://www.sciencedirect.com/science/article/pii/B9780128014073000018

42. Bibber J. An overview of nonhexavalent chromium conversion coatings—Part II: Zinc. Met Finish [Internet]. 2002 Feb 1 [cited 2019 Apr 17];100(2):98–102. Available from: https://www.sciencedirect.com/science/article/pii/S0026057602801623

43. Graziano F. Coil and sheet coating. Met Finish [Internet]. 1999 Jan 1 [cited 2019 May 7];97(5):186–90. Available from: https://www.sciencedirect.com/science/article/pii/S002605769980779X

44. Szczurek E, Dubar M, Deltombe R, Dubois A, DUBAR L. New approach to the evaluation of the free surface position in roll coating. J Mater Process

Technol [Internet]. 2009 Apr 1 [cited 2019 Mar 5];209(7):3187–97. Available from: https://www.sciencedirect.com/science/article/pii/S0924013608005864

45. Eckermann J. Optimising high speed coating processes [Internet]. Swansea University; 2012. Available from: file:///C:/Users/Jamie/AppData/Local/Packages/Microsoft.MicrosoftEdge_8wekyb3d8bbwe/TempState/Downloads/10798179 (1).pdf
46. Alonso S, Réglat O, Bertrand F, Choplin L, Tanguy PA. Process Viscosity in Reverse Roll Coating. Chem Eng Res Des [Internet]. 2001 Mar 1 [cited 2019 May 15];79(2):128–36. Available from: https://www.sciencedirect.com/science/article/pii/S0263876201720278
47. Coyle DJ, Macosko CW, Scriven LE. A Simple Model of Reverse Roll Coating. Ind Eng Chem Res. 1990 Jul 1;29(7):1416–9.
48. Koschmieder EL, Biggerstaff MI. Onset of surface-tension-driven bénard convection. J Fluid Mech. 1986;167:49–64.
49. Lee IJ, Park S, Noh SM, Jung HW, Park JM. Rheology and roll coating dynamics of metallic basecoats for automotive pre-coated metal sheet. Prog Org Coatings. 2013;76(5):917–23.
50. Gutoff EB, Cohen ED. Water- and Solvent-Based Coating Technology. Multilayer Flex Packag [Internet]. 2016 Jan 1 [cited 2019 May 9];205–34. Available from: https://www.sciencedirect.com/science/article/pii/B9780323371001000144
51. Carvalho M., Scriven L. Three-Dimensional Stability Analysis of Free Surface Flows: Application to Forward Deformable Roll Coating. J Comput Phys [Internet]. 1999 May 20 [cited 2019 Mar 5];151(2):534–62. Available from: https://www.sciencedirect.com/science/article/pii/S0021999199961958
52. Gostling MJ. Stability of rigid and deformable roll coating flows. Astronomy. The University of Leeds; 2001.
53. Technologies P. Engineering Documentation - Vertical Strip Coating for ZODIAC Line (Operation and Maintenance). p. 1–55.
54. Bibber JW. Non-chrome-containing conversion coatings for zinc and zinc alloys: Environmentally friendly alternatives provide equal or better adhesion and corrosion resistance as conventional methods. Met Finish. 2008;106(4):41–6.
55. Eppensteiner FW, Jennkind MR. Chromate conversion coatings. Met Finish [Internet]. 2007 Jan 1 [cited 2019 May 20];105(10):413–24. Available from: https://www.sciencedirect.com/science/article/pii/S0026057607803606?via%3Dihub
56. Gao Z, Zhang D, Li X, Jiang S, Zhang Q. Current status, opportunities and challenges in chemical conversion coatings for zinc. Colloids Surfaces A Physicochem Eng Asp. 2018;546:221–36.
57. DesMarais TL, Costa M. Mechanisms of Chromium-Induced Toxicity. Curr Opin Toxicol [Internet]. 2019 May 17 [cited 2019 May 21]; Available from: https://www.sciencedirect.com/science/article/pii/S2468202019300294

58. Tsai C-Y, Liu J-S, Chen P-L, Lin C-S. A roll coating tungstate passivation treatment for hot-dip galvanized sheet steel. Surf Coatings Technol [Internet]. 2011 Aug 25 [cited 2019 Mar 4];205(21–22):5124–9. Available from: https://www.sciencedirect.com/science/article/pii/S0257897211005251
59. Kuehner MA. Phosphate Conversion Coatings. Met Finish. 1985;83(8):15–8.
60. Narayanan TSNS. Surface pretreatment by phosphate conversion coatings - A review. Rev Adv Mater Sci. 2005;9(2):130–77.
61. Rezaee N, Attar MM, Ramezanzadeh B. Studying corrosion performance, microstructure and adhesion properties of a room temperature zinc phosphate conversion coating containing Mn2+ on mild steel. Vol. 236, Surface and Coatings Technology. 2013. p. 361–7.
62. Amin MA. Passivity and passivity breakdown of a zinc electrode in aerated neutral sodium nitrate solutions. Electrochim Acta [Internet]. 2005 Jan 30 [cited 2019 May 23];50(6):1265–74. Available from: https://www.sciencedirect.com/science/article/pii/S0013468604008953
63. Magalhães AAO, Margarit ICP, Mattos OR. Molybdate conversion coatings on zinc surfaces. J Electroanal Chem [Internet]. 2004 Nov 1 [cited 2019 May 23];572(2):433–40. Available from: https://www.sciencedirect.com/science/article/pii/S0022072804003948
64. Tsai C-Y, Liu J-S, Chen P-L, Lin C-S. A two-step roll coating phosphate/molybdate passivation treatment for hot-dip galvanized steel sheet. Corros Sci [Internet]. 2010 Oct 1 [cited 2019 Mar 4];52(10):3385–93. Available from: https://www.sciencedirect.com/science/article/pii/S0010938X10003276
65. Song YK, Mansfeld F. Development of a Molybdate–Phosphate–Silane–Silicate (MPSS) coating process for electrogalvanized steel. Corros Sci [Internet]. 2006 Jan 1 [cited 2019 May 23];48(1):154–64. Available from: https://www.sciencedirect.com/science/article/pii/S0010938X05000120
66. Buchheit RG, Guan H, Mahajanam S, Wong F. Active corrosion protection and corrosion sensing in chromate-free organic coatings. Prog Org Coatings [Internet]. 2003 Sep 1 [cited 2019 May 23];47(3–4):174–82. Available from: https://www.sciencedirect.com/science/article/pii/S0300944003001735
67. Zou Z, Li N, Li D, Liu H, Mu S. A vanadium-based conversion coating as chromate replacement for electrogalvanized steel substrates. J Alloys Compd [Internet]. 2011 Jan 12 [cited 2019 May 23];509(2):503–7. Available from: https://www.sciencedirect.com/science/article/pii/S0925838810023078
68. Zaferani SH, Peikari M, Zaarei D, Danaee I, Fakhraei JM, Mohammadi M. Using silane films to produce an alternative for chromate conversion coatings. Corrosion. 2013;
69. Calabrese L, Proverbio E. Special issue “recent developments on functional coatings for industrial applications.” Coatings. 2020;10(11):1–3.
70. Bacela J, Łabowska MB, Detyna J, Ziety A, Michalak I. Functional coatings for orthodontic archwires-A review. Materials (Basel). 2020;13(15).
71. Salaoru I, Maswoud S, Paul S. Inkjet printing of functional electronic memory cells: A step forward to green electronics. Micromachines. 2019;10(6):1–10.

72. Calabrese L, Brancato V, Bonaccorsi L, Frazzica A, Caprì A, Freni A, et al. Development and characterization of silane-zeolite adsorbent coatings for adsorption heat pump applications. Appl Therm Eng [Internet]. 2017;116:364–71. Available from: http://dx.doi.org/10.1016/j.applthermaleng.2017.01.112

73. Ulaeto SB, Rajan R, Pancrecious JK, Rajan TPD, Pai BC. Developments in smart anticorrosive coatings with multifunctional characteristics. Prog Org Coatings [Internet]. 2017 Oct 1 [cited 2019 May 29];111:294–314. Available from: https://www.sciencedirect.com/science/article/pii/S0300944016310839

74. Hosseini M, Hamdy Makhlouf AS. Industrial applications for intelligent polymers and coatings. Ind Appl Intell Polym Coatings. 2016;1–710.

75. Balgude D, Sabnis A. Sol-gel derived hybrid coatings as an environment friendly surface treatment for corrosion protection of metals and their alloys. J Sol-Gel Sci Technol. 2012;64(1):124–34.

76. Wang D, Bierwagen GP. Sol-gel coatings on metals for corrosion protection. Prog Org Coatings. 2009;64(4):327–38.

77. Bhushan B, Israelachvili JN, Landman U. Nanotribology: Friction, wear and lubrication at the atomic scale. Nature. 1995;374(6523):607–16.

78. Meiler M, Pfestorf M, Geiger M, Merklein M. The use of dry film lubricants in aluminum sheet metal forming. Wear. 2003;

79. Rosenkranz A, Costa HL, Baykara MZ, Martini A. Synergetic effects of surface texturing and solid lubricants to tailor friction and wear – A review [Internet]. Vol. 155, Tribology International. 2021 [cited 2022 Oct 13]. p. 106792. Available from: https://doi.org/10.1016/j.triboint.2020.106792

80. Dubois A, Karim ANM. Metal Forming and Lubrication. Ref Modul Mater Sci Mater Eng. 2019;(i).

81. Persson BNJ. Sliding friction. Surf Sci Rep. 1999;33(3):83–119.

82. Holmberg K, Matthews A, Ronkainen H. Coatings tribology - Contact mechanisms and surface design. Tribol Int. 1998;31(1–3):107–20.

83. Holmberg K, Ronkainen H, Matthews A. Tribology of thin coatings. Ceram Int. 2000;26(7):787–95.

84. Lovell M, Higgs CF, Deshmukh P, Mobley A. Increasing formability in sheet metal stamping operations using environmentally friendly lubricants. J Mater Process Technol. 2006 Jul 3;177(1–3):87–90.

85. Timma C, Lostak T, Janssen S, Flock J, Mayer C. Surface investigation and tribological mechanism of a sulfate-based lubricant deposited on zinc-coated steel sheets. Appl Surf Sci. 2016;390:784–94.

86. Vazirinasab E, Jafari R, Momen G. Application of superhydrophobic coatings as a corrosion barrier: A review. Surf Coatings Technol. 2018;341(July 2017):40–56.

87. Zhang F, Ju P, Pan M, Zhang D, Huang Y, Li G, et al. Self-healing mechanisms in smart protective coatings: A review. Corros Sci. 2018;144(August):74–88.

88. Liang T, Yuan H, Li C, Dong S, Zhang C, Cao G, et al. Corrosion inhibition effect of nano–SiO2 for galvanized steel superhydrophobic surface. Surf

Coatings Technol. 2021;406(October 2020).

89. Latthe SS, Sudhagar P, Devadoss A, Kumar AM, Liu S, Terashima C, et al. A mechanically bendable superhydrophobic steel surface with self-cleaning and corrosion-resistant properties. J Mater Chem A. 2015;3(27):14263–71.

90. Boinovich LB, Gnedenkov S V., Alpysbaeva DA, Egorkin VS, Emelyanenko AM, Sinebryukhov SL, et al. Corrosion resistance of composite coatings on low-carbon steel containing hydrophobic and superhydrophobic layers in combination with oxide sublayers. Corros Sci. 2012;55:238–45.

91. Liu Y, Li S, Zhang J, Liu J, Han Z, Ren L. Corrosion inhibition of biomimetic super-hydrophobic electrodeposition coatings on copper substrate. Corros Sci. 2015;94:190–6.

92. Yin B, Fang L, Hu J, Tang AQ, Wei WH, He J. Preparation and properties of super-hydrophobic coating on magnesium alloy. Appl Surf Sci. 2010;257(5):1666–71.

93. Brassard JD, Sarkar DK, Perron J, Audibert-Hayet A, Melot D. Nano-micro structured superhydrophobic zinc coating on steel for prevention of corrosion and ice adhesion. J Colloid Interface Sci. 2014;447:240–7.

94. Qian B, Shen Z. Fabrication of superhydrophobic surfaces by dislocation-selective chemical etching on aluminum, copper, and zinc substrates. Langmuir. 2005;21(20):9007–9.

95. Zhang X, Liang J, Liu B, Peng Z. Preparation of superhydrophobic zinc coating for corrosion protection. Colloids Surfaces A Physicochem Eng Asp. 2014;454(1):113–8.

96. Xu W, Ning T, Yang X, Lu S. Fabrication of superhydrophobic surfaces on zinc substrates. Appl Surf Sci. 2011;257(11):4801–6.

97. Naing TH, Rachpech V, Janudom S, Mahathaninwong N. Characterization of water-repellent and corrosion-resistant superhydrophobic surfaces on galvanized steel. J Coatings Technol Res. 2020;17(6):1537–48.

98. Barati Darband G, Aliofkhazraei M, Khorsand S, Sokhanvar S, Kaboli A. Science and Engineering of Superhydrophobic Surfaces: Review of Corrosion Resistance, Chemical and Mechanical Stability. Arab J Chem. 2020;13(1):1763–802.

99. Montemor MF. Functional and smart coatings for corrosion protection: A review of recent advances. Surf Coatings Technol. 2014;258:17–37.

100. Li C, Ma R, Du A, Fan Y, Zhao X, Cao X. Superhydrophobic film on hot-dip Galvanized steel with corrosion resistance and self-cleaning properties. Metals (Basel). 2018;8(9).

101. Zhang XF, Chen RJ, Hu JM. Superhydrophobic surface constructed on electrodeposited silica films by two-step method for corrosion protection of mild steel. Corros Sci. 2016;104:336–43.

102. Barthlott W, Neinhuis C. Purity of the sacred lotus, or escape from contamination in biological surfaces. Planta. 1997;202(1):1–8.

103. Fürstner R, Barthlott W, Neinhuis C, Walzel P. Wetting and self-cleaning

properties of artificial superhydrophobic surfaces. Langmuir. 2005;21(3):956–61.

104. Bahgat Radwan A, Abdullah AM, Alnuaimi NA. Recent advances in corrosion resistant superhydrophobic coatings. Corros Rev. 2018;36(2):127–53.

105. Hao Y, Soolaman DM, Yu HZ. Controlled wetting on electrodeposited oxide thin films: From hydrophilic to superhydrophobic. J Phys Chem C. 2013;117(15):7736–43.

106. Liu Q, Chen D, Kang Z. One-Step electrodeposition process to fabricate corrosion-resistant superhydrophobic surface on magnesium alloy. ACS Appl Mater Interfaces. 2015;7(3):1859–67.

107. Varshney P, Mohapatra SS, Kumar A. Superhydrophobic coatings for aluminium surfaces synthesized by chemical etching process. Int J Smart Nano Mater. 2016;7(4):248–64.

108. Jurak SF, Jurak EF, Uddin MN, Asmatulu R. Functional superhydrophobic coating systems for possible corrosion mitigation. Int J Autom Technol. 2020;14(2):148–58.

109. Li C, Ma R, Du A, Fan Y, Zhao X, Cao X. One-step fabrication of bionic superhydrophobic coating on galvanised steel with excellent corrosion resistance. J Alloys Compd. 2019;786:272–83.

110. Chen Z, Hao L, Chen A, Song Q, Chen C. A rapid one-step process for fabrication of superhydrophobic surface by electrodeposition method. Electrochim Acta. 2012;59:168–71.

111. Knudsen OO, Forsgren A. Corrosion Control Through Organic Coatings. Second. CRC Press; 2017.

112. Steffi AP, Balaji R, Chen SM, Prakash N, Narendhar C. Rational Construction of SiO2/MoS2/TiO2 Composite Nanostructures for Anti-Biofouling and Anti-Corrosion Applications. ChemistrySelect. 2021;6(5):917–27.

113. Liu Y, Zhang S, He Y, Chen C, Zhang C, Xie P, et al. Aptes modification of molybdenum disulfide to improve the corrosion resistance of waterborne epoxy coating. Coatings. 2021;11(2):1–13.

114. Rodríguez Ripoll M, Tomala AM, Totolin V, Remškar M. Performance of nanolubricants containing MoS 2 nanotubes during form tapping of zinc-coated automotive components. J Manuf Process [Internet]. 2019;39(February):167–80. Available from: https://doi.org/10.1016/j.jmapro.2019.02.012

115. Guo F, Aryana S, Han Y, Jiao Y. A review of the synthesis and applications of polymer-nanoclay composites. Appl Sci. 2018;8(9):1–29.

116. Müller K, Bugnicourt E, Latorre M, Jorda M, Sanz YE, Lagaron JM, et al. Review on the processing and properties of polymer nanocomposites and nanocoatings and their applications in the packaging, automotive and solar energy fields. Nanomaterials. 2017;7(4).

117. Vickerman JC, Gilmore IS. Surface Analysis - The Principal Techniques: Second Edition. Surface Analysis - The Principal Techniques: Second Edition. 2009.

118. Peißker P. Surface-Preparation Technology. In: Handbook of Hot-Dip Galvanization. John Wiley & Sons, Ltd; 2011. p. 29–90.

119. Yang Leng. Materials Characterization : Introduction to Microscopic and Spectroscopic Methods [Internet]. Second Edi. John Wiley & Sons, Incorporated; 2013. Available from: https://ebookcentral.proquest.com/lib/swansea-ebooks/reader.action?docID=1333091

120. Glaeser WA. Characterization of Tribological Materials, Second Edition. Characterization of Tribological Materials, Second Edition. 2012.

121. Titus D, James Jebaseelan Samuel E, Roopan SM. Nanoparticle characterization techniques [Internet]. Green Synthesis, Characterization and Applications of Nanoparticles. Elsevier Inc.; 2019. 303–319 p. Available from: https://doi.org/10.1016/B978-0-08-102579-6.00012-5

122. Gumustas M, Sengel-Turk CT, Gumustas A, Ozkan SA, Uslu B. Effect of Polymer-Based Nanoparticles on the Assay of Antimicrobial Drug Delivery Systems [Internet]. Multifunctional Systems for Combined Delivery, Biosensing and Diagnostics. Elsevier Inc.; 2017. 67–108 p. Available from: http://dx.doi.org/10.1016/B978-0-323-52725-5/00005-8

123. Sherwood PMA. Carbons and Graphites: Surface Properties of. Encycl Mater Sci Technol. 2001;985–95.

124. Ebnesajjad S. Handbook of Adhesives and Surface Preparation [Internet]. Handbook of Adhesives and Surface Preparation. 2011 [cited 2022 Jul 20]. Available from: https://ebookcentral.proquest.com/lib/swansea-ebooks/reader.action?docID=625297#

125. SCIENTIFIC T. No Title [Internet]. Available from: http://www.tawadascientific.com/main.php?page=how-xrf-works&lang=en

126. Mallakpour S, Azimi F. Spectroscopic characterization techniques for layered double hydroxide polymer nanocomposites [Internet]. Layered Double Hydroxide Polymer Nanocomposites. Elsevier Ltd; 2020. 231–280 p. Available from: http://dx.doi.org/10.1016/B978-0-08-101903-0.00006-4

127. Mohamed Shameer P, Mohamed Nishath P. Exploration and enhancement on fuel stability of biodiesel: A step forward in the track of global commercialization [Internet]. Advanced Biofuels: Applications, Technologies and Environmental Sustainability. Elsevier Ltd; 2019. 181–213 p. Available from: http://dx.doi.org/10.1016/B978-0-08-102791-2.00008-8

128. Iso BS. Plastics — Film and sheeting — Determination of. 2002;3(1).

129. Abdo J, Zaier R. A novel pin-on-disk machine for stick-slip measurements. Mater Manuf Process. 2012;27(7):751–5.

130. Conshohocken W. Standard Test Method for Wear Testing with a Pin-on-Disk Apparatus 1. 2020;05(2016):5–10.

131. Böhm S, McMurray HN, Powell SM, Worsley DA. Photoelectrochemical investigation of corrosion using scanning electrochemical techniques. Electrochim Acta. 2000 Mar 31;45(14):2165–74.

132. Worsley DA, Mcmurray HN, Belghazi A. Determination of localised corrosion mechanisms using a scanning vibrating reference electrode technique. Chem Commun. 1997;

133. Sullivan JH, Mcmurray HN, Penney DJ, Worsley DA. Detection of Currents from a Model Pit Using the Scanning Vibrating Electrode Technique DETECTION OF CURRENT FROM A MODEL PIT USING THE SCANNING VIBRATING ELECTRODE TECHNIQUE (SVET).

134. Wint N, Wijesinghe SL, Yan W, Ong WK, Wu LY, Williams G, et al. The Sacrificial Protection of Steel by Zinc-Containing Sol-Gel Coatings. J Electrochem Soc. 2019;166(13):C434–44.

135. Isaacs HS. The Effect of Height on the Current Distribution Measured with a Vibrating Electrode Probe. J Electrochem Soc [Internet]. 1991 Mar 1 [cited 2022 Dec 6];138(3):722–8. Available from: https://iopscience.iop.org/article/10.1149/1.2085665

136. Isaacs HS, Kissel G. Surface Preparation and Pit Propagation in Stainless Steels. J Electrochem Soc [Internet]. 1972 Dec 1 [cited 2023 Jan 9];119(12):1628. Available from: https://iopscience.iop.org/article/10.1149/1.2404061

137. Loveday D, Peterson P, Rodgers B. Evaluation of organic coatings with electrochemical impedance spectroscopy: Part 1: Fundamentals of electrochemical impedance spectroscopy. CoatingsTech. 2004;1(8):46–52.

138. Chiodelli G, Lupotto P. Experimental Approach to the Impedance Spectroscopy Technique. J Electrochem Soc. 1991;138(9):2703–11.

139. Bonora PL, Deflorian F, Fedrizzi L. Electrochemical impedance spectroscopy as a tool for investigating underpaint corrosion. Electrochim Acta. 1996;41(7–8):1073–82.

140. Muster TH, Cole IS. The protective nature of passivation films on zinc: surface charge. Corros Sci [Internet]. 2004 Sep 1 [cited 2019 Mar 28];46(9):2319–35. Available from: https://www.sciencedirect.com/science/article/pii/S0010938X04000022

141. Rizza MA, Wijayanti W, Hamidi N, Wardana ING. Role of Intermolecular Forces on the Contact Angle of Vegetable Oil Droplets during the Cooling Process. Sci World J. 2018;2018.

142. Jiang HM, Chen XP, Wu H, Li CH. Forming characteristics and mechanical parameter sensitivity study on pre-phosphated electro-galvanized sheet steel. J Mater Process Technol. 2004;151(1-3 SPEC. ISS.):248–54.

143. Kronberger M, Pejaković V, Gabler C, Kalin M. How anion and cation species influence the tribology of a green lubricant based on ionic liquids. Proc Inst Mech Eng Part J J Eng Tribol. 2012;226(11):933–51.

144. Pejaković V, Kronberger M, Mahrova M, Vilas M, Tojo E, Kalin M. Pyrrolidinium sulfate and ammonium sulfate ionic liquids as lubricant additives for steel/steel contact lubrication. Proc Inst Mech Eng Part J J Eng Tribol. 2012;226(11):923–32.

145. Lobnig RE, Jankoski CA, R.E. Lobnig, D.J. Siconolfi, L. Psota-Kelty, G.

Grundmeier, R.P. Frankenthal, M. Stratmann JDS. Atmospheric Corrosion of Zinc in the Presence of Ammonium Sulfate Particles. J Electrochem Soc. 1996;143(3):1539–46.

146. Raab AE, Berger E, Freudenthaler J, Leomann F, Walch C. ZnAlMg Hot-Dip Galvanised Steel Sheets – Tribology and Tool Wear. 2012;157:126–31.

147. Çetinkaya BW, Junge F, Müller G, Haakmann F, Schierbaum K, Giza M. Impact of alkaline and acid treatment on the surface chemistry of a hot-dip galvanized Zn–Al–Mg coating. J Mater Res Technol. 2020;9(6):16445–58.

148. Van Landschoot N, Dane C, Bleeker R, Vlot M. Zinc-Magnesium Coated Hot Dip Galvanised Steel. ATZ Worldw. 2013;115(4):4–8.

149. Saarimaa V, Lange C, Paunikallio T, Kaleva A, Nikkanen J-P, Levä E, et al. Evaluation of surface activity of hot-dip galvanized steel after alkaline cleaning. 1998 [cited 2022 Nov 9]; Available from: https://doi.org/10.1007/s11998-019-00272-9

150. Lee BH, Keum YT, Wagoner RH. Modeling of the friction caused by lubrication and surface roughness in sheet metal forming. J Mater Process Technol. 2002;130–131:60–3.

151. Bachchhav B, Bagchi H. Effect of surface roughness on friction and lubrication regimes. Mater Today Proc [Internet]. 2020;38:169–73. Available from: https://doi.org/10.1016/j.matpr.2020.06.252

152. Permeh S, Lau K. Corrosion of galvanized steel in alkaline solution associated with sulfate and chloride ions. Constr Build Mater [Internet]. 2023;392(May):131889. Available from: https://doi.org/10.1016/j.conbuildmat.2023.131889

153. Gomes HI, Mayes WM, Rogerson M, Stewart DI, Burked IT. Alkaline residues and the environment: A review of impacts, management practices and opportunities. J Clean Prod. 2016;112:3571–82.

154. LeBozec N, Thierry D, Persson D, Riener CK, Luckeneder G. Influence of microstructure of zinc-aluminium-magnesium alloy coated steel on the corrosion behavior in outdoor marine atmosphere. Surf Coatings Technol [Internet]. 2019;374(March):897–909. Available from: https://doi.org/10.1016/j.surfcoat.2019.06.052

155. Penney DJ, Sullivan JH, Worsley DA. Investigation into the effects of metallic coating thickness on the corrosion properties of Zn-Al alloy galvanising coatings. Corros Sci. 2007;49(3):1321–39.

156. Sepper S, Peetsalu P, Saarna M. Methods for evaluating the appearance of hot dip galvanized coatings. Agron Res. 2011;9(SPPL. ISS. 1):229–36.

157. Siu JHW, Li LKY. An investigation of the effect of surface roughness and coating thickness on the friction and wear behaviour of a commercial MoS2-metal coating on AISI 400C steel. Wear. 2000;237(2):283–7.

158. Bonilla A, Argiz C, Moragues A, Gálvez JC. Effect of Sulfate Ions on Galvanized Post-Tensioned Steel Corrosion in Alkaline Solutions and the Interaction with Other Ions. Materials (Basel) [Internet]. 2022 [cited 2022 Nov 15];15(11). Available from: https://doi.org/10.3390/ma15113950

159. Calvo B, Cepeda EA. Solubilities of Stearic Acid in Organic Solvents and in Azeotropic Solvent Mixtures. [cited 2022 Jan 25]; Available from: https://pubs.acs.org/sharingguidelines

160. Heryanto R, Hasan M, Abdullah EC, Kumoro AC. Solubility of stearic acid in various organic solvents and its prediction using non-ideal solution models. ScienceAsia. 2007;33(4):469–72.

161. Cassie ABD, Baxter S. Wettability of porous surfaces. Trans Faraday Soc. 1944;40(5):546–51.

162. de Leon A, Advincula RC. Conducting Polymers with Superhydrophobic Effects as Anticorrosion Coating. In: Intelligent Coatings for Corrosion Control [Internet]. 2015 [cited 2022 May 11]. p. 409–30. Available from: https://app.knovel.com/web/view/khtml/show.v/rcid:kpICCC0001/cid:kt00U8P2E2/viewerType:khtml/root_slug:intelligent-coatings/url_slug:conducting-polymers-with?&b-toc-cid=kpICCC0001&b-toc-root-slug=intelligent-coatings&b-toc-title=Intelligent Coatings for C

163. Zouboy N DE, Pourbaix M. Atlas of Electrochemical Equilibria in Aqueous Solutions,. Pourbaix M, editor. Pergamon Press; 1966. 406 p.

164. Zhao W, Zhu R, Jiang J, Wang Z. Environmentally-friendly superhydrophobic surface based on Al2O3@KH560@SiO2 electrokinetic nanoparticle for long-term anti-corrosion in sea water. Appl Surf Sci. 2019 Aug 1;484:307–16.

165. Liu W, Sun C, Zhao P, Wang S. Solubility of stearic acid in ethanol 1-propanol 2-propanol l-butanol acetone methylene chloride ethyl acetate and 95% ethanol from (293 to 315) K. Adv Mater Res. 2012;550–553:71–4.

166. de Paiva EJM, Corazza ML, Sierakowski MR, Wärnå J, Murzin DY, Wypych F, et al. Influence of two different alcohols in the esterification of fatty acids over layered zinc stearate/palmitate. Bioresour Technol. 2015;193:337–44.

167. Williams J, Griffiths C, Dunlop T, Jewell E. Improving the Processability of a One-Step Hydrophobic Coating for Hot-Dipped Galvanised Steel for Industrial Applications. Coatings. 2022;12(7).

168. 6892-1:2019 BSENISO. Metallic materials. Tensile testing. Method of test at room temperature [Internet]. BSI Standards Publication. 2019 [cited 2022 Jun 27]. Available from: www.iso.org

169. Wint N, Khan K, Sullivan JH, McMurray HN. Concentration Effects on the Spatial Interaction of Corrosion Pits Occurring on Zinc in Dilute Aqueous Sodium Chloride. J Electrochem Soc. 2019;166(11):C3028–38.

170. Zhang XG. Galvanic Corrosion. Uhlig’s Corros Handb Third Ed. 2011;123–43.

171. Williams G, Neil McMurray H. Localized Corrosion of Magnesium in Chloride-Containing Electrolyte Studied by a Scanning Vibrating Electrode Technique. J Electrochem Soc [Internet]. 2008 May 16 [cited 2022 Dec 6];155(7):C340. Available from: https://iopscience.iop.org/article/10.1149/1.2918900

172. Loveday D, Peterspm P, Rodgers B. Evalution of organic coatings with electrochemical impedance spectroscopy part 2: Application of EIS to coatings [Internet]. Vol. 1, CoatingsTech. 2004 [cited 2022 Aug 26]. p. 88–93. Available

from: www.coatingstech.org

173. Moshinsky M. Dielectric Constants of Common Materials. Nucl Phys. 1959;13(1):104–16.

174. Resistivities of Solutions. :1400.

175. Cao L, Wan Y, Li Y, Yang S. Corrosion-resistant and friction-reducing performance of super-hydrophobic coating on hot-dip galvanised steel in a 3.5% NaCl solution. Lubr Sci. 2021;33(6):325–34.

176. Wahab R, Ansari SG, Kim YS, Dar MA, Shin HS. Synthesis and characterization of hydrozincite and its conversion into zinc oxide nanoparticles. J Alloys Compd. 2008 Aug 11;461(1–2):66–71.

177. Sun H, Liu S, Sun L. A comparative study on the corrosion of galvanized steel under simulated rust layer solution with and without 3.5wt% NaCl. Int J Electrochem Sci. 2013;8(3):3494–509.

178. Winiarski J, Tylus W, Winiarska K, Szczygieł I, Szczygieł B. XPS and FT-IR Characterization of Selected Synthetic Corrosion Products of Zinc Expected in Neutral Environment Containing Chloride Ions. J Spectrosc. 2018;2018.

179. Gupta AK, Kumar DR. Formability of galvanized interstitial-free steel sheets. J Mater Process Technol. 2006;172(2):225–37.

180. Sebastian D, Yao CW, Lian I. Mechanical durability of engineered superhydrophobic surfaces for anti-corrosion [Internet]. Vol. 8, Coatings. 2018 [cited 2022 Nov 30]. Available from: www.mdpi.com/journal/coatings

181. Fihri A, Bovero E, Al-Shahrani A, Al-Ghamdi A, Alabedi G. Recent progress in superhydrophobic coatings used for steel protection: A review. Colloids Surfaces A Physicochem Eng Asp [Internet]. 2017;520:378–90. Available from: http://dx.doi.org/10.1016/j.colsurfa.2016.12.057

182. Feng L, Li S, Li Y. Super-Hydrophobic Surfaces : From Natural to Artificial Super-Hydrophobic Surfaces : From Natural to Artificial **. Adv Mater. 2016;(October):1857–60.